

## Development of Analog Phased Array Antenna for Real-time Location System

グアン, チャイ ユー

<https://doi.org/10.15017/1931941>

---

出版情報 : 九州大学, 2017, 博士 (工学), 課程博士  
バージョン :  
権利関係 :



Graduate School of Information Science and Electrical Engineering

Kyushu University, Fukuoka, Japan.

# **Development of Analog Phased Array Antenna for Real-time Location System**

by

**Guan Chai Eu**

A thesis submitted to the Graduate School of Information Science and Electrical  
Engineering in partial fulfilment of the requirements for the degree of

Doctor of Engineering

*Kyushu University, Fukuoka, Japan.*

2018

DEPARTMENT OF ELECTRONICS  
GRADUATE SCHOOL OF INFORMATION SCIENCE AND  
ELECTRICAL ENGINEERING  
KYUSHU UNIVERSITY  
Fukuoka, Japan

Thesis Title:

**Development of Analog Phased Array Antenna for Real-time Location  
System**

Prepared by: **Guan Chai Eu**

Supervisor : **Professor Haruichi Kanaya, Dr. Eng.**

Co-supervisor 1: **Professor Kuniaki Yoshitomi, Dr. Eng.**

Co-supervisor 2: **Professor Kazutoshi Kato, Dr. Eng.**

Date: March 2018



Graduate School of Information Science and Electrical Engineering  
Kyushu University, Fukuoka, Japan.

**To Whom It May Concern,**

We hereby certify that this copy is a typical copy of the original Dr. Eng. (Doctor of Engineering) thesis of

**Mr. Guan Chai Eu**

Dissertation Title:

**DEVELOPMENT OF ANALOG PHASED ARRAY ANTENNA FOR  
REAL-TIME LOCATION SYSTEM**

Supervisor,

---

Prof. Haruichi Kanaya, Dr. Eng.

Department of Electronics,

Graduate School of Information Science

and Electrical Engineering,

KYUSHU UNIVERSITY

March, 2018.

## **Acknowledgements**

First and foremost, I would like to express my deepest gratitude and sincere appreciation to my research supervisor, Professor Haruichi Kanaya for his guidance and support over the course of this research. I have benefited greatly from his perceptive and remarkable knowledge of my field of research. Inspirations gained from technical discussions with him have proven to be invaluable in defining my research direction. In addition, good research environment and hospitality offered by Professor Haruichi Kanaya becomes one of the most memorable experiences in my life.

Furthermore, I would like to thank to Professor Kuniaki Yoshitomi and Professor Kazutoshi Kato for serving on my dissertation committees. Their valuable suggestions are very useful in the improving quality of the dissertation. Their generosity in providing their expertise and advices has inspired me to engage in lifelong learning and being relevant to the organization and community that I will be attached to.

Interacting with my colleagues in RFIC and Microwave Communication Device laboratory has been rewarding, both personally and professionally. I am particularly indebted to every member in the laboratory whom unconditionally lent their kind support to me when I was a research student and after I become a PhD candidate. Many arduous evaluations and experiments became more rewarding with their assistance.

Besides, I would like to express my gratitude to our industry collaborators—Mr.Akira Ishikawa, Mr.Shugo Fukagawa and Mr.Ryuji Kitaya from Kyushu Ten. They assisted me in many aspects and their supports made this research became less strenuous. Also, I would like to extend my gratitude to the university co-investigators: Mr. Tomoki Oda, Mr. Fumiya Iwai, Mr. Kota Tsugami and Mr. Takuhiro Ide, for their significant contributions in developing receiver module for the wireless locating system.

This dissertation would never have been completed without the sponsor and support from Japan Ministry of Education, Culture, Sports, Science and Technology (MEXT). I am extremely indebted to the Japan government for the financial aid given and assigning me to learn from a supportive, dedicated, and profound research supervisor. Thank you.

## **Abstract**

Global Positioning System (GPS) is widely used for locating and tracking objects due to their maturity and large scale implementation. Increase in the number of satellites and number of satellite systems spurs rapid development of detailed digital maps. Many vehicles used in government and commercial sectors, such as taxis, buses, ambulances, and fire trucks are equipped with navigation systems that not only show the current location but constantly trace the movement of vehicle from a monitoring center. Business ventures such as Uber and Grab benefited from the advancement of GPS that leads to new mobile internet applications to complete the conventional public transport services. Uber and Grab-based applications enable prospective passengers to request door-to-door transport service via mobile phone booking.

From the point of view the security and traceability, demands for real-time location tracking of object or human in indoor environment increases. GPS (Global Positioning System), a satellite-based real-time location tracking system, is widely used in providing critical positioning capabilities to commercial users. Due to inability of transmitted signals to penetrate through the wall of building, GPS is unfitted for indoor environment, such as inside building and factory. Low accuracy in the range of 1 meter makes satellite-based location tracking system less suitable for indoor environments. On the other hand, the capability of time difference of arrival (TDOA) based radar, which operates at license-free high band UWB (Ultra-wide band, 7.25 GHz to 10 GHz), capable of estimating object location with the accuracy of 10 cm has been reported. TDOA method estimates signal propagation distance by calculating difference between the time that signals were sent, and time that signals arrive at receiver. It was reported that transmitted pulse shorter than 1 ns is required for precise indoor object-tracing, so that time difference between incident and arrival signals can be exactly measured.

While UWB systems have a very good accuracy, their maximum operation range is limited by few tens of meters. Realization of a system with high antenna gain for long distance communication systems, such as object tracking in warehouse and factory, becomes main challenge because maximum radiated power spectral density of the existing system is limited by local laws and regulations.

The dissertation presents design methodology to increase antenna gain and scan angle in a wideband phased-array system in indoor environment. First part of this dissertation presents a 1x4 printed array antenna for multiple layers PCB. The goal of this work is to design an antenna with realized gain and input impedance less responsive to substrate thickness. Patch antenna fed by two-layer proximity coupled feed line is proposed to alleviate gain degradation caused by thin substrate. Fabricated antenna exhibits good radiation characteristics and a flat gain response from 7.7 to 8.3 GHz. Besides, optimum separation between periodically spaced vias is analyzed and proposed to reduce propagation leakage in the dielectric region.

Second part of this dissertation presents the analysis and design of a full 360 degrees, harmonic-suppressed hybrid coupler phase shifter. Numerical and parametric analyses are used to find the equivalent circuit for circuit proposed. Simulation and measurement results demonstrated that fabricated phase shifter suppresses second harmonic and achieves phase shift range of 360 degrees. Next, harmonic-suppressed phase shifter with new reflective network is presented for phased-array system. Continuous relative phase shift of 250 degrees and insertion loss variation less than 1 dB are achieved with 0-to-10V reverse bias voltages. It is observed that insertion loss variation is smaller than commercial phase shifters and phase shifters found in the literature.

Finally, last part of this dissertation presents the integration of antenna array, power divider, phase shifter and parasitic antenna elements on multiple layers PCB to realize phased array antenna. By placing parasitic antennas in between active antenna arrays, it is found that mutual coupling effect between parasitic antennas and neighbor active driven antenna increases scan angle range of phased array antenna. The measured far-field radiation patterns of fabricated phased array antenna match to the simulation results. Proposed work extends maximum scan range from 55 degrees to 60 degrees. In this work, wide scan angle is realized by using phase shift range lower than phase shift range required in conventional corporate-fed phased array antennas.

# Contents

Acknowledgements.....	i
Abstract.....	ii
Contents.....	iv
List of Figures.....	vi
List of Tables.....	ix
List of Abbreviations.....	x
CHAPTER 1: INTRODUCTION.....	1
1.1 Motivations.....	3
1.2 Research Objectives.....	4
1.3 Thesis Outline.....	5
CHAPTER 2: PHASED ARRAY SYSTEM.....	7
2.1 Beam Steering Concept in Analog Phase Shifter.....	9
2.2 Phase Shifting Techniques.....	12
2.3 Array Feeds.....	
2.3.1 Series Array Feed.....	14
2.3.2 Corporate Array Feed.....	15
2.4 Scan Angle Range of Analog Phased Array Antenna.....	16
2.5 Antenna Gain and Radiation Efficiency.....	16
2.6 Chapter Summary.....	19
References.....	20
CHAPTER 3: LINEAR ARRAY ANTENNA.....	21
3.1 Antenna Design.....	
3.1.1 Antenna Geometry.....	22
3.1.2 Antenna Resonant Frequency.....	24
3.1.3 Fields Radiated in Patch in $TM^x$ Mode.....	26
3.1.4 Antenna Input Impedance.....	28
3.1.5 Antenna Array Principle.....	29
3.2 Wilkinson Power Divider.....	31
3.3 Simulation and Measurement Results of Proposed Antenna Array.....	35



3.4 Electromagnetic Leakage Suppression in Propagation Medium	
3.4.1 Minimum Distance of Periodically Spaced Vias.....	40
3.4.2 Design Verification and Implementation.....	43
3.4.3 Simulation and Measurement Results.....	45
3.5 Chapter Summary.....	48
References.....	49

## CHAPTER 4: PHASE SHIFTER

4.1 Phase Shifter with Harmonic Suppression	
4.1.1 Numerical Analysis.....	54
4.1.2 Parametric Analysis.....	61
4.1.3 Relationship of Series Inductance and Phase Shift Range.....	62
4.1.4 Design Implementation and Fabrication.....	66
4.1.5 Simulation and Measurement Results.....	67
4.2 Phase Shifter with Discrete Reflective Loads	
4.2.1 Circuit Analysis.....	70
4.2.2 Design Implementation and Fabrication.....	74
4.2.3 Simulation and Measurement Results.....	75
4.3 Chapter Summary.....	80
References.....	81

## CHAPTER 5: PHASED ARRAY ANTENNA

CHAPTER 5: PHASED ARRAY ANTENNA	83
5.1 Phased Array Antenna Architecture.....	85
5.2 Parasitic Element For Scan Angle Enhancement.....	87
5.3 Design Implementation and Fabrication.....	90
5.4 Simulation and Measurement results	
5.4.1 S-parameter.....	91
5.4.2 Maximize Scan Angle Using Parasitic Antenna.....	92
5.4.3 Far-field Radiation and Realized Gain.....	93
5.5 Chapter Summary.....	101
References.....	103

## CHAPTER 6: CONCLUSIONS AND FUTURE WORKS

CHAPTER 6: CONCLUSIONS AND FUTURE WORKS	105
6.1 Conclusions.....	105
6.2 Future Works.....	108
References.....	109

## List of Figures

Fig. 2.1	Digital beamforming architecture.....	8
Fig. 2.2	Analog beamforming architecture.....	9
Fig. 2.3	Linear phased array antenna.....	10
Fig. 2.4	Calculated radiation pattern of non-steering phased array antenna with (a) $d = 0.5\lambda_0$ (b) $d = \lambda_0$ .....	13
Fig. 2.5	Series and corporate array feeds.....	15
Fig. 2.6	Calculated radiation pattern of 1x4 phased array antenna with $d=0.5\lambda_g$ and $\theta=180^\circ$ , (a) Normalized radiation pattern. (b) Phase difference $\theta$ between antenna elements.....	17
Fig. 2.7	Phase between current $I$ and voltage $v$ , (a) Ideal case (b) lossy dielectric medium.....	18
Fig. 3.1	Geometry of the proposed antenna.....	22
Fig. 3.2	Electromagnetic field distribution in patch.....	23
Fig. 3.3	Structure of rectangular patch antenna.....	24
Fig. 3.4	Excitation modes of rectangular patch antenna.....	26
Fig. 3.5	Perspective view of the patch and its radiation pattern. (a) Perspective view (b) $xy$ -plane pattern (c) $xz$ -plane pattern.....	27
Fig. 3.6	Antenna input impedance in response to $w_{p2}$ -to- $w_{f1}$ ratio.....	28
Fig. 3.7	Linear array consists of isotropic point sources equally-spaced with distance $d$ .....	30
Fig. 3.8	Array factor of two elements antenna versus spatial phase delay, $\psi$ .....	31
Fig. 3.9	Three ports power divider. (a) Power divider with dividing ratio, $r$ (b) Wilkinson power divider.....	32
Fig. 3.10	Transmission line circuit model of Wilkinson power divider.....	32
Fig. 3.11	Power source with source impedance matched to the transmission line.....	34
Fig. 3.12	Gain drop in conventional patch antenna and proposed antenna at $xz$ - plane, in response to substrate thickness reduction.....	36
Fig. 3.13	Photograph of the fabricated array antenna.....	36
Fig. 3.14	Antenna input impedance measurement with Keysight 8722C Network analyzer.....	37
Fig. 3.15	Radiation pattern measurement setup in anechoic chamber.....	37
Fig. 3.16	$S_{11}$ and maximum realized gains of the proposed array antenna. Simulations (solid) and measurements (dashed).....	38
Fig. 3.17	Simulated (solid) and measured (dashed) radiation patterns of the proposed array antenna at 8 GHz: (a) $xz$ plane, (b) $yz$ plane.....	39
Fig. 3.18	Geometry of the CBCPW with periodically spaced vias.....	41
Fig. 3.19	Region of interest for the CBCPW with periodically spaced vias....	42
Fig. 3.20	Layouts of antenna array fed by different topology. (a) CPW with air bridges. (b) CBCPW with a periodic spaced-via .....	44

Fig. 3.21	Fabricated 4x1 antenna array with the CBCPW feed network (size=234 mm x 71 mm). (a) Top view. (b) Bottom view.....	45
Fig. 3.22	Measured reflection coefficient and achieved gain of the CPW-fed and the CBCPW-fed antenna arrays.....	46
Fig. 3.23	Radiation pattern of 4x1 CBCPW-fed antenna array. (a) xz-plane. (b) yz-plane.....	47
Fig. 4.1	Digital phase shifter, (a) Circuit block diagram (b) I-Q relationship...	52
Fig. 4.2	Null in phased array antenna due to destructive interference between phase shifter and antenna elements.....	54
Fig. 4.3	Schematic diagram of $\pi$ -section low pass filter (LPF).....	55
Fig. 4.4	Schematic of the conventional RTPS.....	57
Fig. 4.5	Schematic of proposed phase shifter with harmonic suppression.....	57
Fig. 4.6	Calculated relative phase shift versus port impedance ratio $r_z$ ( $Z_{qw}=20\ \Omega$ , $L_s=0.45\text{nH}$ , $C_{min}=0.45\text{pF}$ , $C_{max}=3.1\text{pF}$ and $R_s=2.5\Omega$ .....	59
Fig. 4.7	Transmission line of the hybrid coupler. (a) Quarter wavelength transmission line. (b) Distributed elements $\pi$ -section filter.....	59
Fig. 4.8	Parametric variation of the electrical length $\theta_l$ of the transmission line to obtain $r_z=2$ (a) $Z_{i2}$ versus $\theta_l$ variation. (b) $Z_{o2}$ versus $\theta_l$ variation....	63
Fig. 4.9	Theoretical calculation of the relative phase shift versus varactor bias voltage ( $L_s$ varies).....	65
Fig. 4.10	Theoretical calculation of the relative phase shift versus varactor bias voltage ( $Z_{qw}$ varies).....	65
Fig. 4.11	Layout of the full-360°, harmonic-suppressed hybrid coupler phase shifter.....	66
Fig. 4.12	A full 360°, harmonic-suppressed hybrid coupler phase shifter (left) and $\pi$ -section LPF (right).....	67
Fig. 4.13	Second harmonic suppression of the $\pi$ -section LPF at 17.2 GHz. (a) Simulation (dashed) using HFSS (b) Measurement (solid).....	68
Fig. 4.14	Second harmonic suppression of the proposed phase shifter, in comparison with conventional phase shifter. S represents simulation results from HFSS, and M represents measurements.....	68
Fig. 4.15	Relative phase shift versus varactor bias voltage evaluated at fundamental frequency of 8.6GHz. Simulation (solid) result from HFSS, and measurement (dashed).....	69
Fig. 4.16	$ S_{11} $ (black), $ S_{22} $ (blue), and $ S_{21} $ (grey) of the phase shifter at various varactor bias voltage Vb. (a) Simulations (b) Measurements...	69
Fig. 4.17	Schematic diagram of phase shifter with discrete reflective loads.....	70
Fig. 4.18	Calculated relative phase shift versus tuning range of varactor at 8.6 GHz ( $L_s=0.2\text{nH}$ , $Z_{03}=25\Omega$ , and $R_s=2\ \Omega$ ).....	72
Fig. 4.19	Calculated insertion loss of phase shifter versus tuning range of varactor ( $L_e=0.4\ \text{nH}$ , $L_s=0.2\text{nH}$ , $C_{min}=0.2\text{pF}$ , $C_{max}=1\text{pF}$ , $Z_{03}=25\Omega$ , and $R_s=2\ \Omega$ )	73
Fig. 4.20	Calculated phase shift across frequencies of interest ( $L_e=0.4\ \text{nH}$ , $L_s=0.2\text{nH}$ , $Z_{03}=25\Omega$ , and $R_s=2\ \Omega$ ).....	73

Fig. 4.21	Layout of phase shifter with discrete loads.....	74
Fig. 4.22	Input return loss $S_{11}$ of phase shifter, simulation (solid) and measurement (dashed).....	75
Fig. 4.23	Output return loss $S_{22}$ of phase shifter, simulation (solid) and measurement (dashed).....	76
Fig. 4.24	Insertion loss $S_{21}$ of phase shifter, simulation (solid) and measurement (dashed).....	76
Fig. 4.25	Insertion phase $\phi S_{21}$ of phase shifter output, simulation (solid) and measurement (dashed).....	77
Fig. 4.26	Electric field distribution of phase shifter with reflection loads separated by quarter wave-length transmission line.....	78
Fig. 4.27	Electric field of proposed phase shifter with discrete reflection loads..	78
Fig. 5.1	Corporate-fed phased array antenna with the proposed phase shifter...	86
Fig. 5.2	Phase shifter with different reflection loads topology. (a) Conventional phase shifter. (b) Proposed phase shifter with discrete reflective loads.....	86
Fig. 5.3	Mutual coupling between active dipole antenna and parasitic antenna	89
Fig. 5.4	Electric field distribution at scanning angle of $+30^\circ$ .....	89
Fig. 5.5	Prototype of phased array antenna (74.5 mm x 46.8 mm). (a) Top view. (b) Bottom view.....	90
Fig. 5.6	Phased antenna measurement in anechoic chamber.....	91
Fig. 5.7	Return loss of the phased array antenna at various scan angle.....	92
Fig. 5.8	Induced current at the floating parasitic antenna.....	92
Fig. 5.9	Radiation pattern at scan angle, $\theta=0^\circ$ and center frequency, $f_c=8.6$ GHz (xz-plane). (a) Simulation. (b) Measurement. (c) Simulated 3D radiation pattern.....	93
Fig. 5.10	Radiation pattern at scan angle, $\theta=-10^\circ$ and center frequency, $f_c=8.6$ GHz (xz-plane). (a) Simulation, (b) Measurement. (c) Simulated 3D radiation pattern.....	94
Fig. 5.11	Radiation pattern at scan angle, $\theta=+10^\circ$ and center frequency, $f_c=8.6$ GHz (xz-plane). (a) Simulation. (b) Measurement. (c) Simulated 3D pattern.....	94
Fig. 5.12	Radiation pattern at scan angle, $\theta=-30^\circ$ and center frequency, $f_c=8.6$ GHz (xz-plane). (a) Simulation. (b) Simulated 3D pattern.....	95
Fig. 5.13	Radiation pattern at scan angle, $\theta=+30^\circ$ and center frequency, $f_c=8.6$ GHz (xz-plane). (a) Simulation. (b) Simulated 3D pattern.....	95
Fig. 5.14	Simulated realized gain of phased array antenna at xy-plane (max. scan angle $\theta=\pm 30^\circ$ ).....	96
Fig. 5.15	Broadside radiation beam at multiple frequencies (no beam steering)..	97
Fig. 5.16	Scan angle of $-15^\circ$ at multiple frequencies.....	97
Fig. 5.17	Scan angle of $+15^\circ$ at multiple frequencies.....	98
Fig. 5.18	Scan angle of $-30^\circ$ at multiple frequencies.....	98
Fig. 5.19	Scan angle of $+30^\circ$ at multiple frequencies.....	99
Fig. 5.20	Schematic of DC-to-DC step up converter (LMR62421) and its subsidiary components.....	102

## List of Tables

Table 3.1	Design parameters of the proposed antenna.....	28
Table 3.2	Resultant voltages from superposition analysis.....	34
Table 3.3	Wilkinson power divider S parameters at input and output ports....	35
Table 4.1	Design parameters of the RTPS ( $r_z=2$ ).....	65
Table 4.2	Parameters of $\pi$ -section LPF obtained from numeric and parametric analysis.....	66
Table 4.3	Parameters of $\pi$ -section LPF (unit in mm).....	66
Table 4.4	Dimension of phase shifter with discrete loads. (unit in mm).....	74
Table 4.5	Comparison of proposed works against other phase shifters found in the literature.....	79
Table 5.1	Progressive phase shift required for beam steering from $-25^\circ$ to $+25^\circ$ .....	85
Table 5.2	Comparison of phased array antenna with and without parasitic element.....	87
Table 5.3	Realized gain at difference scan angle at the center frequency, $f_c=8.6$ GHz.....	99
Table 5.4	Comparison of the proposed phased array antenna against other steerable antennas found in the literature.....	100

## List of Abbreviations

ADC	-	Analog to digital converter
AF	-	Antenna factor
CBCPW	-	conductor backed co-planar waveguide
CMOS	-	Complementary metal-oxide semiconductor
CPW	-	co-planar waveguide
DBF	-	Digital beamforming
DC	-	Direct current
DOA	-	Direction of arrival
DSP	-	Digital signal processor
DUT	-	Device under test
ESPAR	-	Electronically steerable passive array radiator
FPGA	-	Field programmable gate array
IF	-	Intermediate frequency
ISM	-	Industrial, science and medical
LMS	-	Least mean square
LNA	-	Low noise amplifier
LO	-	Local oscillator
LTCC	-	Low temperature co-fired ceramic
MIMO	-	Multiple Input Multiple Output
MMIC	-	Monolithic microwave integrated circuit
MSL	-	Microstrip line
PCB	-	Patterned circuit board
RF	-	Radio frequency
RLS	-	Reclusive least square
RTPS	-	Reflective-type phase shifter
SINR	-	Signal to noise interference
UWB	-	Ultra-wide band

# Chapter 1

## **Introduction**

As wireless technology progresses, antennas are evolved in order to keep its pace to the latest demands of the market. Reconfigurable antenna in wireless communication system offers spatial directivity and antenna gain to increase spectral efficiency. Directivity of antenna array in wireless communication with beam steering capability can be adapted to a particular transmit or receive angle. Generally, antenna elements with the same radiation patterns and polarizations are used to populate phased array system, which leads to performance enhancement in terms of peak gain and beam width characteristics.

In satellite communication, antenna on the surface of earth is fixed and pointed to satellites located in geosynchronous orbit. Constant communication is maintained because orbital periods of satellites are same as the Earth's rotation period. Reflector antenna, which has high gain, is preferred in point-to-point communication. Antenna array with beam steering capability is preferred when simultaneous communication between stationary earth station and several geostationary (GEO) satellites is required.

In cellular communications and Wi-Fi system, antenna array with beam steering capability is deployed in multiple input multiple output (MIMO) system. MIMO systems benefit from increase in data rate and network capacity.

Multiple, spatially separate data can be transmitted over the same frequency band via beam steering technique. Besides, beam steerable antenna can dynamically respond to the propagation environment to minimize multipath fading.

In RFID systems, beam steering technology is the backbone of wireless locating and tracing system. Its implementation allows real-time tracking of goods and products, for more efficient storage and sequence planning. Radiation beam can be adaptively steered from one spot to another spot in the surveillance region without any additional readers. Several commercial UWB radars, which use low energy spectral density based on chirp-spread spectrum signals, are able to provide minimum accuracy of few centimeters such as, PulsON 440 module, Decawave Scensor DW1000 and Ubisense Dimension4.

In automotive industry, Lidar (Light radar), which is based on beam steering technology, are widely researched for the next-generation car sensor. It detects objects with optical pulses and produces a set of data points to estimate the distance of nearby objects. On 2016 consumer electronics show (CES) exhibition, Quanergy Systems, which is based in Sunnyvale (California), demonstrated a prototype solid-state Lidar sensor designed for driverless car. Representative from Quanergy quoted that its sensor will cost 250 USD in volume production. Currently, industry players are working hard towards their final goal of realizing solid-state Lidar sensor, which is capable of detecting 100 m object with a selling price of 10 USD per chip.

Beam steering technology can be realized on patterned circuit board (PCB), low temperature co-fired ceramic (LTCC) or silicon-based technologies such as complementary metal-oxide semiconductor (CMOS) and silicon germanium (SiGe). For millimeter-wave band wireless communication system, compound semiconductors, e.g. indium phosphide (InP) and gallium arsenide (GaAs), are preferred, irrespective of their high fabrication cost and complex fabrication process. Currently, the cost of CMOS or monolithic microwave integrated circuit (MMIC) chip fabrication and complexity of phased array antennas are the main impediments to their deployment in any large scale commercial application.



X-band spectrum, as well as high band ultra-wideband (UWB) spectrum, has short wavelength ( $<5$  cm). They are good candidates for wireless locating system that requires accuracy resolution of 10 cm for object tracking. Development of phased array system operates at X-band on patterned circuit board (PCB) will reduce production cost and extend the deployment of phased array antenna to a wide range of consumer applications. Usually, microwave devices operate X-band or high band UWB spectrums are fabricated on CMOS or compound semiconductors. Implementation of the microwave devices on standard PCB that has higher tangent loss than CMOS and compound semiconductors, poses several challenges in terms of substrate loss, module size, dispersion characteristics in the microstrip transmission line and etc.

This dissertation investigates on the high band UWB phased array antenna implemented on patterned circuit board (PCB) to achieve good cost versus performance. First, designs of phased array antennas found in the literature are taken as reference models. Modular approach is adopted to develop microwave devices, i.e. antenna, phase shifter, and power distribution network, separately. Next, all microwave devices are integrated into a single module on multiple layers PCB. Viable solutions are then proposed to realize phased array antenna that meet requirements of commercial applications such as realized gain, scan angle, power consumption, operation bandwidth, control voltages, and manufacturing cost.

### 1.1 Motivations

Wireless communication systems in the consumer market normally operate at 2.4 and 5 GHz frequency ranges. However, the growing demands for higher data rates spur the development of wireless communication system at higher frequencies because significantly wide bandwidth can be obtained as operating frequency is increased. Wavelength at higher frequencies, e.g. X-band and above, is shorter than the ones in 2.4 GHz and 5 GHz. As opposed to wavelength at 2.4 GHz or 5 GHz, X-band signal has a shorter wavelength, in which signal could not penetrate through walls and ceilings. Short wavelength has good isolation in indoor environment enables frequency reuse in order to extend the number of users.

In indoor environments such as the factory and airport checked luggage area, wide operation bandwidth and frequency reuse are required for real-time object tracking system. From the point of view the security and traceability, the growth of real-time location estimation of object or human in indoor environment is expected. In outdoor environment, a satellite-based real-time location tracking system, GPS (Global Positioning System) is widely used in providing critical positioning capabilities to users. Due to its inability of transmitted signals to penetrate through the wall of building, airborne GPS is unfitted for indoor environment, such as inside building and factory.

On the other hand, the capability of time difference of arrival (TDOA)-based radar to estimate object location with the accuracy of 10 cm has been reported. It operates in license-free high band UWB (ultra-wide band, 7.25 GHz to 10 GHz). TDOA method estimates signal propagation distance by calculating difference between the exact times that signals were sent, and time that signals arrive at receiver. Maximum radiated power spectral density of the present system is limited by local laws and regulations. By increasing antenna gain in a system, communication distance can be extended in system with restricted power spectral density.

This dissertation presents a design methodology to increase antenna gain and maximize scan angle in phased array systems with a limited bias voltage. PCB manufacturing process is preferred because of its low fabrication cost and ease of implementation. Best to author's knowledge, implementation of module-based phased array system at X-band using PCB manufacturing process has not been reported prior to this work. Considering the merit of cost versus performance of PCB-based phased array antenna, the development of beam steering system for real time location system is investigated thoroughly in this dissertation.

### 1.2 Research Objectives

The objectives of this thesis are to develop phased array antenna in a single module, which has the following unique features that can be summarize as:

- (1) Intermodulation Distortion Reduction: Designed phase shifter must be capable of suppressing high order harmonics on transmitter and receiver paths.

Suppression of high order harmonics at the RF front-end reduces intermodulation distortion at low noise amplifier (LNA) in the receiver path.

- (2) Beam Squint: Beam squint refers to the changes in scanning angle of phased array antenna when the operating frequency is changed. Beam squint is commonly found in series-fed phased array antenna because of large group delay from accumulated phase shift. Corporate-fed phased array antenna has minimum beam squint but strict requirement for large phase shift range in individual phase shifter limits scan angle of the adaptive antenna array.
- (3) Scan Angle with Low Bias Voltage: To achieve large scan angle range, large progressive phase shift range is required in phased array antenna. My research objective is to widen scan angle of phased array antenna with restricted phase shift range, by using 10 V bias voltage. Parasitic antenna elements are introduced to extend original scan angle, in order to overcome phase shift limitation imposed by phase shifters.

### 1.3 Thesis Outline

The dissertation is organized in 6 chapters to define and explain on the development of analog phased array antenna. Concept of beam steering in analog phased array antenna is provided in Chapter 2. Phased array system architecture and possible phase shifting techniques are then discussed. Issue related to grating lobes in the radiation pattern caused by separation distance between adjacent antenna elements is highlighted. Next, power distribution network of the antenna elements is explored to ensure uniform power distribution and evade some issues related to scan angle across frequencies of interest. The relationship of scan angle with progressive phase shift and separation distance between adjacent antennas is defined.

Chapter 3 discusses the implementation of linear antenna array on multiple layers PCB process. Antenna elements are fabricated on 1.6 mm while power distribution network is fabricated on 0.2 mm PCB. Antenna elements and its distribution network are combined into single module using multiple layers PCB to achieve compact and low profile structure.

Two layer proximity coupling is introduced in slotted patch antenna for impedance matching purpose. In addition, periodically spaced vias structure is proposed for radiation suppression in the transmission line. At the end of the section, simulation and measurement results are presented to validate design concept introduced.

Chapter 4 presents the analysis and design of a full 360 degrees, harmonic-suppressed hybrid coupler phase shifter. Numerical and parametric analyses are introduced as tools of analysis. Simulation and measurement results demonstrate that fabricated phase shifter suppresses higher harmonics and achieves relative phase shift range of 360°. Next, harmonic-suppressed phase shifter with reflective network constructed from discrete varactors and inductors is proposed. Continuous relative phase shift of 250° and insertion loss variation with less than 1 dB are achieved with 10 V reverse bias voltage. The loss variation obtained is less than commercial phase shifters and phase shifters found in the literature.

Chapter 5 presents the integration of antenna array, power divider, phase shifter and parasitic antenna elements fabricated on multiple layers PCB to form phased array antenna. By placing parasitic antennas in between active antenna arrays, it is found that mutual coupling between active antennas and parasitic antennas increases scan angle range of phased array antenna. The measured far-field radiation patterns of the fabricated phased array antenna match to simulation results. Proposed parasitic antennas extend the maximum scan angle range from 50° to 60°. Proposed design technique enables wide scan angle to be achieved by phase shifter with limited phase shift range. Required relative phase shift range for  $\pm 30^\circ$  scan angle is less than other commercially available phased array system and phased array antennas found in the literature.

In the last chapter, contributions from all works and techniques are summarized. Realization of phased array antenna with beam steering capability at device level and system level are concluded. Besides, other prospective technique to improve the gain of phased array system across wideband is reviewed.

## Chapter 2

### Phased Array Systems

The presence of phased array antenna enables antenna beam to be steered by electronic mean. Beam is steered by controlling phase and amplitude of incoming RF signals of phased array antenna. Beam steering techniques can be classified into analog and digital beamforming. Digital beamforming (DBF) architecture offers several sophisticated features, including multiple beams forming capability, direction of arrival (DOA) estimation, and good signal-to-interference noise ratio (SINR). Fig 2.1 shows the block diagram of a DBF antenna. DBF architecture consists of orthogonal transform unit and field programmable gate array (FPGA) to deliver amplitude and phase weights to antenna elements. Orthogonal transformation unit separates incoming intermediate frequency (IF) signals into in-phase  $I$ , and quadrature  $Q$  components. The modulated complex signals of antenna beams are processed by FPGA. Adaptive algorithm such as Least Mean Square (LMS), Recursive Least Square (RLS) and Conjugate Gradient Method (CGM) is utilized to compute the array weights [1]-[3]. The computed weights are downconverted to intermediate frequency (IF) signals and distributed to antenna elements for beam steering.

The analog approach, on the other hand, is less capable to execute the same functionalities that DBF does. Fig 2.2 depicts two architectures of phased array antenna using analog approach. As we can see, analog beamforming architectures require neither analog-to-digital converters (ADCs) nor FPGA for complex amplitude and phase distributions.

Analog approach offers low DC power consumption and affordable fabrication cost because of the absence of high-priced FPGA and ADCs. Architecture in Fig. 2.2(a) shows analog beamforming architecture, where complex weight is applied to the signal at radio frequency (RF) stage. The architecture is not suitable for system designated at frequency above Ku-band because off-the-shelf phase shifter operates at Ku-band is scarce; even if it were available, it should be expensive due to the low demand-to-supply ratio. RF complementary metal oxide semiconductor (RF-CMOS) and patterned circuit board (PCB) technology are the most common technologies used to fabricate phase shifter. For RF-CMOS phase shifter, transient frequency  $f_t$  of the gate transistor limits operation frequency of the device. PCB-based phase shifter can be deployed at high frequency; nevertheless, severe dielectric loss at high frequency due to tangent loss of dielectric material is inevitable. For system suffered from high attenuation at high frequency, variable gain amplifier was introduced to amplify weak RF signal [4]. Another technique to overcome severe attenuation at high frequency is demonstrated in Fig. 2.2(b), where phase shifting is implemented at intermediate frequency (IF) stage. In this architecture, RF signals are down-converted to IF signal for its phase to be shifted using phase shifters operate at IF-stage.

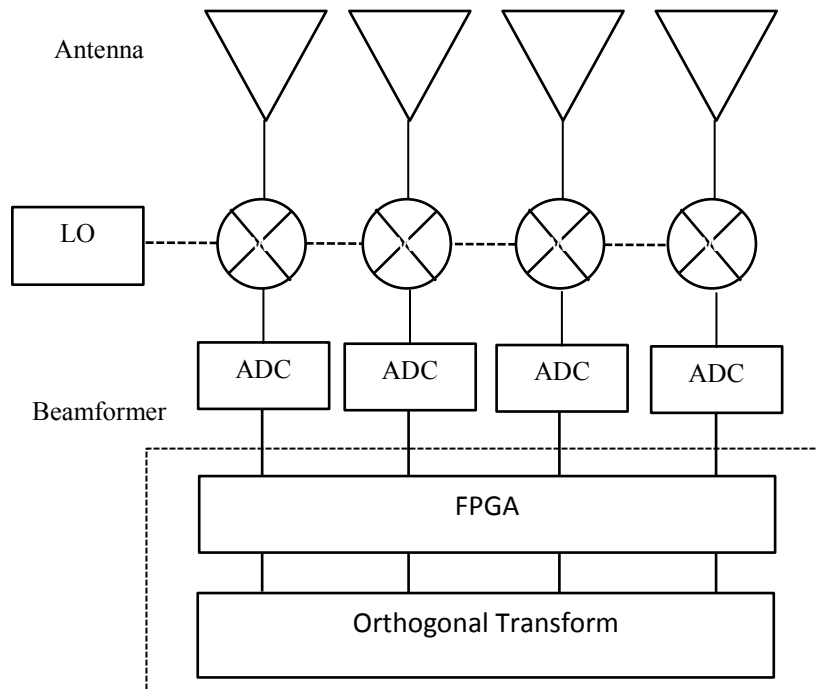


Fig. 2.1 Digital beamforming architecture.

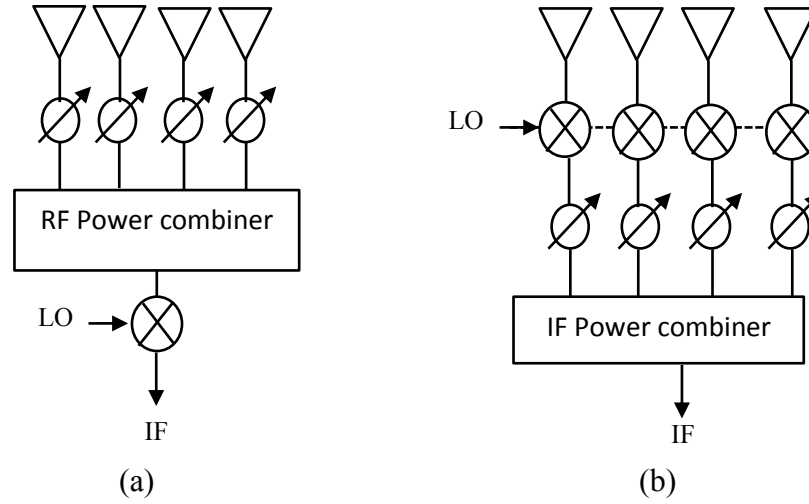


Fig. 2.2 Analog beamforming architecture. (a) RF Phase Shifting. (b) IF Phase Shifting.

### 2.1 Beam Steering Concept in Analog Phase Array Antenna

The history of analog beamforming technique dates back to the Butler matrix beamforming network consists of hybrid coupler and fixed phase shifters, that steers beam in discrete manner [5]. Researches on analog beam steering proliferated when analog phase shifters with continuous phase shift were proposed to replace butler matrix. Block diagram of an  $n$ -element phased array system is shown in Fig. 2.3.  $n$ -element antennas are equally spaced by a distance,  $d$ , along a linear axis. For simplicity, we discuss only the receiver case, where similar concepts are held for transmitter due to the reciprocity concepts. Separate variable time delays are incorporated at each signal path to control the phase of the signals before all the signals are combined at the power combiner. Fig. 2.3 shows plane-wave beam incidents upon the antenna array at an angle of  $\theta$  to the normal direction. Due to the spacing between the adjacent antennas, the beam reached successive antennas at different time constant.

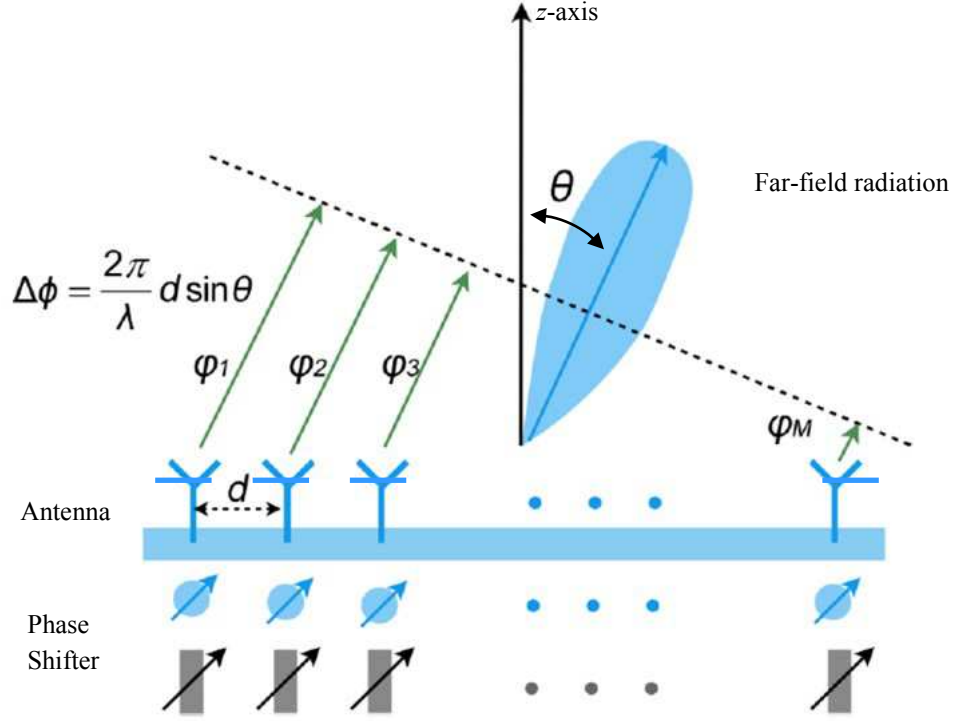


Fig. 2.3 Linear phased array antenna.

To derive array factor in linear phased array antenna, we do not consider mutual coupling between adjacent antenna elements for the sake of simplicity. Assume that all the elements in array are isotropic, and they are driven at the same phase and power, the resultant beam will radiate at broadside direction; perpendicular to the plane where they are mounted to. For broadside direction, radiation will spread along  $z$  direction in Fig. 2.3. When beam is steered, resultant field of radiated beam is a function of phase difference between adjacent antenna elements when the distance between the array elements,  $d$ , is fixed and spaced apart by one-half free space wavelength ( $\lambda_0/2$ ). If we apply a progressive phase shift to the inter-stage array elements, the beam can be directed towards desired scan angle, for example,  $\theta$ , as shown in Fig. 2.3. In general, radiation pattern of uniformly-spaced array antenna can be represented by [6]

$$S(\theta) = \sum_{n=1}^N S_{el}(\theta) S_{AF}(\theta) = S_{el}(\theta) \sum_{n=1}^N a_n e^{j(k_0(N-n)d \sin\theta + \alpha)}, \quad (2.1)$$

where  $\alpha$  represents phase taper on each path of antenna element.



$S_{el}(\theta)$  represents element factor of antenna elements,  $k_0$  is the free space wavenumber,  $\alpha$  is phase difference between adjacent antenna, and  $n$  is number of antenna elements. Array factor of linear array radiation pattern is written as

$$S_{AF}(\theta) = \sum_{n=1}^N e^{j(N-n)\Psi}, \quad (2.2)$$

where  $\Psi = k_0 d \sin(\theta) + \alpha$ . (2.3)

In eq. (2.3), we may recognise a finite geometric series. If both sides of this equation are multiplied with  $e^{j\Psi}$ , we get

$$S_{AF}(\theta)e^{j\Psi} = e^{jN\Psi} + e^{j(N-1)\Psi} + \dots + e^{j2\Psi} + e^{j\Psi}. \quad (2.4)$$

Next, eq. (2.3) is subtracted from eq. (2.5), then we obtain

$$S_{AF}(\theta)(e^{j\Psi} - 1) = (e^{jN\Psi} - 1) \quad (2.5)$$

which may be written, after splitting and rearranging the exponential terms, as

$$S_{AF}(\theta) = \frac{e^{j\frac{N\Psi}{2}}(e^{j\frac{N\Psi}{2}} - e^{-j\frac{N\Psi}{2}})}{e^{j\frac{\Psi}{2}}(e^{j\frac{\Psi}{2}} - e^{-j\frac{\Psi}{2}})} = e^{j\frac{N-1}{2}\Psi} \frac{\sin(\frac{N\Psi}{2})}{\sin(\frac{\Psi}{2})}, \quad (2.6)$$

Neglecting phase factor,  $e^{j\frac{N-1}{2}\Psi}$ ,

$$|S_{AF}(\theta)| = \left| \frac{\sin(\frac{N\Psi}{2})}{\sin(\frac{\Psi}{2})} \right|. \quad (2.7)$$

$$|S_{AF}(\theta)| = \left| \frac{\sin(\frac{N(k_0 d \sin(\theta) + \alpha)}{2})}{\sin(\frac{k_0 d \sin(\theta) + \alpha}{2})} \right|. \quad (2.8)$$

To steer beam to desired direction, progressive phase taper,  $a_n$ , must be applied to uniformly-spaced antenna elements. Separation distance between antenna elements,  $d$ , is

crucial to avoid unwanted radiation beam, known as grating lobes. Grating lobe appears when the array factor repeats itself, as reported in [3].

Grating lobes, which have same radiation strength as main beam, will appear along with the main beam if  $d$  is set too large. It occurs whenever the argument  $\Psi$  in eq. (2.4) is an integer multiple of  $2\pi$  and it can be written as

$$\Psi = m2\pi. \quad m = 1, 2, \dots, m \quad (2.11)$$

First grating lobe occurs when

$$\frac{d}{\lambda}(\sin\theta - \sin\theta_0) = m, \quad m = 1, 2, \dots, m \quad (2.12)$$

By rearranging eq. (2.12), grating lobe in uniformly-spaced phased array antenna can be avoided if separating distance between antenna elements satisfies

$$d < \frac{\lambda}{(\sin\theta - \sin\theta_0)}. \quad (2.13)$$

Fig. 2.4 shows radiation pattern of one dimension linear array antenna with and without the presence of grating lobes. Antenna elements are cosines waveform. Directivity of antenna array composed of cascading 4 identical, equidistant antenna elements is plotted. Grating lobes occur when separation distance between antenna elements  $d$  is increased from one-half guided wavelength ( $0.5\lambda_0$ ) to one wavelength ( $\lambda_0$ ).

## 2.2 Phase Shifting Techniques

Phase shifter is a core device in analog phased array radar systems, as briefed in the previous section. We will take a look on parameters in RF signal which can be manipulated to accomplish a relative phase shift in this section. Phase of signals can be derived by assuming the signals to be time harmonic, as follows:

$$s(\omega) = \cos(\omega t), \quad (2.14)$$

where  $\omega = 2\pi f$ ,  $f$  is the frequency of travelling wave.

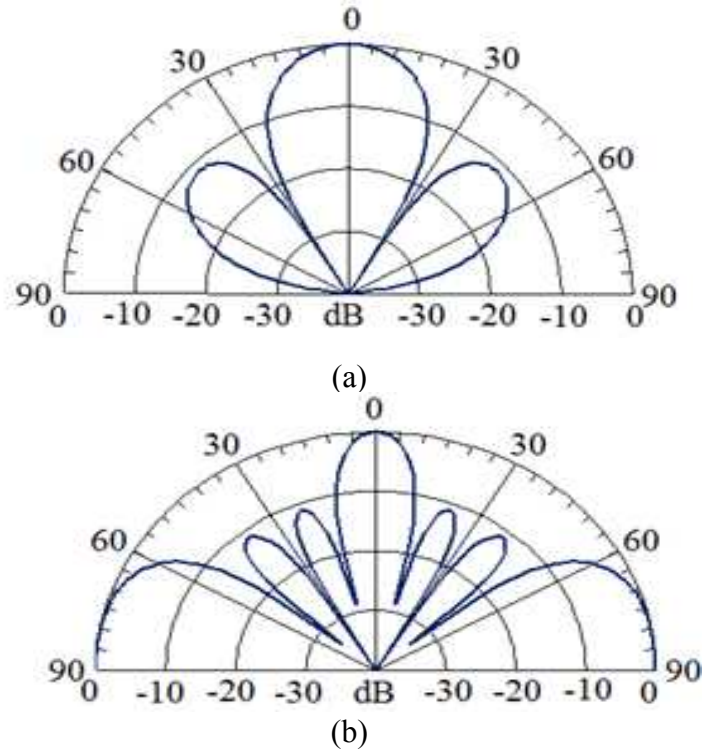


Fig. 2.4 Calculated radiation pattern of non-steering phased array antenna with  
(a)  $d = 0.5\lambda_0$  and (b)  $d = \lambda_0$ .

Time,  $t$ , is expressed as the distance,  $l$ , travelled by signal over propagation velocity of the signal  $c$ , so that we find for phase of travelling wave as,

$$\omega t = 2\pi f l \sqrt{\epsilon\mu} \quad , \quad (2.15)$$

where  $\epsilon$  is the permittivity, and  $\mu$  is the permeability of the propagation medium.

Variables  $(f, l, \epsilon, \mu)$  listed in eq. (2.15) implicitly shows all parameters required to adjust phase of a signal. Relative phase shift are achieved, as follows:

- adjusting phase by changing electrical length of transmission line ( $l$ );
- adjusting phase by varying frequency of RF signal ( $f$ );
- adjusting phase by changing permittivity of medium for signal propagation ( $\epsilon$ );
- adjusting phase by changing permeability of medium for signal propagation ( $\mu$ ).

## 2.3 Array Feeds

Feeding network is the backbone in antenna arrays, in which it combines a number of antenna elements, to achieve high gain. Required phase shift range for phased array antenna to steer beam to the maximum scan angle depends on the type of feeding network used. Generally, antenna array can be categorized based on the way antenna elements are fed in an array network. When the array elements are in series along array feed, the array is termed “series”. On the other hand, the array is termed “shunt” when the elements are in parallel with array feed. Shunt feed is also known as corporate feed. Series and corporate feeds are the most common feeding network available for phased array antenna.

### 2.3.1 Series Array Feed

Fig. 2.5 presents series-fed network consists of  $N$  antenna elements and  $(N-1)$  phase shifters connected in series. To obtain broadside radiation, antenna elements are fed in-phase and series array feed is adjusted to a particular factor of wavelength of the operating signal. Input and output impedances of each antenna must be customized individually in order to match to the transmission line’s characteristic impedance. The cumulative nature of the phase shift in series array feed enables the realization of a wide steering angle with a small phase shift range. As the signal travels away from the source in series array feed, antenna elements and phase shifters connected in series withdraw power from transmission line. For antenna elements located far away from the RF source, power delivered to the antenna elements is reduced.

When the number of elements in array antenna expands, this may lead to uneven power distribution to antenna elements that must be accounted for array factor calculation. Furthermore, accumulated phase shift in series-fed network leads to beam squint and limits operating bandwidth of phased array antenna.

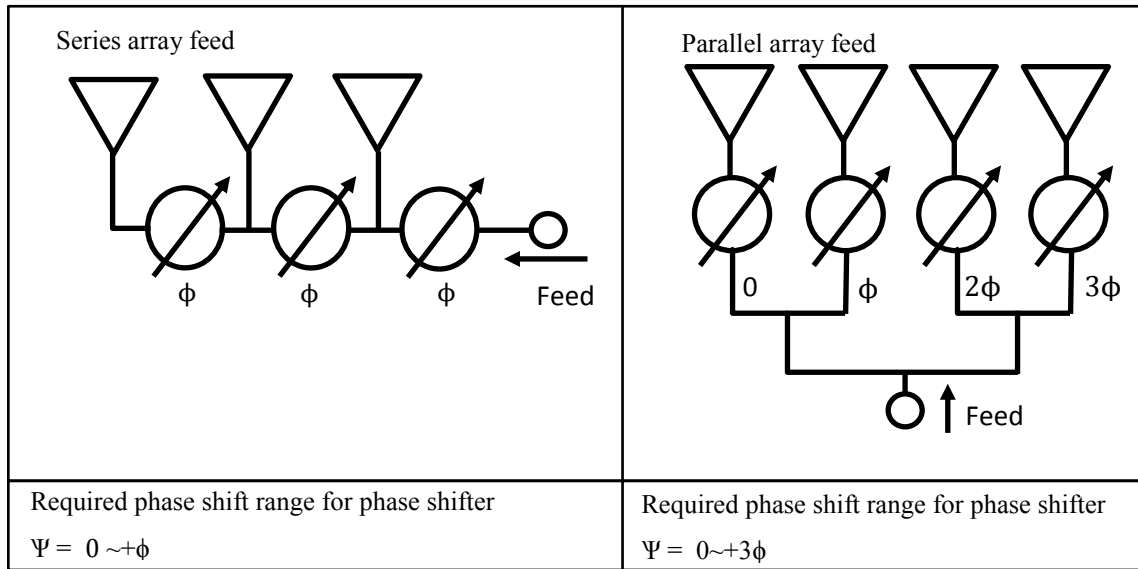


Fig. 2.5 Series and corporate array feeds.

### 2.3.2 Corporate Array Feed

Antenna elements arranged in parallel to the array feed is known as corporate-fed network.  $N$  antenna elements and  $N$  phase shifters are connected in parallel to form corporate feed. Owing to the fact that phase shifter is connected individually to antenna element, large phase shift range is required to realize wide beam steering angle. The required amount of phase shift is higher than series array feed by a factor of  $N-1$ , in which  $N$  is the number of antenna elements in the phased array system. RF power is distributed evenly to each antenna element via equally split, 2-way power dividers cascaded in nested structure as illustrated in Fig. 2.5. In corporate-fed network, distance travelled by RF signals from the source to the array elements is same in terms of electrical length.

Antenna elements in corporate-fed network are equidistant from source. This allows radiated power to be distributed uniformly to generate maximum directivity at desired angle for a given aperture size. Side lobes level in corporate-fed antenna array can be suppressed by increasing number of antenna elements or distributing non-uniform amplitude with determined optimal weights for each antenna elements.

## 2.4 Scan Angle Range of Analog Phased Array Antenna

Scan range is referred to the maximum scan angle of beam that can be steered away from broadside without the appearance of grating lobes in the principal planes. As we have seen in Fig. 2.4, grating lobes occur in the principal plane upon enlarging separation distance between antenna elements to  $\lambda_0$ . In other words, grating lobe occurs when separation distance  $d$  is more than one free space wavelength ( $d \geq \lambda_0$ ) for the broadside linear array antenna, in a non-scanning situation.

To steering beam in any angle without a grating lobe being present in the principal place, new equation is deduced from eq.(2.13) as follows,

$$d < \frac{\lambda}{|1 + \sin\theta_{max}|} . \quad (2.16)$$

Maximum scan angle without any grating lobes depends on the separation distance  $d$ . Eq. (2.13) implicitly indicates that grating lobes will appear even if separation distance between inter-stage antenna elements is kept less than one free-space wavelength, given than beam is over-steered. Fig. 2.6 shows calculated radiation pattern of 1x 4 phased array antenna with separation distance between antenna element,  $d=0.5\lambda_g$ , and progressive phase difference,  $\theta=160^\circ$ . Progressive phase difference,  $\theta$ , is chosen to violate eq. (2.16) to demonstrate the occurrence of grating lobes.

Progressive phase shift required for grating lobe-free beam steering, can be written as

$$\Delta\phi = \frac{360^\circ \cdot (d\sin\theta)}{\lambda} . \quad (2.17)$$

## 2.5 Antenna Gain and Radiation Efficiency

For direct current (DC) or alternate current (AC) transmission line, energy loss can be ignored when power is transferred from one point to another point, separated by distance,  $d$ . Power transfer efficiency in a device or transmission line is defined as the ratio of the output power divided by the input power. Resistance of material inhibits in the carrier is the primarily factor of power loss in DC transmission line.

If we take a look on high frequency signal propagation in device such as antenna, there are several factors that lead to mismatch between radiated power in the free space and power delivered to the antenna.

Similar to power transfer efficiency in other electronic device, radiation efficiency of an antenna is the ratio of the desired output power to the incident power, as follows:

$$\eta_{rad} = \frac{P_{rad}}{P_{inc}} = \frac{P_{inc} - P_{loss}}{P_{inc}} \quad (2.18)$$

where  $P_{loss} = L_{cond} + L_{diel} + L_{imp}$ . (2.19)

$P_{rad}$  is the far-field radiated power of the antenna,  $P_{inc}$  is the incident power supplied to the antenna, and  $P_{loss}$  is the power loss suffered by the antenna due to the imperfection of dielectric materials used and impedance mismatch between high frequency devices. Eq. (2.19) shows power loss suffered by the antenna when RF signals radiate in far-field.  $L_{cond}$  represents ohmic loss caused by imperfection in the conductors of radiator and ground plane.  $L_{diec}$  is a dielectric loss occurs in dielectric materials as RF signals propagate in the dielectric medium. Dielectric loss happened because a portion of RF energy is absorbed by the dielectric material and converted into heat.

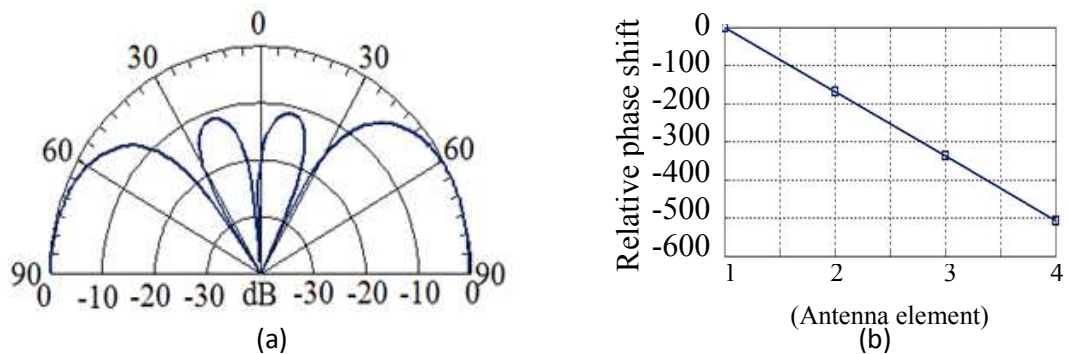


Fig. 2.6 Calculated radiation pattern of 1x4 phased array antenna with  $d=0.5\lambda_g$  and  $\theta=180^\circ$ . (a) Normalized radiation pattern. (b) Phase difference  $\theta$  between antenna elements.

For an ideal case, the current leads the voltage by  $90^\circ$  for any RF signals propagate in propagation medium with permittivity  $\epsilon_r = 1$ , such as free space. In the lossy dielectric medium, incident current does not lead the voltage by  $90^\circ$  as shown in Fig. 2.7 (b). Lag angle,  $\theta_d$ , is known as dielectric loss angle. Loss in a dielectric material can be expressed as

$$L_{diec} = VI \cos \theta_d = VI \cos(90 - \phi_d) \quad (2.20)$$

As such, propagation loss in the dielectric medium can be expressed as follows:

$$L_{diec} = VI \sin \phi_d, \quad (2.21)$$

For smaller value of  $\phi_d$

$$L_{diec} = VI \tan \phi_d \quad (2.22)$$

to represent lag angle between current and voltage vector of RF signals propagate in dielectric medium.  $\tan \phi_d$  is a tangent loss of the dielectric medium; it can be written as

$$\tan \phi_d = \frac{\epsilon_r''}{\epsilon_r'} \quad (2.23)$$

where  $\epsilon_r'$  and  $\epsilon_r''$  are the real and imaginary part of the dielectric constant, respectively.

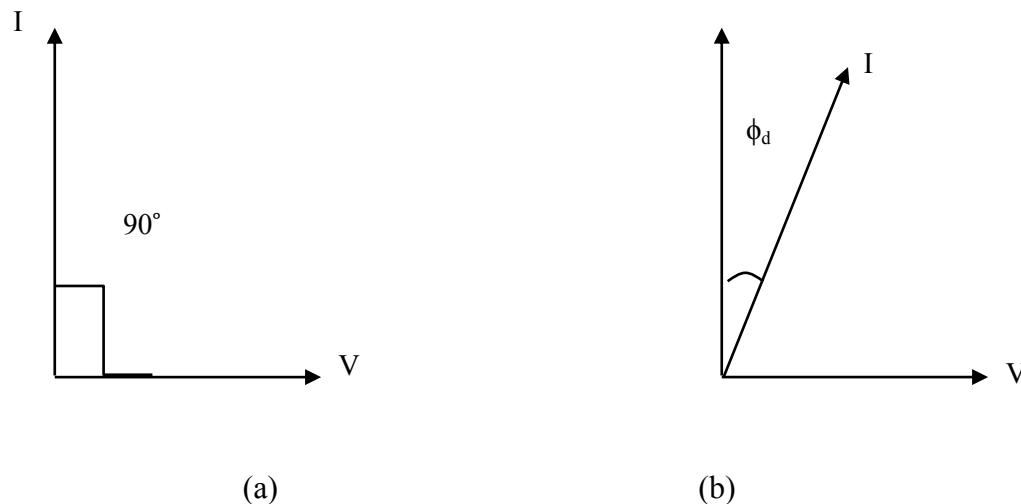


Fig. 2.7 Phase between current I and voltage v, (a) Ideal case, and (b) lossy dielectric medium.



$L_{imp}$  represents mismatch loss due to impedance mismatch between antenna and feed line. Let's consider antenna input impedance as  $Z_{ant}$  and feed line's characteristic impedance as  $Z_{feed}$ . Reflection coefficient,  $\Gamma$ , is used to describe amount of an electromagnetic wave reflected from antenna due to impedance mismatch. It can be written, as follows [7] :

$$\Gamma = \frac{E^-}{E^+} = \frac{Z_{ant} - Z_{feed}}{Z_{ant} + Z_{feed}}, \quad (2.24)$$

where  $E^-$  is reflected wave and  $E^+$  is incident wave. Mismatch loss,  $L_{imp}$  can be expressed as

$$L_{imp} = -20 \log(1 - \Gamma^2). \quad (2.25)$$

## 2.6 Chapter Summary

A brief introduction to the architectures and principles of operation of a phased array was discussed. Beamforming network can be realized using either analog or digital architectures, depends on the system requirements. Digital phased array antenna can steer multiple beams simultaneously. In digital beamforming, power consumption in ADCs and its processor escalates for the devices to keep up with the growth in design complexity to accomodate high sampling rate. In analog beamforming, its architecture is less complex, and the phased array system consumes less power than its digital counterparts. Next, travelling wave as cosine wave is considered in deriving factors that influence phase of travelling wave. Phase of the travelling wave can be tuned by changing the parameters of the factors derived, such as transmission line length, substrate permittivity and permeability. Other characteristics of phased array antenna, such as beam steering principle, scan angle, antenna factor, and radiation efficiency, were also discussed.

### References

- [1] E. Everett, C. Shepard, L. Zhong, and A. Sabharwal, “SoftNull: Many-Antenna Full-Duplex Wireless via Digital Beamforming,” *IEEE Trans. on Wireless Comm.*, Vol. 15, no. 12, pp. 8077-8092, Dec. 2016
- [2] C. Ward, P. Hargrave, and J. McWhirter, “A novel algorithm and architecture for adaptive digital beamforming,” *IEEE Trans. Antennas Propag.*, vol. 34, no.3, pp. 338 -346, March 1986.
- [3] S. Denno, and T. Ohira, “Modified constant modulus algorithm for digital signal processing adaptive antennas with microwave analog beamforming,” *IEEE Trans. Antennas Propag.*, vol. 50, no.6, pp. 850-857, June 2002
- [4] D. R. Banbury, N. Fayyaz, S. Safavi-Naeini, and S. Nikneshan, “A CMOS 5.5/2.4 GHz dual-band smart-antenna transceiver with a novel RF dual-band phase shifter for WLAN 802.11a/b/g,” in *IEEE RFIC Symp.*, pp. 157–160, Jun. 2004.
- [5] J. Butler et al., “Beamforming matrix simplifies design of electronically scanned antennas,” *Electron. Design*, vol. 9, pp.170-173, April 1961
- [6] Robert C. Hansen, “Phased Array Antennas,” 2nd edition, Wiley Press, Nov. 2009.
- [7] David M. Pozar, “Microwave Engineering,” 4<sup>th</sup> edition, Wiley Press, Nov. 2012.

## Chapter 3

### Linear Array Antenna

Microstrip patch antennas are compact, low profile and easy to design that makes the antennas extremely useful in many wireless applications. In recent years, considerable attention has been given to widening the operating bandwidth of the microstrip patch antenna. Numerous methods to increase the bandwidth of the antenna, including aperture coupling, stacking substrates with different permittivity and deployment of low dielectric substrate, had been reported [1],[2], [4]. Work in [4] shows that the antenna gain and substrate thickness are mutually conflicting, that is, the use of thin substrate causes degradation in the realized gain of the antenna. A coplanar waveguide (CPW)-fed unidirectional slot antenna was proposed to overcome the problem stated in [5].

Antenna operates at 8.5 GHz offers wider bandwidth compared to frequencies operate at industrial, scientific, and medical (ISM) bands, especially 2.5 GHz and 5 GHz. Increase in substrate thickness enhances realized gain of antenna. Subsequently, the size of distributed elements phase shifter is increased if substrate with the same thickness were used in phase shifter design. To achieve low-profile and compact size array antenna, multiple layers PCB is required to combine antennas and feeding network on substrate with difference thickness.

This chapter presents antenna elements that are excited by upper two copper layers of four layers PCB through proximity coupling. Proposed structure alleviates gain degradation caused by thin substrate. The proposed antenna requires only two substrate layers, instead of 3 layers required by the conventional aperture coupled microstrip patch.

The proposed method also reduces width mismatch between antenna elements and feeding network in multi-layer PCB. In order to validate our idea, 1x4 array antenna is fabricated and measured.

### 3.1 Antenna Design [3]

#### 3.1.1 Antenna Geometry

Fig. 3.1 illustrates the geometry of the proposed antenna. Patch antenna is etched on the top layer with the length  $l_p$  and width  $w_p$  are calculated using transmission-line model [8]. The radiating patch is excited electromagnetically by 2 layers feed line, having width of  $w_{f2}$  on the external layer, and width of  $w_{f1}$  on the internal layer. External feed line is electrically connected to internal feed line placed beneath radiating patch through metal via. A slot is etched at the center of the patch to excite energy from the internal feed line.

Referring to cavity model in [6], a rectangular microstrip antenna can be represented as an array of two radiating narrow apertures; patch width of  $w_p$  is separated by a distance of  $l_p$ . Charge distribution in the cavity model is explained from the formation of the fields within the cavity is explained. When the microstrip patch is excited, potential difference is formed on the top patch, feed line and bottom ground plane. Charge movement due to potential difference causes edges of the patch to radiate.

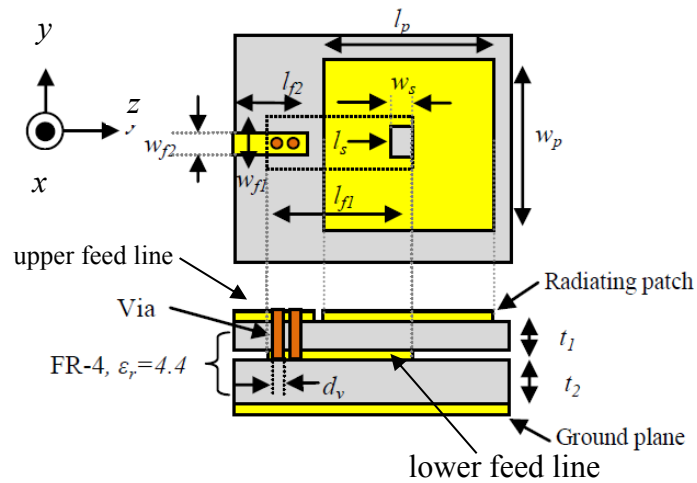


Fig. 3.1 Geometry of the proposed antenna.

Then, a charge distribution is established on the upper and lower surfaces of the patch and internal feed line, as well as on the surface of the ground plane, as shown in Fig. 3.2.

There are two mechanisms that control charge distribution: an attractive mechanism and a repulsive mechanism [7]. The attractive mechanism refers to electromagnetic force related to corresponding opposite charges on the bottom surface of the patch and the front surface of internal feed line; and opposite charges on the bottom surface of the internal feed line and the front surface of ground plane. The repulsive mechanism refers to the charge that is pushed to the edges, and drifts to top surfaces of patch, internal feed line and ground plane. The motion and interaction of charges creates electric field line associated to the standing wave inside the patch. In cavity model, we assume tangential magnetic field is small (ideally zero) and side walls are formed along the perimeter of the patch as perfect magnetic layer. In this situation, the cavity is a lossless model because input impedance consists of reactive components only. In practice, the size of ground plane is larger than patch as shown in Fig. 3.2. Charges flow to the edge of the patch and create fringing field to generate radiation. Fringing fields at the edges of the patch, which are separated by one-half guide wavelength ( $\lambda_g/2$ ), are in-phase. Fringing fields combine and reinforce radiation to the broadside direction.

As we know, magnetic current  $M_s$  flows along the periphery of the cavity is the only nonzero current components in the cavity. Fringing field strength depends on the magnetic current, whereas fringing fields increase when magnetic current density increases. In this study, internal feed line is proposed to excite slotted antenna via proximity coupling to increase magnetic current density.

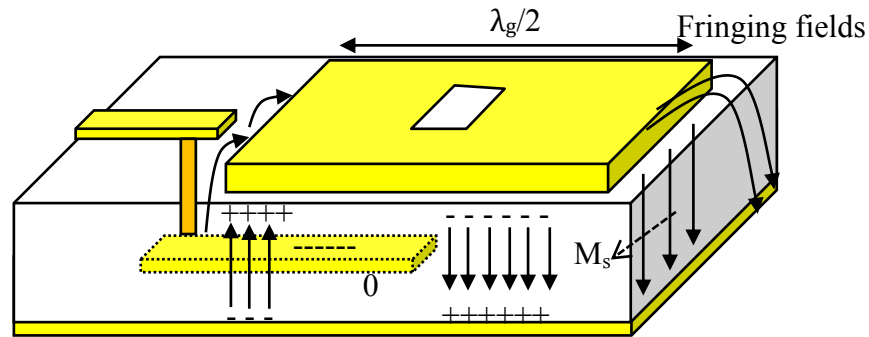


Fig. 3.2 Electromagnetics field distribution in patch.

### 3.1.2 Antenna Resonant Frequency

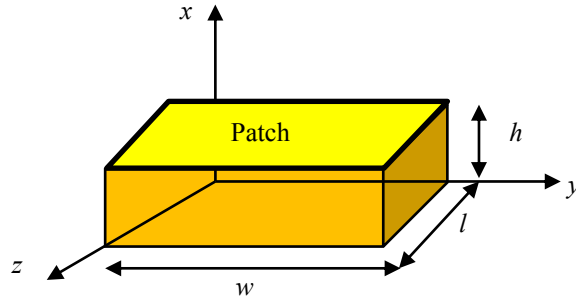


Fig. 3.3 Structure of rectangular patch antenna.

Field density in the cavity analyzed using vector potential approach was demonstrated in [8]. The authors consider the dielectric substrate as truncated and not extended beyond the edges of the patch. The vector potential  $A_x$  must satisfy the homogenous wave equation of

$$\nabla^2 A_x + k^2 A_x = 0 \quad (3.1)$$

where  $A_x$  is derived in [8] using separation of variables, as follows:

$$A_x = [A_1 \cos(k_x x) + B_1 \sin(k_x x)] [A_2 \cos(k_y y) + B_2 \sin(k_y y)] \cdot [A_3 \cos(k_z z) + B_3 \sin(k_z z)] \quad (3.2)$$

$k_x, k_y$  and  $k_z$  are the propagation wavenumber along  $x, y$ , and  $z$  directions, respectively. Electric and magnetic fields within the cavity are related to the vector potential  $A_x$ , as follows:

$$\left. \begin{aligned} E_x &= -j \frac{1}{\omega \mu \epsilon} \left( \frac{\partial^2}{\partial x^2} + k^2 \right) A_x, & H_x &= 0 \\ E_y &= -j \frac{1}{\omega \mu \epsilon} \left( \frac{\partial^2 A_x}{\partial x \partial y} \right), & H_y &= \frac{1}{\mu} \frac{\partial A_x}{\partial z} \\ E_z &= -j \frac{1}{\omega \mu \epsilon} \left( \frac{\partial^2 A_x}{\partial x \partial z} \right), & H_z &= -\frac{1}{\mu} \frac{\partial A_x}{\partial y} \end{aligned} \right\} \quad (3.3)$$

Boundary conditions are applied to show that  $B_1$ ,  $B_2$  and  $B_3$  are equal to zero. The final form for vector potential  $A_x$  in eq. (3.2) can be written as,

$$A_x = A_{mnp} \cos(k_x x) \cos(k_y y) \cos(k_z z) \quad (3.4)$$

where  $A_{mnp}$  represents the amplitude coefficients of excitation mode. Propagation constant in  $x$ ,  $y$  and  $z$ -axis are equal to

$$\left. \begin{aligned} k_x &= \left(\frac{m\pi}{h}\right), \quad m = 0, 1, 2, \dots \\ k_y &= \left(\frac{n\pi}{l}\right), \quad n = 0, 1, 2, \dots \\ k_z &= \left(\frac{p\pi}{w}\right), \quad p = 0, 1, 2, \dots \end{aligned} \right\} m=n=p \neq 0 \quad (3.5)$$

The resonant frequencies of the cavity can be estimated, as follows:

$$(f_r)_{mnp} = \frac{1}{2\pi\sqrt{\mu\epsilon}} \sqrt{\left(\frac{m\pi}{h}\right)^2 + \left(\frac{n\pi}{l}\right)^2 + \left(\frac{p\pi}{w}\right)^2} \quad (3.6)$$

For patch antenna with high length-to-height ratio ( $l/h$ ) and length-to-width ( $w/h$ ) ratio, dominant mode of antenna radiation occurs at the lowest order of resonant frequency. The dominant mode of wave is  $TM_{010}^x$  mode, resonant frequency is written as

$$(f_r)_{010} = \frac{1}{2l\sqrt{\mu\epsilon}} = \frac{v_0}{2l\sqrt{\epsilon_r}} \quad (3.7)$$

where  $v_0$  and  $\epsilon_r$  are the wave velocity in free-space and permittivity of propagation medium, respectively. Second order mode  $TM_{020}^x$  can be excited by setting the patch dimension to  $l/2 > w$  and  $w > h$ . Resonant frequency is expressed as

$$(f_r)_{020} = \frac{1}{l\sqrt{\mu\epsilon}} = \frac{v_0}{l\sqrt{\epsilon_r}} \quad (3.8)$$

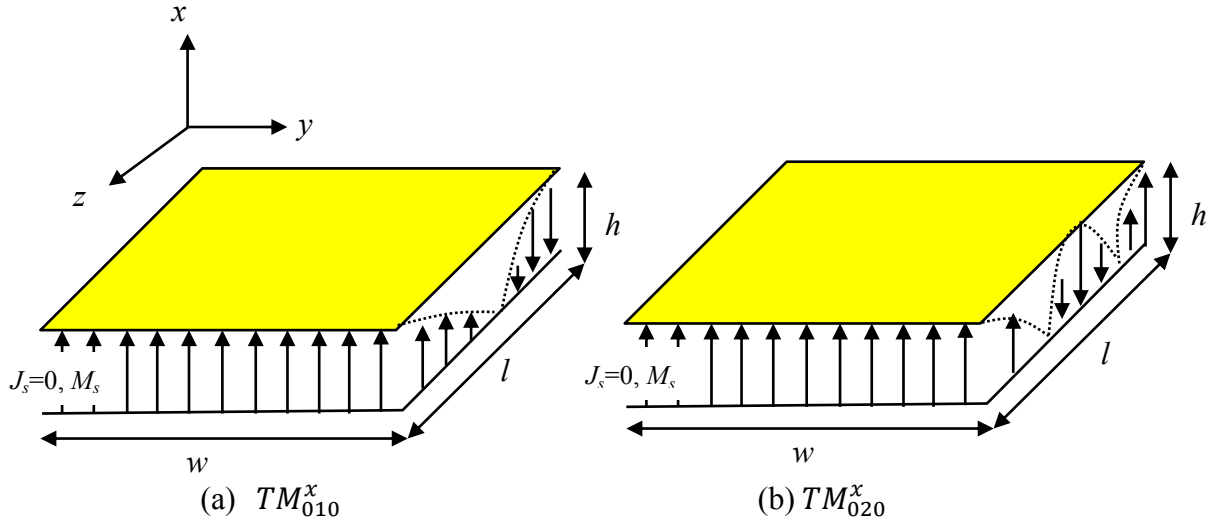


Fig. 3.4 Excitation modes of rectangular patch antenna. (a)  $TM_{010}^x$ . (b)  $TM_{020}^x$

### 3.1.3 Fields Radiated in Patch in $TM^x$ Mode

The simplest mode of excitation is  $TM_{010}^x$ . Four perfectly conducting magnetic walls are treated as narrow slots in cavity model. Fields radiated by slots at  $xz$ -plane are separated by the length of the patch  $l$ . They are out of phase and cancel each other along the principal planes. Another two slots separated by the width of the patch  $w$ , approximately  $\lambda_g/2$ , has in-phase fringing fields to generate far-field radiation in the broadside direction ( $x$ -axis). Equivalent electric current  $J_s$  and equivalent magnetic current  $M_s$  at the surface of the slots shown in Fig. 3.4, can be expressed as

$$J_s = \vec{n} \times H_a \quad (3.9)$$

$$\text{and} \quad M_s = -\vec{n} \times E_a \quad (3.10)$$

where  $E_a$  and  $H_a$  represent the electric and magnetic fields at the slots.  $\vec{n}$  is the vector normal to the surface of the slots. Electric current density  $J_s$  is extremely small and it is negligible. We only consider equivalent magnetic current density  $M_s$  as the only current source in the patch. According to image theory,  $M_s$  becomes twice of its original value when large ground plane is present. The final magnetic current density is

$$M_s = -2\vec{n} \times E_a \quad (3.11)$$

along the side periphery of the radiating slots.



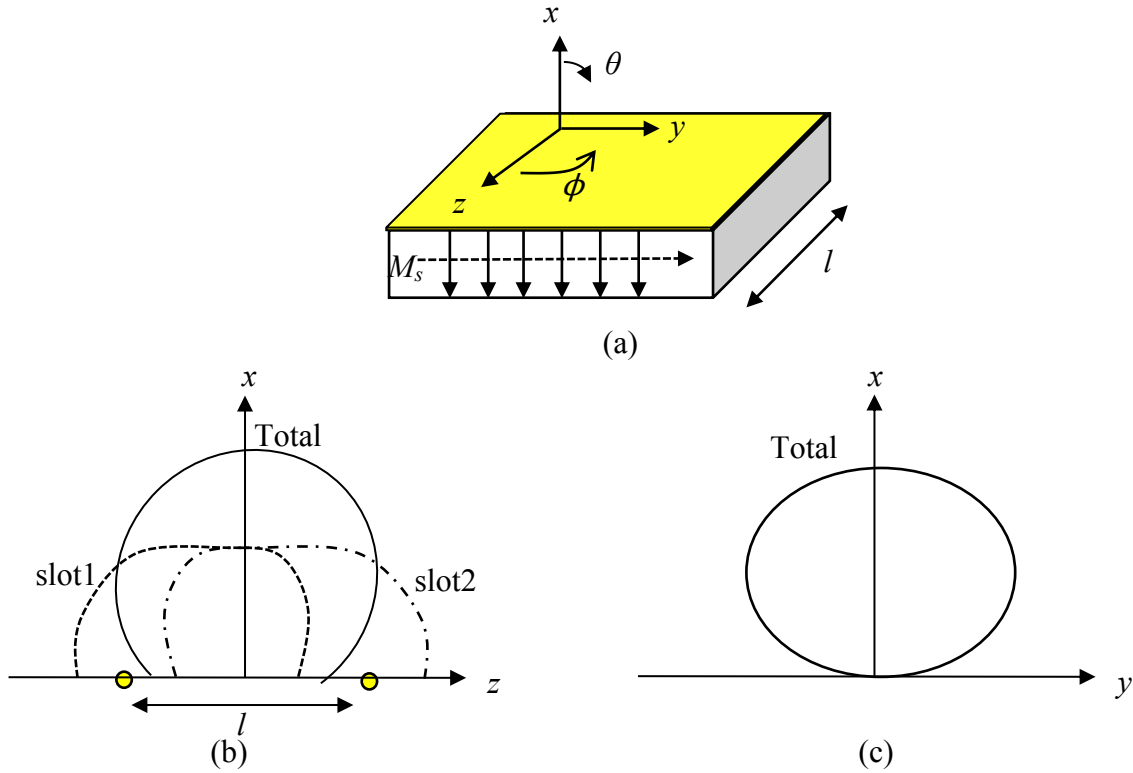


Fig. 3.5 Perspective view of the patch and its radiation pattern. (a) Perspective view, (b)  $xz$ -plane pattern, and (c)  $xy$ -plane pattern.

The array factor for two radiating slots separated by the length of the patch  $l$  along  $z$ -axis,

$$(AF)_z = 2\cos\left(\frac{k_0 l_e}{2} \sin\theta \sin\phi\right) \quad (3.12)$$

where  $l_e$  is the effective length of the patch. Figs. 3.5(b) and 3.5(c) show  $xz$ -plane and  $xy$ -plane with total electric fields are given as

$$E(\theta) = +j \frac{k_0 w V e^{-jk_0 r}}{\pi r} \left\{ \frac{\sin\left(\frac{k_0 h \cos\theta}{2}\right)}{\left(\frac{k_0 h \cos\theta}{2}\right)} \right\} \cos\left(\frac{k_0 l_e}{2} \sin\theta\right) \quad (3.13)$$

for  $\phi=90^\circ$ ,  $0^\circ \leq \theta \leq 360^\circ$  (E-plane), where  $k_0$  is the free space wave number,  $r$  is the far field radiation point, and  $V$  is the voltage across the slot ( $V=hE_0$ ).

### 3.1.4 Antenna Input Impedance

Full-wave electromagnetic simulation tool (HFSS, ANSYS) was used to run parametric analysis of  $w_{f2}$ -to- $w_{f1}$  ratio, shown in Fig. 3.1.  $w_{f2}$ -to- $w_{f1}$  ratio is a parameter used to adjust input impedance of proposed antenna. Slot is etched at the center of the patch by 0.5 mm x 1 mm so that the patch can be excited through permittivity coupling. Fig. 3.6 shows changes in input impedance of the slotted patch when  $w_{f2}$ -to- $w_{f1}$  ratio is changed from 1 to 3. It is noticed that antenna becomes more capacitive when the ratio increases from 1 to 3. Optimum ratio is obtained as 1.5 as depicted in Fig. 3.6. Optimized design parameters of the proposed antenna are listed in Table 3.1. Length of the patch,  $l_p$  is set to 7.6 mm using eq. (3.7), and optimum width of the patch,  $w_p$  is obtained as 13 mm. Proposed patch radiates at the edges along  $y$ -axis, as depicted in Fig. 3.5(a)

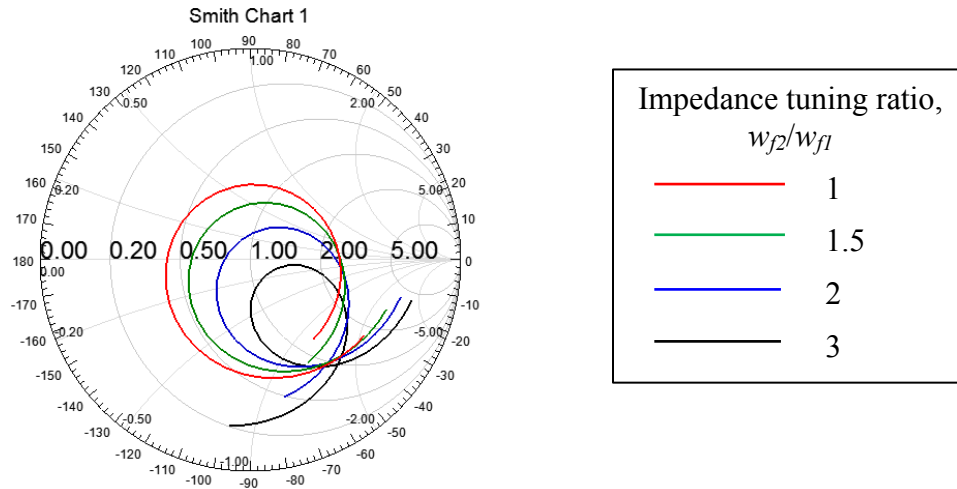


Fig. 3.6 Antenna input impedance in response to  $w_{f2}$ -to- $w_{f1}$  ratio.

Table 3.1 Design parameters of the proposed antenna.

$w_p$	$l_p$	$w_{f1}$	$l_{f1}$	$w_{f2}$	$l_{f2}$	$w_s$	$l_s$	$t_1$	$t_2$	$d_v$
13	7.6	3.4	5	1.6	5	0.5	1	0.25	1.24	0.65
(unit in mm)										

### 3.1.5 Antenna Array Principle

Antenna array consists of a set of identical antenna elements positioned in a linear line. For simplicity, antenna array comprised of equally-spaced antenna elements and equal amplitude is considered. Incoming waves arrive at point source 2 and the travelled distance are shorter than the waves arrive at point source 1, as illustrated in Fig. 3.7. Assume that the phase of the arriving wave at point source 1 is equal to zero, the corresponding phase of waves at point source 2 corresponding to the point source 1 is  $\xi = \beta d \cos \theta$ . Each point source leads its nearest neighbor on the left by the same spatial phase delay of  $\xi$ . Using this results, array factor AF is written as,

$$\begin{aligned} AF &= A_0 + A_1 e^{j\beta d \cos \theta} + A_1 e^{j\beta 2d \cos \theta} + \dots + A_1 e^{j\beta n d \cos \theta}, \\ &= \sum_{n=1}^N A_n e^{j\beta (N-n) d \cos \theta}. \end{aligned} \quad (3.14)$$

Consider that phased array system has a linear progressive phase shift between adjacent elements, eq. (3.14) is then written as,

$$AF = \sum_{n=1}^N A_n e^{j\beta (N-n)(d \cos \theta + \alpha)}. \quad (3.15)$$

Consider that current has a linear phase progression, we can separate the phase explicitly as,

$$A_n = A_n e^{jn\alpha}. \quad (3.16)$$

Array factor is a function of  $\psi = \beta(d \cos \theta + \alpha)$ . When two elements are spaced apart by one-half of free-space wavelength ( $\lambda_0/2$ ) without any phase weight applied to the elements ( $\alpha=0$ ),  $\psi$  is expressed as

$$\psi = \beta n(d \cos \theta) = \pi \cos \theta. \quad (3.17)$$

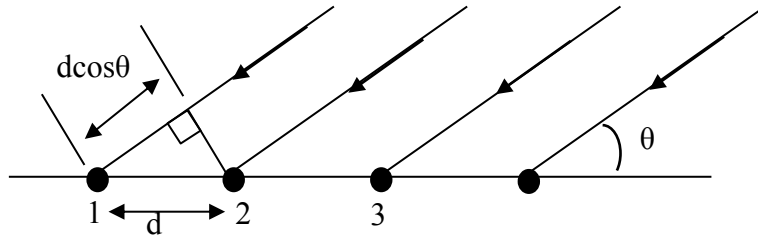


Fig. 3.7 Linear array consists of isotropic point sources equally-spaced with distance  $d$ .

Array factor for two elements array is

$$AF = 1 + e^{j\beta d \cos \theta} = e^{j\frac{\beta d \cos \theta}{2}} \left( e^{-j\frac{\beta d \cos \theta}{2}} + e^{j\frac{\beta d \cos \theta}{2}} \right) \quad (3.18)$$

and  $\beta d/2 = \pi/2$  when  $d = \lambda/2$ , array factor is simplified as,

$$AF = 2e^{j\left(\frac{\pi}{2}\cos\theta\right)} \cos\left(\frac{\pi}{2}\cos\theta\right). \quad (3.19)$$

Replacing eq. (3.17) into eq. (3.19), array factor  $\psi$  is written as,

$$AF(\psi) = 2e^{j\left(\frac{\psi}{2}\right)} \cos\left(\frac{\psi}{2}\right), \quad (3.20a)$$

$$|AF(\psi)| = 2\cos^2\left(\frac{\psi}{2}\right) \quad (3.20b)$$

Eq. (3.20b) is obtained if we only extract absolute value from the array factor. The magnitude of array factor is then plotted as a function of  $\psi$  in numeric computing software, as shown in Fig. 3.8. Note that the maximum array factor of two elements antenna array occurs at broadside when  $\theta=0^\circ$  and  $\psi=0$ . Another concern in designing antenna array is the grating lobes discussed in chapter 2. Distance between adjacent antenna elements has to be set to one-half of free-space wavelength to prevent the appearance of grating lobes.

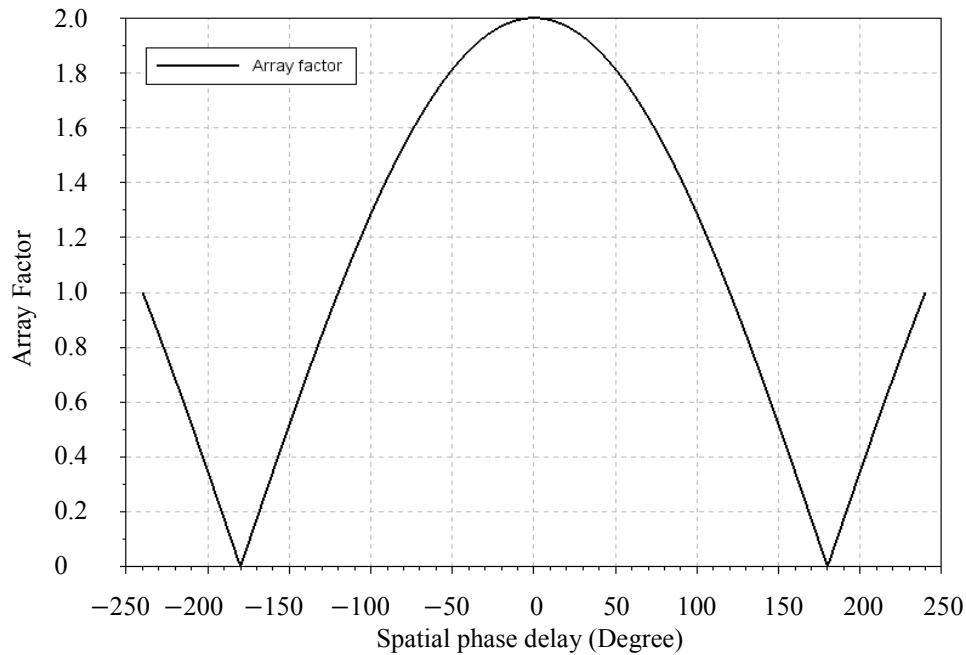


Fig. 3.8 Array factor of two antenna elements versus spatial phase delay,  $\psi$ .

### 3.2 Wilkinson Power Divider

Array antenna can be cascaded using series-fed or corporate-fed networks. Microwave power dividers in either 3 ports or 4 ports are available to distribute power to the antenna array. It divides input signal to two or more output signals of lesser power. Power dividers can be customized to divide output power equally or unequally in power division ratio, as shown in Fig. 3.9(a). Wilkinson power divider is selected in this study because input and output ports can be matched to  $50\ \Omega$  and isolation between two output ports is good. For other power dividers, i.e. T-junction and resistive power divider, all ports can be matched  $50\ \Omega$  at the expense of low isolation and additional loss from matching circuit. Fig. 3.9(b) shows the geometry of Wilkinson power divider. Scattering parameters (S-parameter) of the output and input ports are analyzed using even and odd mode analysis to demonstrate the characteristic of Wilkinson power divider.

Wilkinson power divider can be constructed based on arbitrary power division ratio, as depicted in Fig. 3.9(a). For simplification,  $-3\ \text{dB}$  equally split power divider is analyzed in the following example. Fig. 3.10 shows equivalent circuit of Fig. 3.9(b) when direct and coupling ports are sourced by even or odd mode voltage sources.

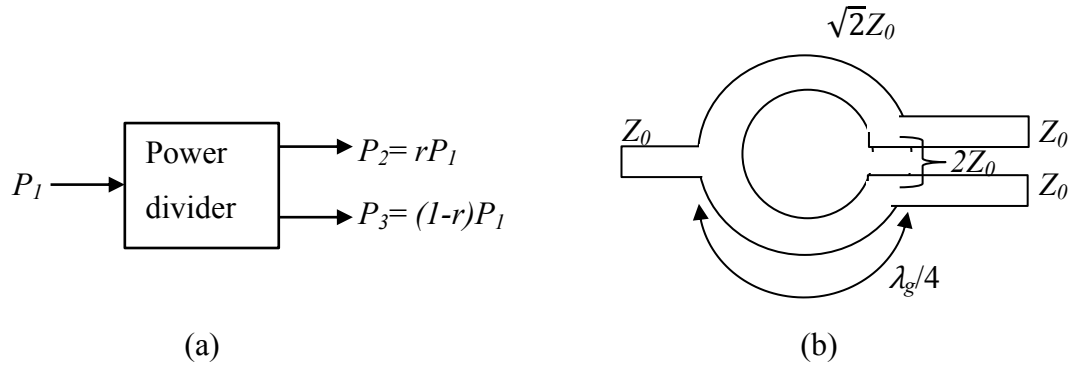


Fig. 3.9 Three ports power divider. (a) Power divider with dividing ratio ,  $r$ .  
(b)Wilkinson power divider.

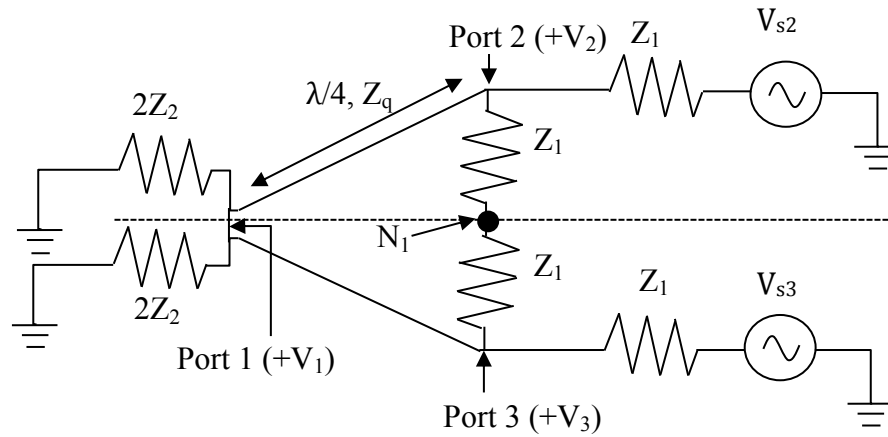


Fig. 3.10 Transmission line circuit model of Wilkinson power divider.

Numerical analysis is performed on this model by using symmetric and antisymmetric sources at the output ports. Even-odd mode analysis technique found in [9] is elaborated to analyze Wilkinson power divider.

Even mode analysis: Output ports are connected to the voltage generators,  $V_{s2}$  and  $V_{s3}$ . Currents from voltage sources cancel each other at node  $N_1$ , and thus  $N_1$  becomes virtually open.  $V_{s2}=V_{s3}=V_s/2$ , in even mode. Voltage at port 2 and port 3 are obtained as

$$V_2^e = V_3^e = \frac{V_s}{2} \left( \frac{Z_1}{Z_1 + Z_1} \right) = \frac{V_s}{4}, \quad (3.21)$$

given that length between port 1 and port 2 or 3 is a one-quarter of guided wavelength.

Even mode voltage at port 1 can be found using telegrapher's equation and it is given as,

$$V_1^e = \frac{-jV_s}{2\sqrt{2}} \quad (3.22)$$

Odd mode analysis: Output ports are connected to the voltage generators,  $V_{s2}$  and  $V_{s3}$ . Voltages at port 2 and port 3 has same amplitude but different polarity, thus  $N_1$  becomes virtually short. In odd mode,  $V_{s2} = -V_{s3} = V_s/2$ , voltages at port 2 and port 3 are obtained as

$$V_2^o = \frac{V_s}{2} \left( \frac{Z_1}{Z_1 + Z_1} \right) = \frac{V_s}{4}, \quad (3.23)$$

$$V_3^o = -\frac{V_s}{4}. \quad (3.24)$$

Odd-mode voltage at port 1 is zero when anti-symmetrical power sources are used. The connection at port 1 is a virtually short circuit because the polarity of  $V_{s2}$  and  $V_{s3}$  is in opposite direction. Therefore,

$$V_1^o = 0 \quad (3.25)$$

Superposition analysis is used in the analysis to find voltage at port 1, 2 and 3. The resultant voltages are tabulated in Table 3.2.

Now, voltage source is injected into port 2 while port 1 and 3 are terminated to match transmission line characteristic impedance. Let's assume that source impedance is matched to the transmission line characteristic impedance, thus minimum standing wave occurs, as illustrated in Fig. 3.11. Total voltage at port 2 is

$$V_2 = V_2^+ + V_2^- = \frac{V_s}{2} + V_2^-. \quad (3.26)$$

$V_2^- = 0$  V when the source impedance is matched to the transmission line characteristic impedance. Thus, incident wave  $V_2$  transmitted from the source at port 2 is  $V_s/2$ .

Eqs. (3.21) to (3.26) are used to derive S parameters of Wilkinson power divider, as follows:

$$S_{12} = \frac{V_1^-}{V_2^+} = \left( \frac{-jV_s}{2\sqrt{2}} \right) \frac{2}{V_s} = \frac{-j}{\sqrt{2}} \quad (3.27)$$

$$S_{22} = \frac{V_2^-}{V_2^+} = (0) \frac{2}{V_s} = 0 \quad (3.28)$$

$$S_{32} = \frac{V_3^-}{V_2^+} = (0) \frac{2}{V_s} = 0 \quad (3.29)$$

From the symmetricity of passive network,

$$S_{12} = S_{13} = \frac{-j}{\sqrt{2}}, S_{22} = S_{33} = 0, S_{23} = S_{32} = 0 \quad (3.30)$$

and  $S_{12} = S_{21} = \frac{-j}{\sqrt{2}}, S_{31} = S_{13} = \frac{-j}{\sqrt{2}} \quad (3.31)$

are obtained from reciprocity theorem. Table 3.3 describes the characteristics of Wilkinson power divider based on S-parameter obtained from eq. (3.27) to (3.31).

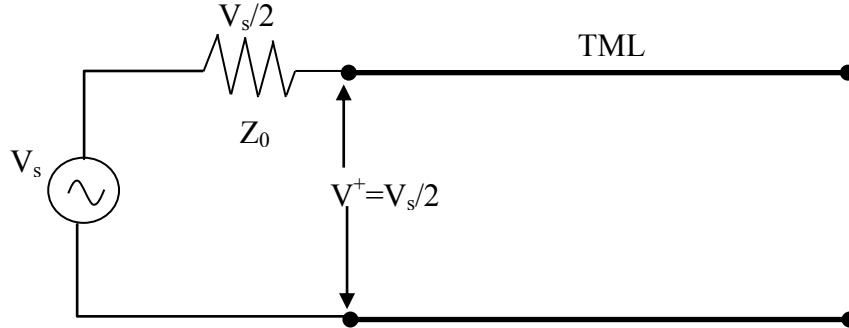


Fig. 3.11 Power source with source impedance matched to the transmission line.

Table 3.2 Net voltages from superposition analysis.

Port (Fig. 3.10)	$V_n^e + V_n^o$	Total voltage
1	$\frac{-jV_s}{2\sqrt{2}} + 0$	$\frac{-jV_s}{2\sqrt{2}}$
2	$V_s/4 + V_s/4$	$V_s/2$
3	$V_s/4 + (-V_s/4)$	0



Table 3.3 Wilkinson power divider S parameters at input and output ports.

S-parameter	Description
$S_{11} = S_{22} = S_{33} = 0$	All ports are matched when ports are terminated with matched loads.
$S_{21} = S_{12} = \frac{-j}{\sqrt{2}}$	Symmetry due to reciprocity
$S_{31} = S_{13} = \frac{-j}{\sqrt{2}}$	Symmetry due to reciprocity
$S_{23} = S_{32} = 0$	Port 2 and port 3 are isolated. Ideally, no power is dissipated by the resistor placed between port 2 and 3.

### 3.3 Simulation and Measurement Results of Proposed Antenna Array

Antenna elements discussed in Section 3.1 are cascaded as 1x4 antenna array. It was simulated using full-wave electromagnetic simulation tool (HFSS from ANSYS). Fig. 3.12 shows the comparison of simulated antenna gain of conventional patch antenna and proposed antenna. Substrate thickness is varied from 0.8 mm to 1.6 mm in the simulation. It is observed that realized gain degradation in the proposed antenna ( $\Delta G1$ ) with respect to the reduction of substrate thickness is less severe compared to the one in conventional patch antenna ( $\Delta G2$ ).

Fig. 3.13 shows the proposed antenna array. It was fabricated on FR-4 ( $\epsilon_r=3.8$ ,  $\tan \delta=0.02$ ) with multi-layer PCB manufacturing process with substrate thickness of 1.6 mm. Antenna elements were fabricated on 1.6 mm FR-4 while corporate-fed network consists of Wilkinson power divider was fabricated on 0.25 mm FR-4. Reflection coefficient ( $S_{11}$ ) of the array antenna was measured using Keysight 8722C Network analyzer (Fig. 3.14). Prior to the gain measurement, distance between transmitter array antenna and receiver array antenna was determined and transmitter power was measured ( $S_{21}$ ). Realized gain of the array antenna was calculated using Friss transmission equation. Measurements of radiation pattern in E-plane and H-plane were conducted in anechoic chamber, as depicted in Fig. 3.15.

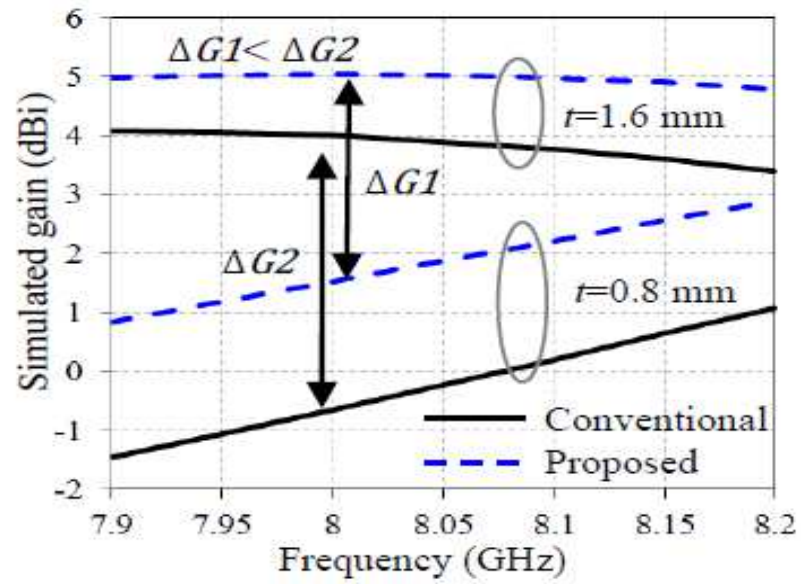


Fig. 3.12 Gain drop in conventional patch antenna and proposed antenna at xz-plane, in response to substrate thickness reduction.

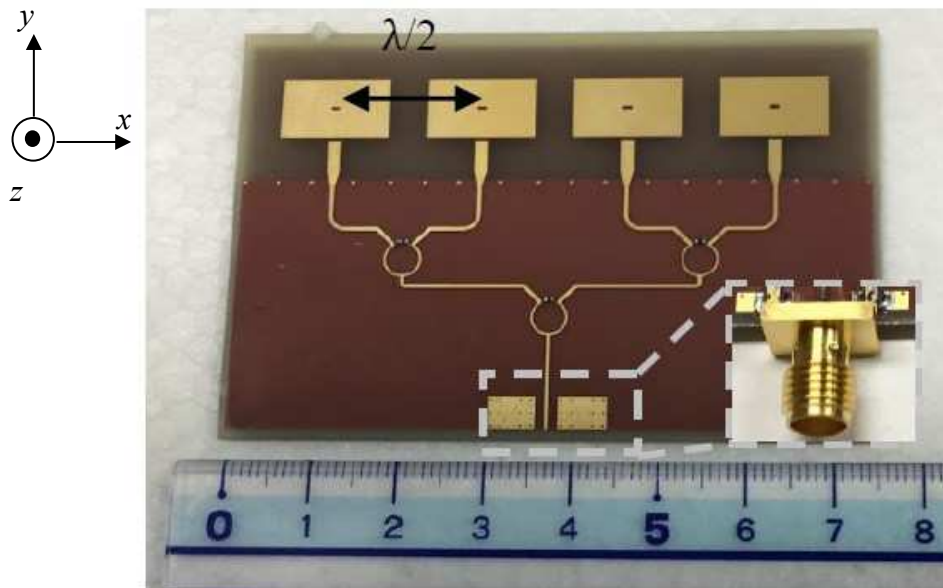


Fig. 3.13 Photograph of the fabricated array antenna (74.5 mm x 46.8 mm).

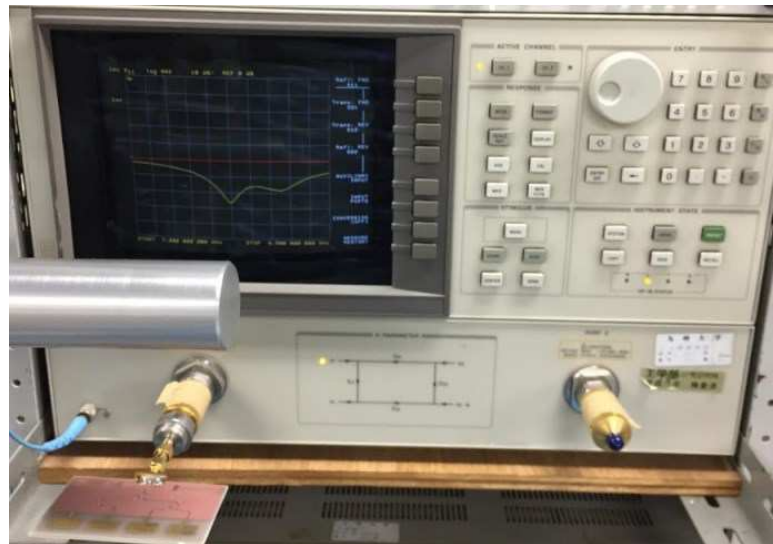


Fig. 3.14 Antenna input impedance measurement with Keysight 8722C Network analyzer.

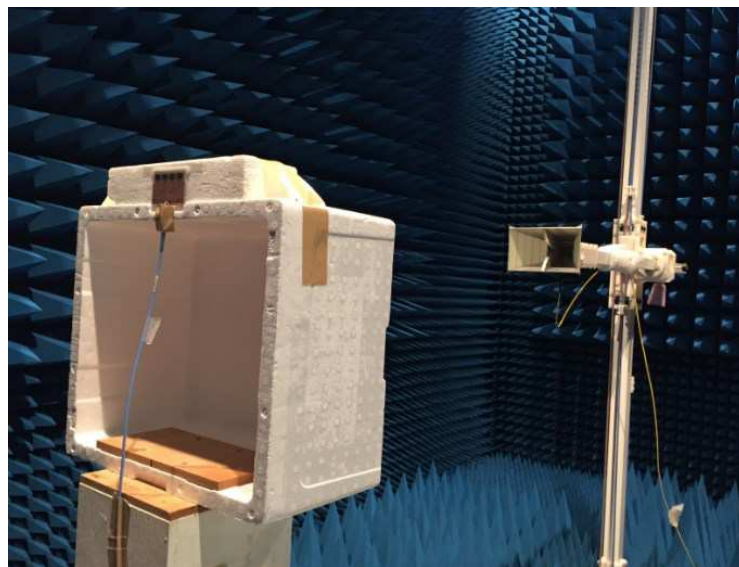


Fig. 3.15 Radiation pattern measurement setup in anechoic chamber.

Fig. 3.16 shows simulations and measurements of  $S_{11}$  and maximum realized gain of the proposed antenna from 7.4 GHz to 8.6 GHz. Measured input impedance  $S_{11}$  is lower than  $-10$  dB from 7.6 GHz to 8.4 GHz, which corresponds to 10% impedance bandwidth. As we know,  $-10$  dB impedance bandwidth depends on dielectric permittivity of substrate used. Wide  $-10$ -dB impedance bandwidth can be achieved by using dielectric material with low permittivity. As we know, dielectric material with low permittivity improves  $-10$  dB impedance bandwidth. In this work, feeding technique through permittivity coupling from 2 layers feed lines enhances  $-10$  dB impedance bandwidth. Wide  $-10$  dB impedance bandwidth in the proposed antenna is equivalent to the one in microstrip patch array antenna fabricated on low permittivity substrate ( $\epsilon_r=2.2$ ) [10]. Simulated and measured results demonstrate that a flat gain response from 7.6 to 8.4 GHz with peak gain of 5.8 dBi at 8 GHz is measured.

Fig. 3.17 shows simulated and measured normalized radiation patterns of the proposed array antenna at  $xz$ -plane and  $yz$ -plane of Fig. 3.13. Simulations and measurements are in good agreement. Array antenna propagates along  $z$ -axis with maximum side lobe level is  $-16$  dB. Measured front-to-back ratio is  $-11$  dB.

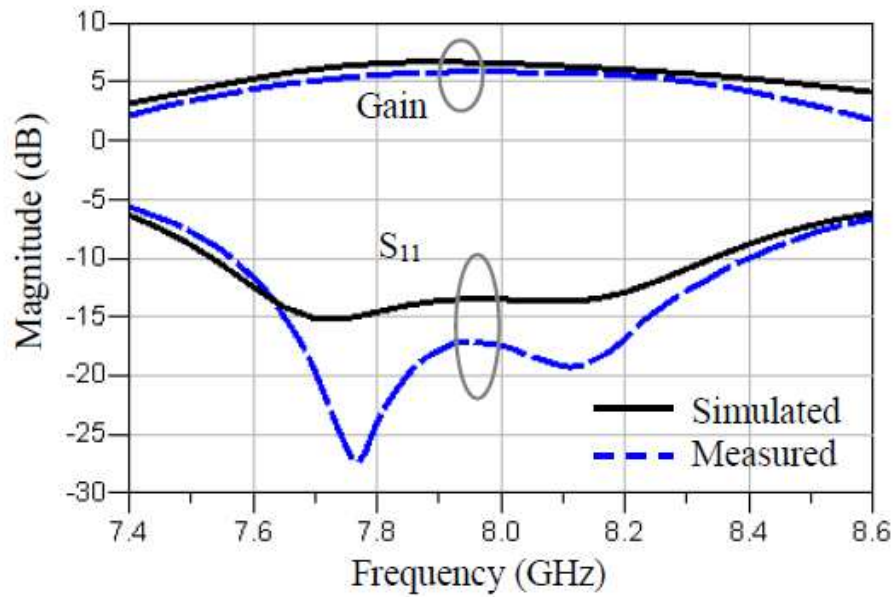


Fig. 3.16  $S_{11}$  and the maximum realized gain of the proposed array antenna. Simulations (solid) and measurements (dashed).

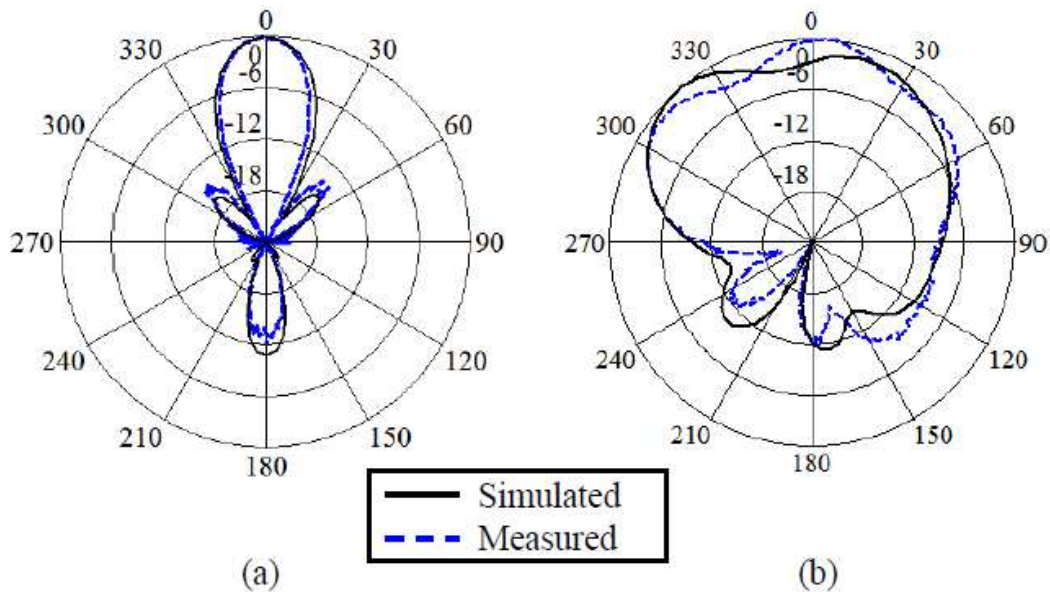


Fig. 3.17 Simulated (solid black) and measured (dashed blue) radiation patterns of the proposed array antenna at 8 GHz: (a)  $xz$ -plane, and (b)  $yz$ -plane.

### 3.4 Electromagnetic Leakage Suppression in Propagation Medium [11]

The presence of a conductor backplane in planar antenna such as microstrip patch antenna is crucial in exciting fringing field for unidirectional radiation pattern. In practice, microstrip line (MSL) has a finite ground plane that doesn't support a TEM wave to infinity transversely because the fields between the MSL and ground plane decrease exponentially as incident signals propagate away from the RF source. On the contrary, coplanar waveguide (CPW) with ground planes and conductor located on the same plane has a low fringing field in the air and dielectric substrate, thus exhibits low dispersion characteristics.

Portion of electromagnetic field from the MSL and CPW radiates to the free space, thus phase velocity changes when travelling wave penetrates through the dielectric substrate. When operating frequency exceeds critical frequency, the dominant mode changes from bound to leaky mode because the phase constant in the dielectric substrate decreases and becomes smaller than the wave number of the relevant surface wave in MSL or CPW transmission lines [12]-[14].

Author in [13] presented technique to suppress surface wave loss by stacking existing substrate of conductor backed coplanar waveguide (CBCPW) with another substrate in different permittivity to alter effective dielectric constant. Non-leaky region from the proposed technique was validated through spectral domain analysis with a complex root searching procedure [15].

Despite numerous leakage analyses at high frequencies have been reported, planar transmission line loss at low frequencies has received little attention because loss can be reduced by using costly dielectric substrate that exhibits low tangent loss. Furthermore, leakage is tolerable in single element antenna fabricated on low cost dielectric substrate, FR-4. However, dielectric loss becomes severe at frequencies above radio frequency when MSL or CPW transmission lines are fabricated on low cost dielectric substrate. Electromagnetic leakage loss increases in MSL or CPW transmission lines when feeding network are expanded to become multi-section feeding network to support antenna array systems.

In the following section, optimum separation distance between vias in the CBCPW will be derived. By using identical antenna elements, CBCPW-fed antenna arrays with and without periodic vias are compared to each other to determine leakage in the planar array antenna at S-band. Effectiveness of the proposed leakage suppression structure is validated as well.

#### 3.4.1 Minimum Distance of Periodically Spaced Vias

Geometry of periodically spaced vias illustrated in Fig. 3.18, composed of via diameter ( $d$ ), pitch between vias ( $p$ ) and distance between two rows of vias ( $w$ ), are studied to determine the region of interest where the leakage is at minimum level. Periodic vias in Fig. 3.18 act as a ground via fence and exhibit bandgap characteristics over certain frequencies range. Additional inductances and capacitances from shorting vias can be tuned to establish high impedance surface similar to bandstop resonant circuit. It suppresses leaky mode over certain frequency range in the dielectric substrate.

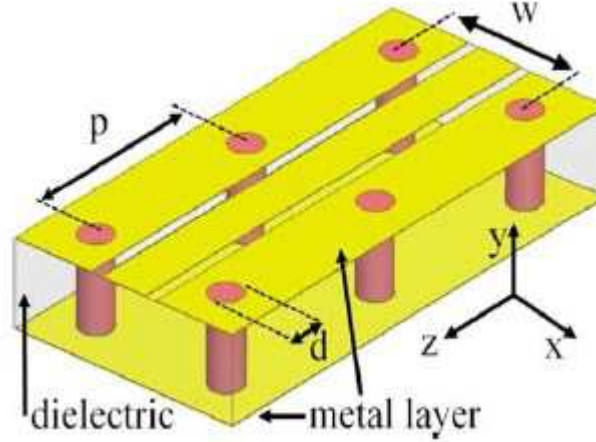


Fig. 3.18 Geometry of the CBCPW with periodically spaced vias.

For a periodic structure of period  $p_s$ , the electromagnetic field that propagates in the  $z$  axis, as depicted in Fig. 3.18, satisfies the Floquet condition [14],

$$F(z + p_s) = e^{-\gamma p_s} F(z). \quad (3.32)$$

Propagation constant  $\gamma$  in the periodic structures can be determined through Floquet modes derived from a transcend equation or classical matrix eigenvalues [16]. Once the eigenvalues of propagation constant  $\gamma$  have been determined, effective phase constant ( $\beta_{eff}$ ) can be defined as,

$$\beta_{eff} \leq \frac{n_g \pi}{p} \quad (3.33)$$

where

$$\beta_{eff} = \sqrt{k_z^2 - k_x^2}. \quad (3.34)$$

$k_z$  represents the wavenumber in the  $z$ -axis and  $k_x$  is the wavenumber in the  $x$ -axis of Fig. 3.18.  $n_g$  is the order of bandgap occurrences at  $\pi$ ;  $2\pi$ ;  $\dots$ ,  $n_g \pi$  in periodic structure. Let's assume that the first bandgaps ( $n_g=1$ ) occurs at the stopband, where the bandgap frequency is equivalent to twice of the center frequency ( $2f_0$ ) of the propagating wave.

Then, phase constant in eq. (3.34) can be expressed as,

$$\beta_{eff} = 2k_z. \quad (3.35)$$

We assume that leakage is suppressed ( $k_x \approx 0$ ) at the bandgap region. Guide wave number can be expressed as,

$$k_z = \frac{2\pi}{\lambda_g}. \quad (3.36)$$

Substituting eqs.(3.35) and (3.36) into (3.33), the maximum pitch between adjacent vias is proposed , as follows:

$$p = \frac{\lambda_g}{4} \quad (3.37)$$

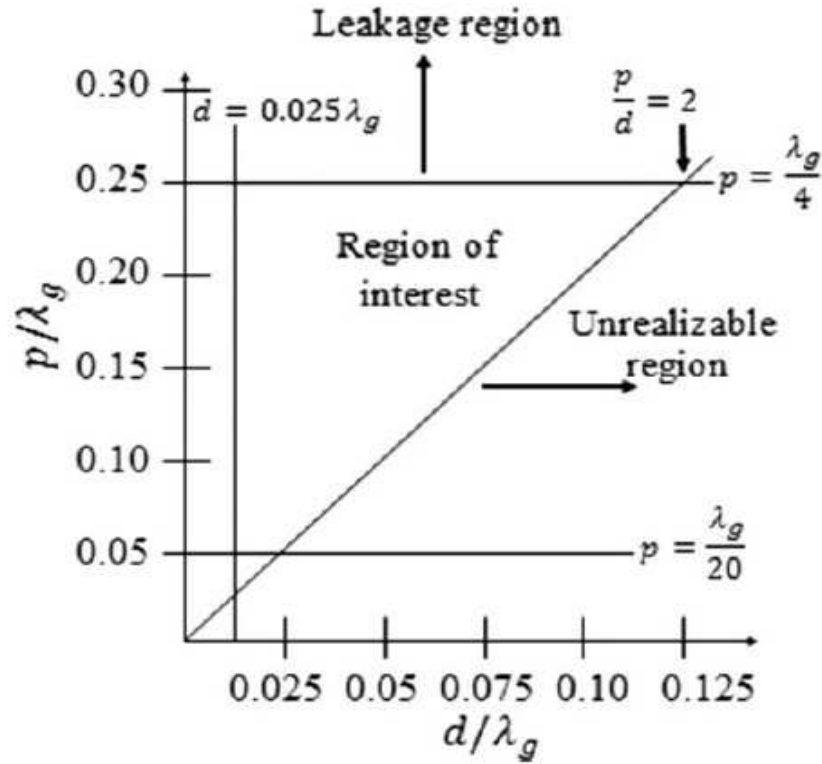


Fig. 3.19 Region of interest for the CBCPW with periodically spaced vias.



Eq. (3.38) is set to reduce number of shorting vias required in order to enhance rigidity of the printed board. Other parameters can be defined by the following equations [8]:

$$p > \frac{\lambda_g}{20}, \quad (3.38)$$

$$\frac{p}{d} = 2. \quad (3.39)$$

$\lambda_g$  is a guide wavelength of the CBCPW shown in Fig. 3.18. Minimum separation distance between vias in eq. (3.38) is crucial to prevent over-perforated structure. Eq. (3.39) is adhered to avoid adjacent vias from overlapping. It is set to follow minimum permissible via diameter restricted by the manufacturing process. In this work, via diameter is set to  $0.025\lambda_g$ . Eqs (3.37) to (3.39) are then organized in a graph to represent the region of minimum leakage loss for the conductor backed co-planar waveguide (CBCPW) filled with a ground via fence, as illustrated in Fig. 3.19.

### 3.4.2 Design Verification and Implementation

Four antenna elements are combined to form 1x4 antenna array with adjacent elements are spaced apart by one-half of the free space wavelength ( $0.5\lambda_0$ ). CPW and CBCPW configuration are used to feed identical antenna elements.

In the first topology, antenna elements are fed by the CPW corporate-fed network with air bridges attached, as illustrated in Fig. 3.20(a). Air bridges comprised of short copper wires with physical length shorter than  $0.25\lambda_g$ . The air bridges were strategically placed to join ground planes of the CPW lines [17]. The length of copper wires is kept at 8.7 mm while wire thickness is set to 0.5 mm. Air bridges are placed 5 mm apart from each other.

In the second topology, antenna elements are fed by the CBCPW with the proposed ground via fences, as shown in Fig. 3.20(b). Two rows of copper-filled vias ( $d=1.5$  mm,  $p=15$  mm), which follow design rules derived are used to connect the top conductor to the bottom conductor.

Both the CPW and CBCPW topologies are simulated using commercial 3D full wave electromagnetic simulator. Fig. 3.20 shows the geometry of array antenna with CPW-based and CBCPW-based feeding network. Realized gains of array antennas with and without the implementation of periodically spaced vias are compared to each other in order to validate the proposed design technique.

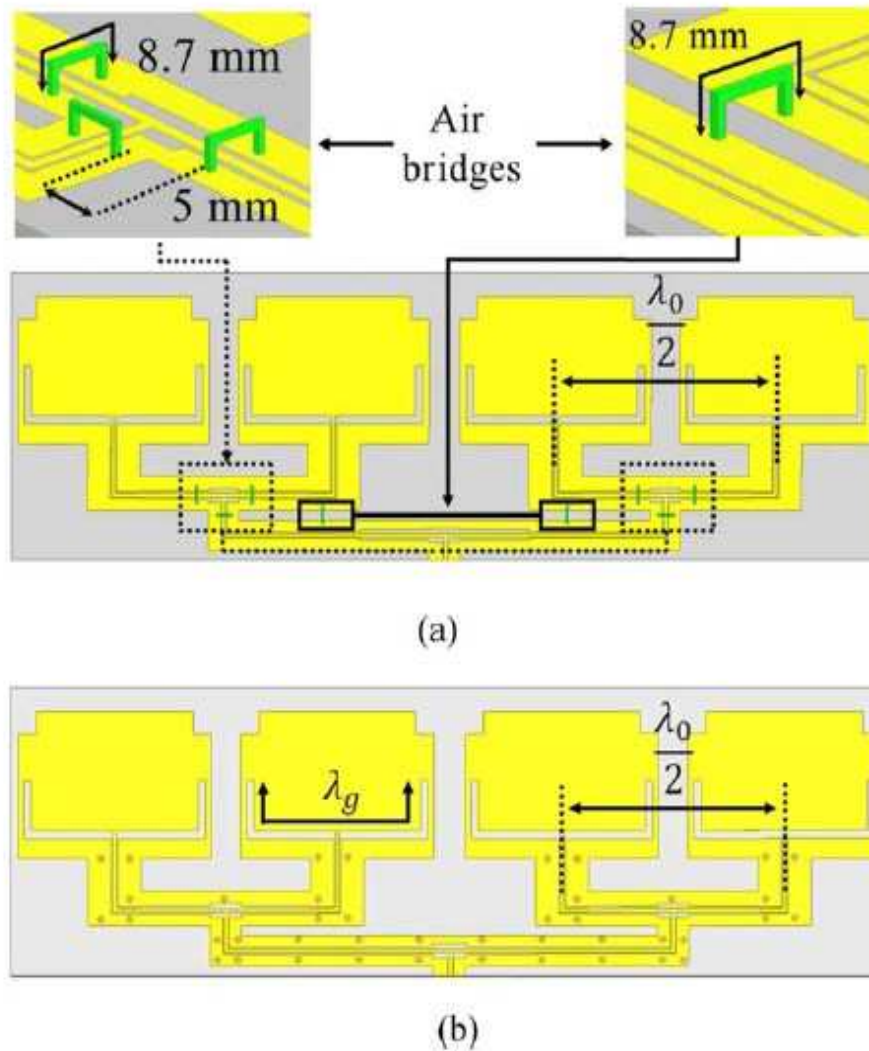


Fig. 3.20 Layouts of antenna array with different feeding topology. (a) CPW with air bridges, and (b) CBCPW with a periodic spaced-via.

### 3.4.3 Simulation and Measurement Results

To verify our analysis, CPW-fed antenna array with air bridges and CBCPW-fed antenna array (Fig. 3.21) were fabricated on a 1.6 mm FR4 ( $\epsilon_r=4.1$ ,  $\tan \delta=0.015$  at 2.4 GHz) sandwiched by the top and bottom copper layers of  $0.18 \mu\text{m}$  thickness. Return loss ( $S_{11}$ ) and gain achieved by antenna arrays were measured using vector network analyzers (HP-8722C and Anritsu 37269D), starting from 2.1 to 2.6 GHz.

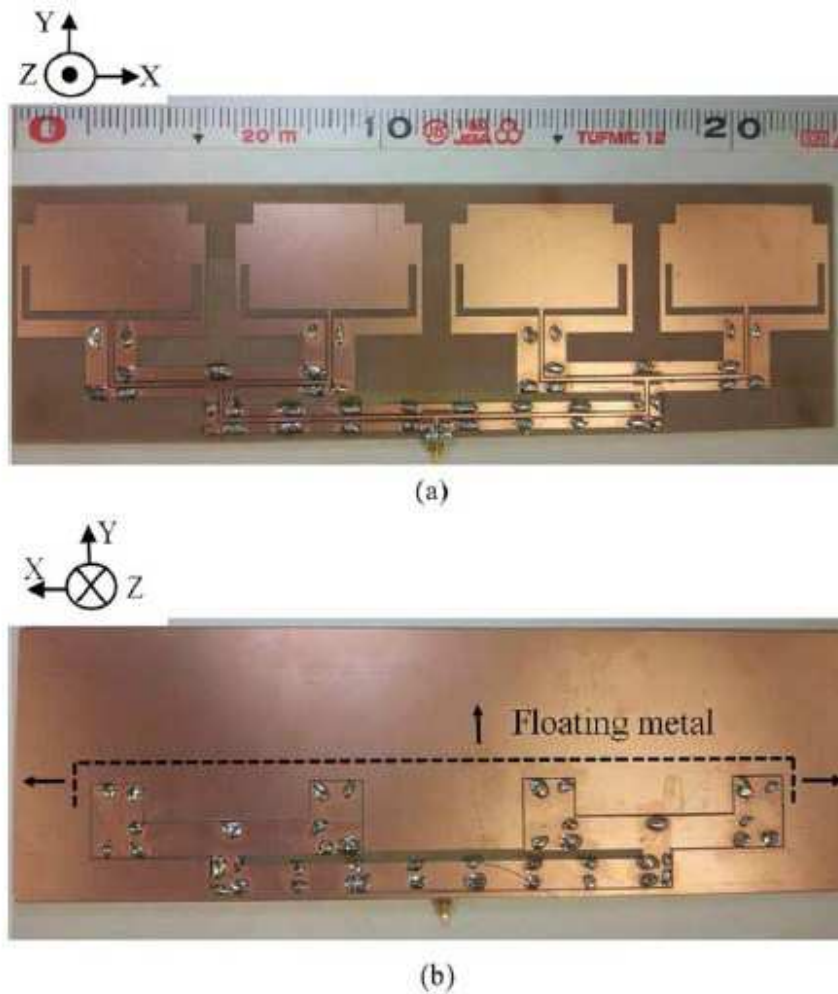


Fig. 3.21 Fabricated 4x1 antenna array with the CBCPW feeding network (size=234 mm x 71 mm). (a) Top view, and (b) bottom view.

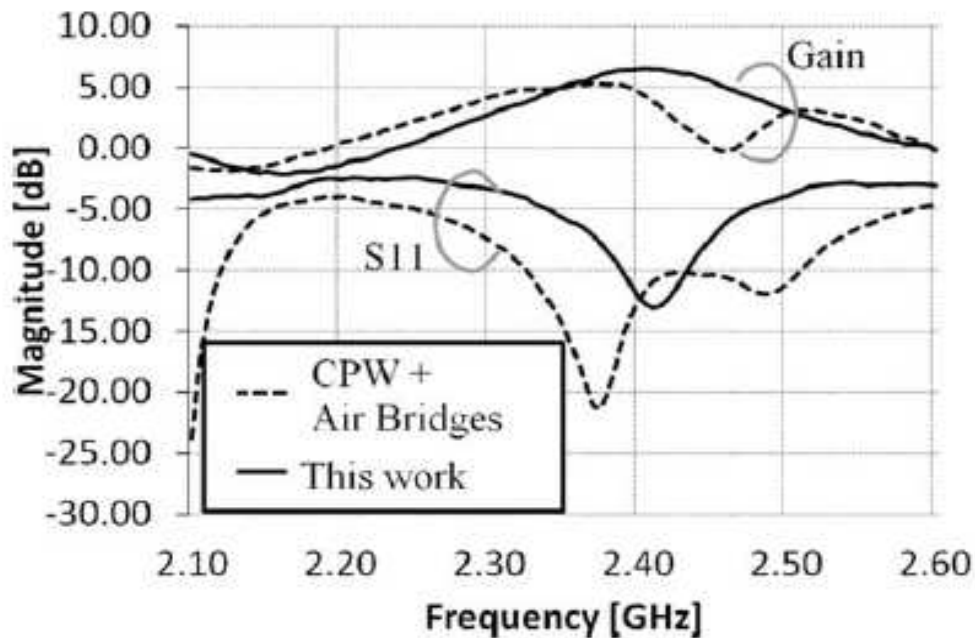


Fig. 3.22 Measured reflection coefficient ( $S_{11}$ ) and realized gain of the CPW-fed and the CBCPW-fed antenna arrays.

Fig. 3.22 displays measurement results for the  $S_{11}$  and gain achieved in the CPW and CBCPW feeding networks. 1-dB gain difference observed from the comparison of CPW-fed and CBCPW fed antenna arrays validates the effectiveness of optimum separation distance derived to suppress leakage in the dielectric substrate.

Realized gain in antenna arrays were calculated using the Friss transmission equation based on measured S parameter data ( $S_{21}$ ). Antenna array fed by the CBCPW has a peak gain of 8.5 dBi (simulated) and 6.5 dBi (measured) at 2.4 GHz. Meanwhile peak gain achieved by the CPW-fed antenna array is 7.4 dBi (simulated) at 2.42 GHz and 5.3 dBi (measured) at 2.37 GHz. With the implementation of periodically space vias, 1 dB recovered from the leakage loss in dielectric medium is crucial for large-scale array antennas such as uni-directional antenna arrays. Measured gain is 2 dB less than simulation results of CPW and CBCPW topologies is due to the residual loss between feed line and coaxial connector.

Fig. 3.23 shows the simulation and measurement of normalized radiation patterns for the CBCPW-fed antenna array. The drawback of the proposed ground via fence in antenna array is that  $-10$  dB impedance bandwidth is narrow due to the bandgap effects related to frequency-dependent wave propagation in periodically spaced vias.

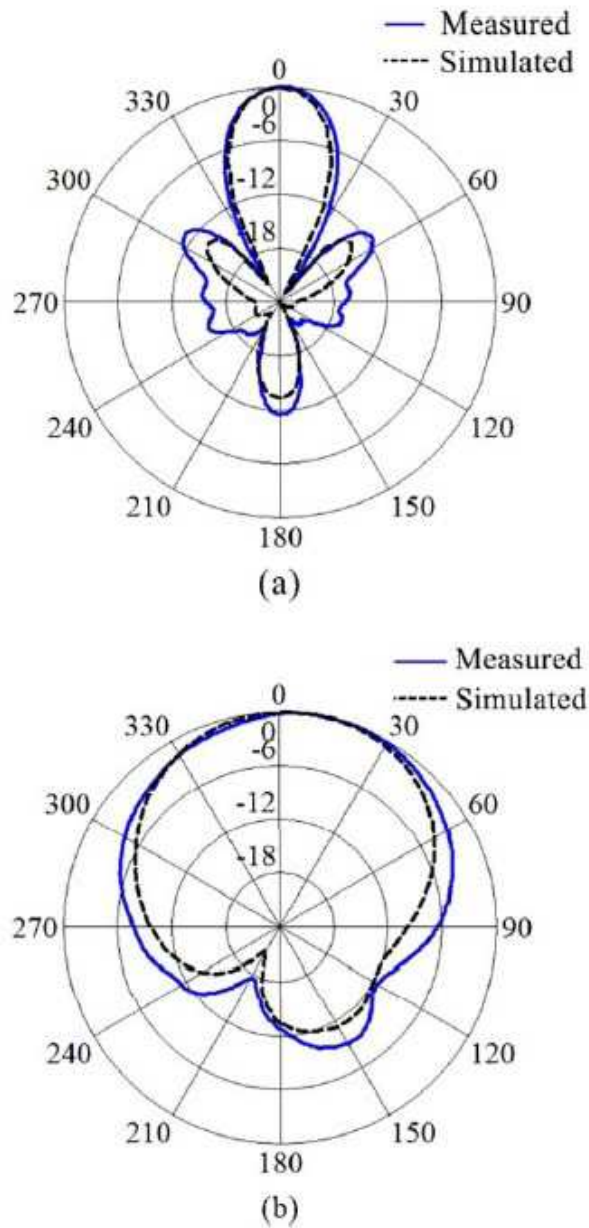


Fig. 3.23 Radiation pattern of 4x1 CBCPW-fed antenna array. (a)  $xz$ -plane, (b)  $yz$ -plane.

### 3.5 Chapter Summary

In this chapter, two-layer proximity coupled feed line has been proposed for slotted antenna in order to reduce gain degradation due to reduced substrate thickness. Two layers feed line with impedance tuning ratio of  $w_p/w_f$ , can be easily scaled to reduce impedance mismatch between antennas and feeding network of multiple layers PCB. Design and implementation of the proposed antenna were discussed, followed by measurements of fabricated antenna arrays. Next, S-parameter of Wilkinson power divider was derived using even-odd analysis. Antenna elements were fabricated on 1.6 mm FR-4 substrate. They were fed by using corporate feeding network fabricated on 0.25 mm FR-4 substrate. Experimental results demonstrate that proposed antenna is compatible with multiple layers PCB manufacturing process. Last, the structure of periodically-space vias were proposed, fabricated, and measured. The proposed periodic vias has suppressed radiation loss vias in a FR-4 dielectric substrate successfully, as demonstrated in the experiments.

## References

- [1] X. H. Yang and L. Shafai, “Characteristics of aperture coupled microstrip antennas with various radiating patches and coupling apertures,” *IEEE Trans. Antennas Propag.*, vol. 43, no. 1, pp. 72–78, Jan. 1995.
- [2] S. D. Targonski, R. B. Waterhouse, and D. M. Pozar, “Design of wide-band aperture-stacked patch microstrip antennas,” *IEEE Trans. Antennas Propag.*, vol. 46, no. 9, pp. 1245–1251, Sept. 1998.
- [3] C. E. Guan, M. Mansour, K. Yoshitomi, and H. Kanaya, “A Printed Array Antenna for Multi-layer PCB Design,” 2017 International Symposium on Antennas and Propagation (ISAP), Oct. 2017.
- [4] D. H. Schaubert, D. M. Pozar, and A. Adrian, “Effect of microstrip antenna substrate thickness and permittivity: Comparison of theories and experiment,” *IEEE Trans. Antennas Propag.*, vol. 37, no. 6, pp. 677–682, June 1989.
- [5] H. Kanaya, S. Tsukamoto, T. Hirabaru, D. Kanemoto, R. K. Pokharel, K. Yoshida, “Energy Harvesting Circuit on a One-Sided Directional Flexible Antenna,” *IEEE Microw. Wireless Compon. Lett.*, vol. 23, no. 3, pp. 164–166, March 2013.
- [6] N. K. Uzunoglu, N. G. Alexopoulos, and J. G. Fikioris, “Radiation Properties of Microstrip Dipoles,” *IEEE Trans. Antennas Propag.*, vol. 27, no. 6, pp. 853–858, Nov. 1979.
- [7] A. Hamo, A. Benyamini, I. Shapir, I. Khivrich, J. Waissman, K. Kaasbjerg, Y. Oreg, F. von Oppen & S. Ilani, “Electron attraction mediated by Coulomb repulsion,” *Nature*, vol. 535, pp. 395–400, July 2016.
- [8] Warren L. Stutzman and Gary A. Thiele, “Antenna Theory and Design,” 3rd Edition, John Wiley & Sons Inc., May 2012.

- [9] J. Reed and G. J. Wheeler, "A Method of Analysis of Symmetrical Four-Port Networks," IRE Trans. on Microw. Theory and Techn., vol. MTT-4, pp. 246–252, Oct. 1956.
- [10] S. H. Yeung, A. García-Lampérez, T. K. Sarkar, and M. Salazar-Palma, "Comparison of the Performance Between a Parasitically Coupled and a Direct Coupled Feed for a Microstrip Antenna Array," IEEE Trans. Antennas Propag., vol. 62, no. 5, pp. 2813-2818, May 2014.
- [11] C. E. Guan, K. Yoshitomi, and H. Kanaya, "Derivation of The Optimum Distance Between Periodically Spaced Via for Leakage Suppression at S-band," Microwave and Optical Technology Letters, Vol. 58, no. 5, pp. 1257-1260, May 2016.
- [12] A. A. Oliner and K. S. Lee, "The nature of the leakage from higher modes on microstrip line," IEEE MTT-S Int Microwave Symp Digest, Baltimore, Maryland, pp. 57–60, June 1986.
- [13] L. Yaozhong, C. Kimin, and T. Itoh, "Non-leaky coplanar (NLC) waveguides with conductor backing," IEEE Trans. Microw. Theory and Tech., vol. 43, no. 5, pp. 1067–1072, May 1995.
- [14] N. K. Das, "Methods of suppression or avoidance of parallel-plate power leakage from conductor-backed transmission lines," IEEE Trans Microw. Theory and Tech., vol. 44, no. 2, pp.169–181, Feb. 1996.
- [15] R.E. Collin, "Field theory of guided waves," 2<sup>nd</sup> edition, Wiley-IEEE Press, Dec. 1990.
- [16] S. Amari, R. Vahldieck, J. Bornemann, and P. Leuchtmann, "Spectrum of corrugated and periodically loaded waveguides from classical matrix eigenvalues," IEEE Trans. Microw. Theory and Tech., vol. 48, no. 3, pp. 453–460, March 2000.
- [17] G. E. Ponchak, J. Papapolymerou, and M. M. Tentzeris, "Excitation of coupled slotline mode in finite-ground CPW with unequal ground-plane widths," IEEE Trans. Microw. Theory Tech., vol. 53, no. 2, pp.713–717, Feb. 2005.



## Chapter 4

### Phase Shifter

One of the core components of phased array antenna is the phase shifter. It produces a change in the phase of signals transmitted through it. In phased array antenna, each antenna element is connected to a single phase shifter. Beam is steered when progressive phase shift is applied to adjacent antenna elements in the array. Critical parameters in phase shifter such as phase shift range, insertion loss and insertion loss variation across phase shift range determine the performance of the phased array antenna. Phase shifter can be realized by tuning the frequency of RF signal electronically by adjusting parameters discussed in Section 2.2. Architecture of electronically controlled phase shifter can be categorized into digital circuit and analog circuit.

Most of the digital phase shifters use vector sum method for adjusting phase shift. In vector sum method,  $-3\text{dB}$  quadrature hybrid coupler is used to split incident signal into two components of equal amplitude but  $90^\circ$  difference in phase, better known as in-phase signal  $I$  and quadrature phase signal  $Q$ . Each signal passed through separate bi-phase modulator. Phase is changed discretely, e.g. from  $0^\circ$  to  $45^\circ$ ,  $90^\circ$  or  $180^\circ$  state, for both  $I$  and  $Q$  components. Relationship between  $I$  and  $Q$  in Fig. 4.1(b) is given as

$$|I|^2 + |Q|^2 = 1 \quad (4.1)$$

$$I = 20 \log(R \cos \theta) \quad (4.2)$$

$$Q = 20 \log(R \sin \theta) \quad (4.3)$$

$R = 10^{-(x/20)}$  and  $x$  is an attenuation level in dB.

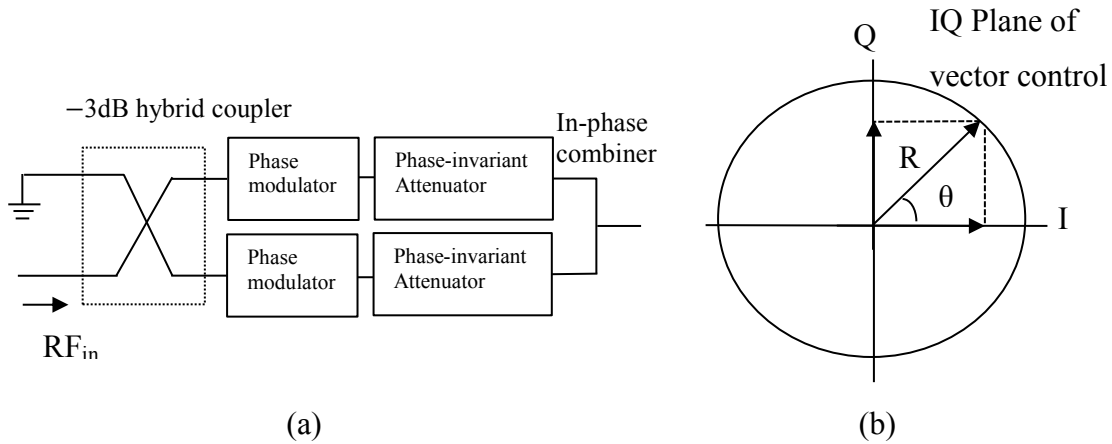


Fig. 4.1 Digital phase shifter. (a) Circuit block diagram, and (b) I-Q relationship.

IQ plane is a square, rather than a circle, because I and Q components are not equal in amplitude at the output of bi-phase modulator. Discrete phase shifts are represented by a various states. Circuit designer has to determine the maximum insertion loss occurs at one of these states. Once the maximum insertion loss is determined, the I or Q amplitudes in the other states are adjusted using phase invariant attenuator in each path to match to the state with maximum insertion loss to form unit circle (See Fig. 4.1 (b)).

On the other hand, analog phase shifter is preferred in phased array antenna and phase modulation in communication systems because it offers adjustable continuous phase shift. Relative phase shift of a two ports network can be realized through different phase shift techniques such as ferroelectric materials, loaded lines or reflection loads. The utilization of varactor diode as reflective load in the phase shifter dates back to the early 1960s [1]. Back then, reflective-type phase shifter (RTPS) was constructed using 3 ports circulator and a reflective load. As microstrip technology proliferated, 3 ports circulator had been replaced by the hybrid coupler due to its compact size, high-power handling and ease of implementation. Over past few decades, most of the researchers focused on maximizing the phase shift range. Phase shift range could be improved by increasing varactor diode's capacitance range, combining two  $180^\circ$  phase shifters, or cascading two shunt varactor diodes separated by quarter wavelength of the guide wavelength to achieve a full  $360^\circ$  phase shift range, as described in [2]–[5].

Area of the hybrid coupler phase shifter is primarily occupied by the hybrid coupler because of its quarter wavelength branches. Various miniaturization techniques, in either MMIC process [6] or low cost printed circuit board (PCB) process, have been proposed as cost-saving measures. Authors in [7] proposed T-section transmission line consists of different line lengths and characteristic impedances to replace quarter wavelength transmission line of the conventional  $-3$ -dB hybrid coupler. But, the reduced-size coupler with unequal branch length has a narrow impedance bandwidth. In [7]–[10] and [12], the authors presented various combinations of a short, high-impedance transmission line as inductor element and shunt open-end stubs to offset capacitance loss caused by the reduced line of the miniaturized coupler. Reduced-size hybrid coupler phase shifter was implemented using existing miniaturization technique and deployed in the phased array antenna [10]. Due to the narrow phase shift range, the authors had to opt for series-fed network in order to obtain larger accumulated phase delay to steer array antenna.

For area reduction purpose, reduced-size hybrid couplers with interdigitated distributed-element capacitor had been developed to suppress second harmonic noise [11], [12]. It can be deployed at transmit and receive paths of the phase modulation communication system to prevent out-of-band signals from saturating the front end. Previous researches show that size reduction of the hybrid coupler has little impact on its coupling performance. However, the phase shift range might be reduced due to the device miniaturization. Lack of researches on the implementation of the miniaturized coupler in the phase shifter to obtain maximum phase shift is the motivation of the work described here.

For the first section, we analyze and design a full  $360^\circ$ , harmonic-suppressed phase shifter without compromising on its phase shift range. Distributed elements  $\pi$ -section low pass filter (LPF) is considered as a replacement for quarter wavelength branches of the hybrid coupler phase shifter. Proposed phase shifter is the reflective type phase shifter, which is capable to suppress second harmonic noise. However, it is not suitable for phased array antenna.

When phase shifter is cascaded to the antenna element of phased array antenna, the device radiates and causes destructive interference to the radiation pattern. Fig. 4.2 shows the radiation pattern of phased array antenna and near to zero point, better known as null in antenna terminology. Null is observed due to the destructive interference caused by phase shifter. Improvement is then made in the phase shifter and discrete components are proposed as reflection loads to overcome unwanted radiation from phase shifter. Proposed idea of the deployment of discrete components not only reduces the area of the existing phase shifter, but it also reduces insertion loss variation with respect to the changes of relative phase shift.

#### 4.1 360° Phase Shifter with Harmonic Suppression [13]

##### 4.1.1 Numerical Analysis

###### A. Distributed Elements Low Pass Filter

Fig. 4.3 shows the configuration of the  $\pi$ -section low pass filter (LPF) consists of a series inductor and two shunt capacitors. Series high impedance and shunt low impedance paths attenuate high frequency elements. At microwave band and above, distributed elements filter is preferred because of its relatively small size and low insertion loss. An ultra-compact coplanar waveguide (CPW) bandpass filter with sharp roll-off attributed to the higher order filters ( $n = 11$ ) had been reported in [14].

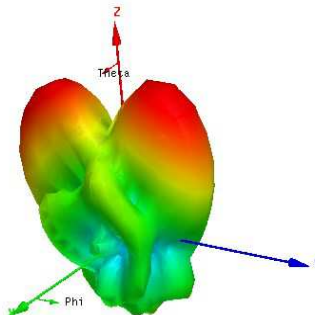


Fig. 4.2 Null in phased array antenna due to destructive interference between phase shifter and antenna elements.

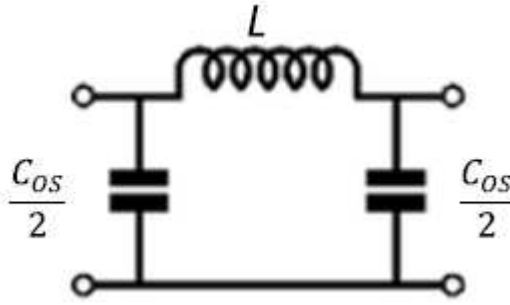


Fig. 4.3 Schematic diagram of  $\pi$ -section low pass filter (LPF).

Since phase shifter discussed here is designed to operate at 8.6 GHz, distributed elements is chosen because short propagating wavelength allows the distributed elements  $\pi$ -section LPFs to be integrated in the phase shifter for fabrication using the standard patterned circuit board process. Components in the  $\pi$ -section LPF are modelled on shunt open-end stubs to represent capacitive components and series transmission line to represent inductive component. Richards' transformation is used to find the equivalent capacitance of the open-end stub. By mapping the frequency variable  $\omega$  to the  $\Omega$ -plane, the susceptance of the open-end stub with capacitance is derived, as follows:

$$jB = j\Omega \left( \frac{\cos \theta}{2} \right) \quad (4.4)$$

$$\Omega = \tan \beta l. \quad (4.5)$$

$\beta$  is the propagation constant in the transmission medium. Open-end stub is designed by taking advantage of wave characteristic of which its length is inversely proportional to the operating frequency. At the center frequency  $f_c$ , open end stub's electrical length  $\theta_l$  is set to one-eighth of a guide wavelength ( $\lambda_g/8$ ). At the second harmonic, it becomes quarter wavelength ( $\lambda_g/4$ ) to create transmission zeros. If the open-end stub's electrical length is equal to or less than one-eighth of a guide wavelength, Taylor series approximation for eq. (4.5) is  $\Omega = \beta l$ . By assigning arbitrary width to the open-end stub, susceptance  $B$  can be determined from the approximation formula found in [15]. Susceptance of an open end stub can be calculated by substituting  $\cos \theta$  and  $\Omega$  into eq. (4.4).

Cutoff frequency of the  $\pi$ -section LPF can be obtained from,

$$f_{cutoff} = \frac{1}{\pi\sqrt{LC_{os}}} . \quad (4.6)$$

$\pi$ -section LPF is proposed to replace quarter wavelength transmission line of the hybrid coupler. Therefore, dimensions of the inductive transmission line must be optimized to keep phase shift range constant.

### B. Hybrid Coupler in Phase Shifter

Quadrature hybrid coupler in the phase shifter functions as power divider to deliver traveling waves to ports R1 and R2, and as power combiner at the output port of the RTPS (Figs. 4.4 and 4.5). Reflected signals from ports R1 and R2 that are terminated to ground using voltage-controlled varactor, undergo phase changes when the bias voltage applied across the varactor is varied. Reflected signals with shifted phase are then combined at the output port of the phase shifter. Distributed elements  $\pi$ -section LPF is used to replace quarter wavelength transmission line of the hybrid coupler, without increasing the size of the phase shifter. This can be achieved by assigning the length of the open-end stub to one-eighth wavelength ( $\lambda_g/8$ ) at the center frequency  $f_c$  so that it can be fitted into the blank space in the coupler. At the second harmonic, the effective electrical length of the open stub becomes  $\lambda_g/4$  to produce transmission zeros. For maximum power transfer, two distributed elements  $\pi$ -section LPFs are deployed in the phase shifter to ensure reflected signals that arrive at the RF output port are in phase. Most importantly, the port impedance ratio of the conventional and proposed phase shifters must be equal to each other in order to maintain consistent phase shift range. Hence, eq. (4.7) is established, given as

$$r_z = \frac{Z_{i1}}{Z_{o1}} = \frac{Z_{i2}}{Z_{o2}} . \quad (4.7)$$

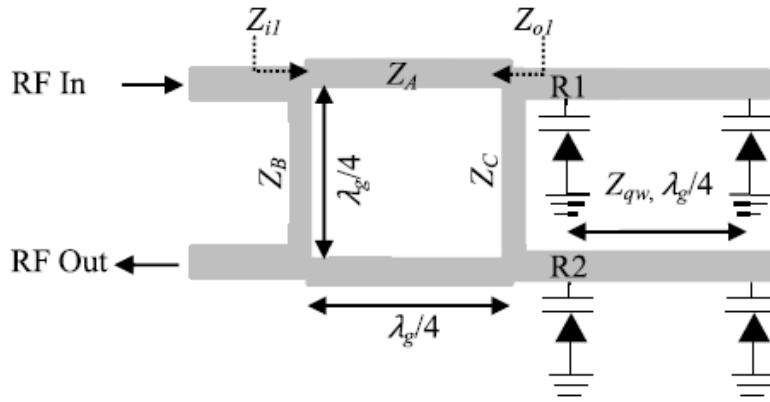


Fig. 4.4 Schematic of the conventional RTPS.

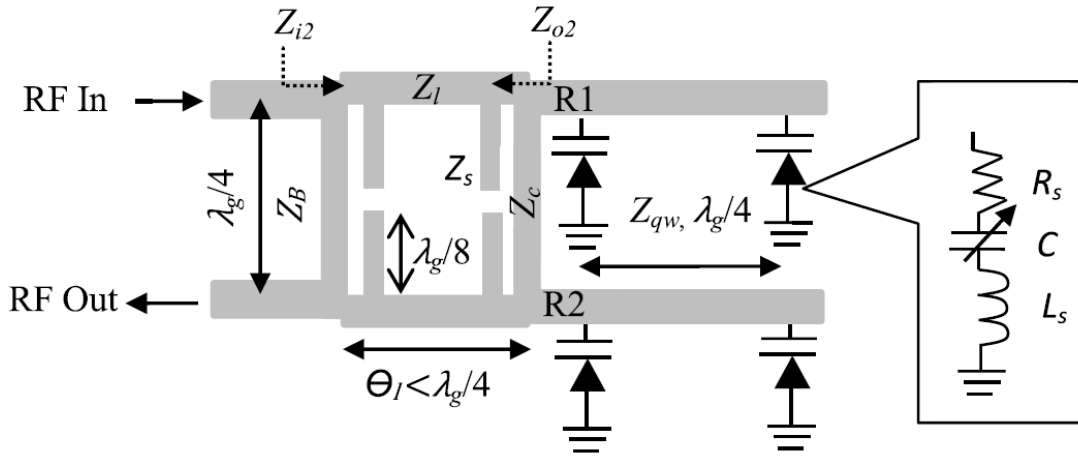


Fig. 4.5 Schematic of proposed phase shifter with harmonic suppression.

With pre-specified values of  $Z_{il}$ ,  $Z_{i2}$ ,  $Z_{o1}$ ,  $Z_{o2}$  and the hybrid coupler's coupling coefficient  $k$ , characteristic impedance of each branch in the coupler in Fig. 4.4 can be calculated from [16], given as

$$Z_A = \sqrt{\frac{Z_{im}Z_{om}}{1+k^2}} \quad Z_B = \frac{Z_{im}}{k} \quad Z_C = \frac{Z_B Z_{om}}{Z_{im}} \quad \text{for } m = 1, 2. \quad (4.8)$$

As depicted in Figs. 4.4 and 4.5, the reflection coefficient at port R1 terminated with two shunt varactors separated by a quarter wavelength transmission line can be written as

$$|\Gamma| = \frac{Z_{load} - Z_{o2}}{Z_{load} + Z_{o2}} = \frac{R_s Z_{qw}^2 + Z_{o2}(X_{vac}^2 - R_s^2) + jX_{vac}(Z_{qw}^2 - 2Z_{o2}R_s)}{R_s Z_{qw}^2 - Z_{o2}(X_{vac}^2 - R_s^2) + jX_{vac}(Z_{qw}^2 + 2Z_{o2}R_s)}. \quad (4.9)$$

$Z_{qw}$  is the characteristic impedance of the quarter wavelength transmission line.  $R_s$  and  $L_s$  are parasitic components of the varactor depicted in the inset of Fig. 4.5. For the sake of simplicity,  $L_s$  is accounted into reactance components  $X_{vac}$  of the varactor. Maximum phase shift range is realized by terminating ports R1 and R2 of the phase shifter with identical reflection loads. Relative phase shift ( $\phi_{S21}$ ) is the phase angle of the reflection coefficient in eq. (4.9). We can compute  $\phi_{S21}$  as,

$$\phi_{S21} = 2 \tan^{-1} \left[ \frac{X_{vac}(Z_{qw}^2 - 2Z_{o2}R_s)}{R_s Z_{qw}^2 + Z_{o2}(X_{vac}^2 - R_s^2)} \right] - 2 \tan^{-1} \left[ \frac{X_{vac}(Z_{qw}^2 + 2Z_{o2}R_s)}{R_s Z_{qw}^2 - Z_{o2}(X_{vac}^2 - R_s^2)} \right] \quad (4.10)$$

$$\Delta\phi = \Delta\phi_{S21}(C_{max}) - \Delta\phi_{S21}(C_{min}) \quad (4.11)$$

Phase shift range ( $\Delta\phi$ ) greatly depends on the reactance variation  $\Delta X_{vac}$  ( $r_c = C_{max}/C_{min}$ ) of the varactor. However, maximum phase shift of the hybrid coupler phase shifter can be increased further by doubling port impedance ratio ( $r_z = Z_{i2}/Z_{o2}$ ). At constant capacitance ratio, the maximum phase shift range in respect of the variation of the port impedance ratio  $r_z$  is calculated from (4.10) and (4.11), and plotted in Fig. 4.6. The maximal relative phase shift of the phase shifter significantly increases from  $195^\circ$  to  $360^\circ$  when  $r_z$  is changed from 1 to 2.2.

### C. Transmission Line Model Analysis

Phase shifter with harmonic suppression is realized by substituting quarter wavelength transmission line of the hybrid coupler with distributed elements  $\pi$ -section LPF. Integration of the  $\pi$ -section LPF in the hybrid coupler will not deteriorate its coupling performance. However, phase shift range might be reduced if the port impedance ratio  $r_z$  is not taken into consideration, as demonstrated in Fig. 4.6. To ensure  $r_z$  is consistent, the distributed elements  $\pi$ -section LPF can be transformed from quarter wavelength transmission line by applying ABCD matrix to the circuits in Fig. 4.7.



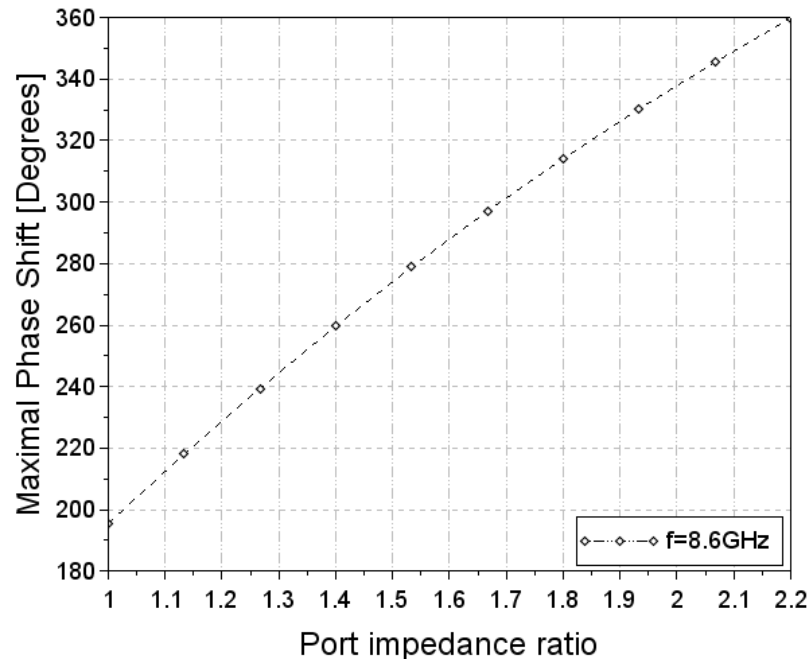


Fig. 4.6 Calculated relative phase shift versus port impedance ratio  $r_z$ . ( $Z_{qw}=20\ \Omega$ ,  $L_s=0.45\ \text{nH}$ ,  $C_{min}=0.45\ \text{pF}$ ,  $C_{max}=3.1\ \text{pF}$  and  $R_s=2.5\ \Omega$ ).

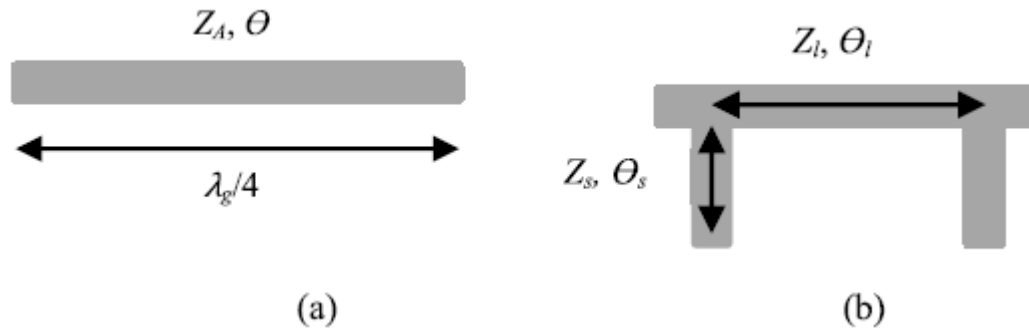


Fig. 4.7 Transmission line of the hybrid coupler. (a) Quarter wavelength transmission line, and (b) distributed elements  $\pi$ -section filter.

The conventional hybrid coupler shown in Fig. 4.7(a) has ABCD matrix that can be expressed as

$$\begin{bmatrix} \cos \theta & jZ_A \sin \theta \\ j\frac{\sin \theta}{Z_A} & \cos \theta \end{bmatrix}. \quad (4.12)$$

Meanwhile, ABCD matrix of the distributed elements  $\pi$ -section LPF shown in Fig. 4.7(b), consists of 3 matrices, is represented by eq. (4.13), as follows:

$$\begin{bmatrix} 1 & 0 \\ j\frac{\tan \theta_s}{Z_s} & 1 \end{bmatrix} \begin{bmatrix} \cos \theta_l & jZ_l \sin \theta_l \\ j\frac{\sin \theta_l}{Z_l} & \cos \theta_l \end{bmatrix} \begin{bmatrix} 1 & 0 \\ j\frac{\tan \theta_s}{Z_s} & 1 \end{bmatrix}. \quad (4.13)$$

The first and third matrices are open-end stubs evaluated at center frequency,  $f_c$  of the phase shifter. Second matrix represents inductive transmission line that connects the stubs. To suppress the second harmonic,  $45^\circ$  or one-eighth of guide wavelength at the center frequency  $f_c$  of the phase shifter is assigned to  $\theta_s$ . ABCD coefficients of the distributed elements  $\pi$ -section LPF calculated from the matrix product of eq. (4.13) is given in eq. (4.14), as follows:

$$\begin{bmatrix} \cos \theta_l - \frac{Z_l}{Z_s} \sin \theta_l \tan \theta_s & jZ_l \sin \theta_l \\ j\frac{\cos \theta_l}{Z_l Z_s^2} (Z_s^2 \tan \theta_l + \tan \theta_s (2Z_l Z_s - yZ_l^2)) & \cos \theta_l - \frac{Z_l}{Z_s} \sin \theta_l \tan \theta_s \end{bmatrix} \quad (4.14)$$

with  $y = \tan \theta_l \tan \theta_s$ . Port impedance ratio  $r_z$  is kept consistent by equating the ABCD matrices of the  $\pi$ -section LPF to the conventional quarter wavelength transmission line. From eq. (4.12) and eq. (4.14), the following relations are established,

$$Z_l \sin \theta_l = Z_A \sin \theta, \quad (4.15)$$

$$Z_l \sin \theta_l = Z_s (\cos \theta_l - \cos \theta) / \tan \theta_s. \quad (4.16)$$

Note that we assume  $0 < \theta_l \leq \theta$  in our discussion to ensure eq. (4.16) is always positive for the  $\pi$ -section LPF.  $Z_A$  and  $\theta$  are known variables since the conventional hybrid coupler has four quarter wavelength transmission lines.

The characteristic impedance of the hybrid coupler ( $Z_A$ ,  $Z_B$ , and  $Z_c$ ) can be calculated from eq. (4.8) using user-defined coupling coefficient of the coupler. Substituting eq. (4.15) into (4.16), characteristic impedance of the open-end stub can be expressed as

$$Z_s = \frac{Z_A \sin \theta \tan \theta_s}{(\cos \theta_l - \cos \theta)}. \quad (4.17)$$

Eq. (4.17) implies that the  $\pi$ -section LPF is equivalent to the conventional quarter wavelength transmission line in Fig. 4.7(a) when proper values are assigned to  $Z_s$  and  $\theta_l$ . Dielectric substrate's thickness and effective dielectric constant of  $t$  and  $\epsilon_{eff}$ , and the stub's width,  $w_s$  are determined beforehand. Characteristic impedance of the open-end stub,  $Z_s$  in microstrip mode is then computed using the curve-fit approximation formula found in [14], as follows:

$$\begin{aligned} Z_s &= \frac{60}{\sqrt{\epsilon_{eff}}} \ln \left( \frac{8t}{W_s} + \frac{W_s}{4t} \right) \quad \text{for } \frac{W_s}{t} \leq 1 \\ &= \frac{120\pi}{\sqrt{\epsilon_{eff}} \left[ \frac{W_s}{t} + 1.393 + 0.667 \ln \left( \frac{W_s}{t} + 1.444 \right) \right]} \quad \text{for } \frac{W_s}{t} \geq 1 \end{aligned} \quad (4.18)$$

The required electrical length  $\theta_l$  of the inductive transmission line is obtained by substituting  $Z_s$  obtained from eq. (4.18) to eq. (4.17). Remaining unknown parameter  $Z_l$  can now be computed by solving eq. (4.15) using calculated parameters of  $Z_A$ ,  $\theta$ ,  $Z_s$ ,  $\theta_s$ , and  $\theta_l$ .

#### 4.1.2 Parametric Analysis

In the previous analysis, transmission line is analyzed instead of the hybrid coupler to avoid rigorous design equations corresponding to the even- and odd-mode half structures analysis. In order to validate numeric method introduced in Section 4.1.1, the hybrid coupler is now analyzed using parametric analysis to find unknown design parameters ( $Z_l$ ,  $\theta_l$ ) of the  $\pi$ -section LPF. Parameters found are compared with results obtained from the transmission line model analysis for validation purpose.

Assume that the conventional RTPS of Fig. 4.4 has port impedance ratio  $r_z = 1$ . The port impedance ratio of the proposed phase shifter with integrated  $\pi$ -section LPFs in Fig. 4.5 should be equal to  $r_z = 1$  to achieve consistent phase shift range. Theoretical prediction in Fig. 4.5 was plotted based on the capacitance values given in the datasheet of the commercial varactor diode. Because of the limitation in the capacitance range, the phase shifter is designed with a port impedance ratio  $r_z = 2$  for full  $360^\circ$  phase shift. To obtain  $r_z = 2$ , characteristic impedances of the vertical branches in the  $-3$ -dB hybrid coupler depicted in Figs. 4.4 and 4.5, can be calculated from eq. (4.8) as  $Z_B = 50 \Omega$  and  $Z_C = 25 \Omega$  when  $Z_{i1} = 50 \Omega$ ,  $Z_{i2} = 50 \Omega$ . Close approximation of the width of the short transmission line of  $\theta_l$  in Figs. 4.5 and 4.7(b) can be determined since its impedance  $Z_l$  should be equivalent to the characteristic impedance ( $Z_A = 25 \Omega$ ) of the quarter wavelength transmission line in Fig. 4.4.

Parametric variation on electric length  $\theta_l$  of the inductive transmission line of the  $\pi$ -section LPF was performed using Keysight Technologies' Advanced Design System™ (ADS). Fig. 4.8 shows the characteristic impedances  $Z_{i2}$  and  $Z_{o2}$  of the proposed phase shifter with respect to the  $\theta_l$  variation (8 to 9 GHz). In Fig. 4.8, characteristic impedances of the proposed structure (Fig. 4.5) and conventional RTPS (Fig. 4.4) are not equal but full  $360^\circ$  phase shift is predicted in the proposed phase shifter based on the theoretical calculation in Fig. 4.6 when  $r_z = 2$ . With predefined parameters  $Z_s = 67.7 \Omega$  and  $\theta_s = 45^\circ$  of the open-end stub, the optimum values of the series transmission line are  $Z_l = 26.28 \Omega$  and  $\theta_l = 72^\circ$  at 8.6 GHz.

#### 4.1.3 Relationship of Series Inductance and Phase Shift Range

To our knowledge, maximum phase shift range in the RTPS primarily depends on the varactor capacitance ratio  $r_c$  and port impedance ratio  $r_z$  of the hybrid coupler phase shifter. Transmission line model and parametric analysis are proposed to ensure the phase shift range is not affected by the integration of  $\pi$ -section LPF. In addition, we would like to highlight on another parameter that influences the phase shift range of the phase shifter. As the phase shifter discussed here operates at high frequency (8.6 GHz), series inductance and capacitance values of the reflective load should be deliberately selected to produce decent reactance level for full  $360^\circ$  relative phase shift.

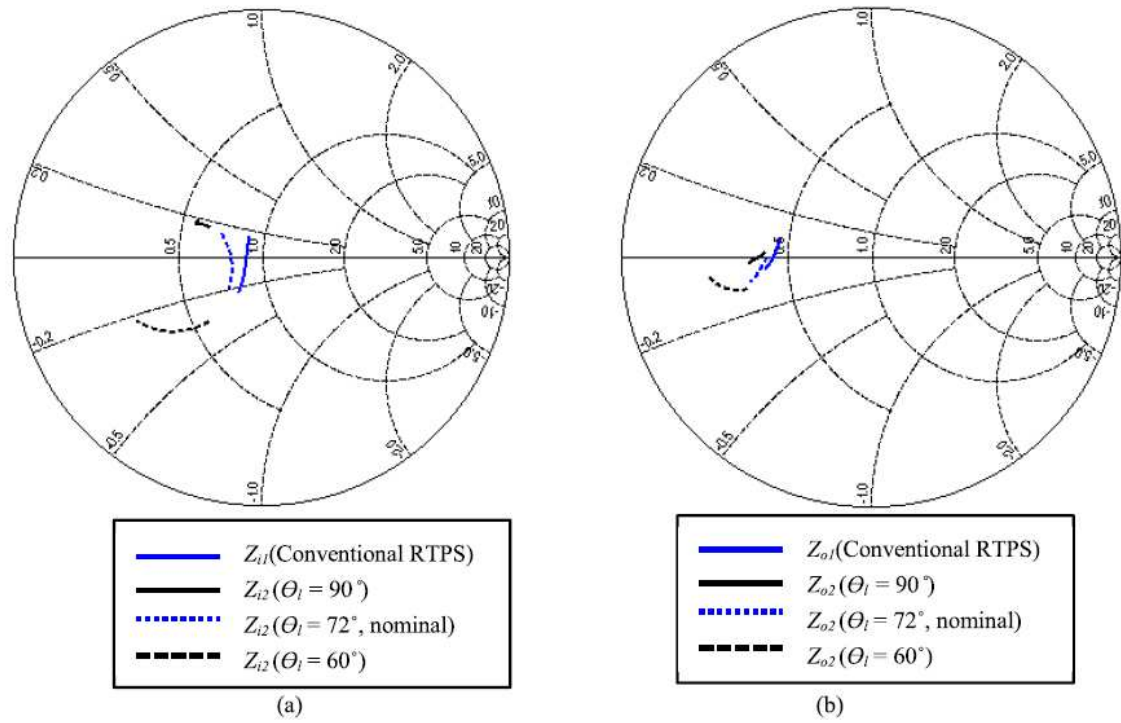


Fig. 4.8 Parametric variation of the electrical length  $\theta_l$  of the transmission line to obtain  $r_z=2$  (a)  $Z_{i2}$  versus  $\theta_l$  variation, and (b)  $Z_{o2}$  versus  $\theta_l$  variation.

Correspondingly, varactor with small capacitance (in the range of few Pico farads) and small inductance is often selected as reflective load when the center frequency of the RTPS is in the range of X-band and above. Since our phase shifter is designed to operate at 8.6GHz, design equations are derived to find the optimum series inductance required in order to obtain the maximum phase shift range.

As illustrated in the inset of Fig. 4.5, maximum phase shift range is calculated from the phase difference between the extreme varactor capacitance values at  $C_{min}$  and  $C_{max}$ . By taking parasitic inductance  $L_s$  into account, eq. (4.11) can be rewritten, as follows:

$$\Delta\phi_{max} = |\angle S_{21}(X_{vac,Cmax}) - \angle S_{21}(X_{vac,Cmin})| \quad (4.19)$$

where

$$X_{vac,Cmax} = \omega L_s - \frac{1}{\omega C_{max}} + R_s, \quad (4.20)$$

$$X_{vac,Cmin} = \omega L_s - \frac{1}{\omega C_{min}} + R_s. \quad (4.21)$$

Maximum phase shift range is obtained when series inductive components  $L_s$  is in resonance with the center value of varactor capacitance  $C_o$ . At resonance mode, total reactance is equal to zero and the optimum inductance for maximal relative phase shift is obtained from eq. (4.22), as follows:

$$\left( \omega L_s - \frac{1}{\omega C_{max}} \right) - \left( \omega L_s - \frac{1}{\omega C_{min}} \right) = 0$$

$$L_s = \frac{C_{max} + C_{min}}{2\omega^2 C_{min} C_{max}}. \quad (4.22)$$

$$C_0 = \sqrt{r_c} C_{min} \quad \text{or} \quad C_0 = \frac{C_{max}}{\sqrt{r_c}} \quad (4.23)$$

given that  $r_c = C_{max}/C_{min}$ .

Fig. 4.9 is plotted using eq. (4.11) and parameters in table 4.1 obtained from parametric study. It shows the theoretical prediction of the relative phase shift of the RTPS with respect to the varactor bias voltage for different inductance values. Full 360° phase shift is achieved when the optimum series inductance  $L_s = 0.45$  nH. It is observed that the maximum phase shift range of the RTPS reduced when the varactor inductance deviated from the optimum value  $L_s = 0.45$  nH.

Fig. 4.10 shows the nonlinearity phase increment of the RTPS with respect to the bias voltage applied across the varactor when  $L_s = 0.45$  nH. Linearity is achieved when the characteristic impedance  $Z_{qw}$  of the quarter wavelength transmission line at the reflective load in Figs. 4.4 and 4.5 are increased. However, the phase shift range is reduced. We have to opt for  $Z_{qw} = 20 \Omega$  in our design to realize a full 360° phase shift because of the limitation in the capacitance ratio  $r_c$  of the available commercial varactor.

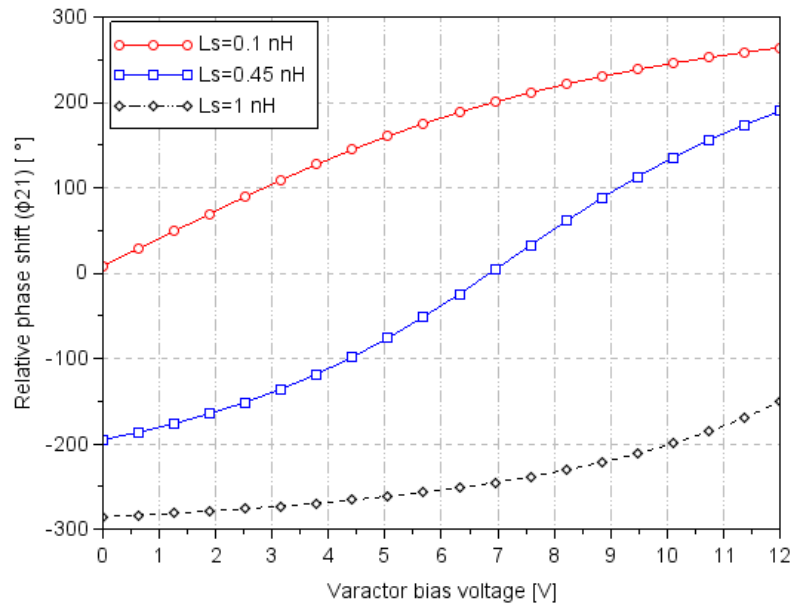


Fig. 4.9 Theoretical calculation of the relative phase shift versus varactor bias voltage ( $L_s$  varies).

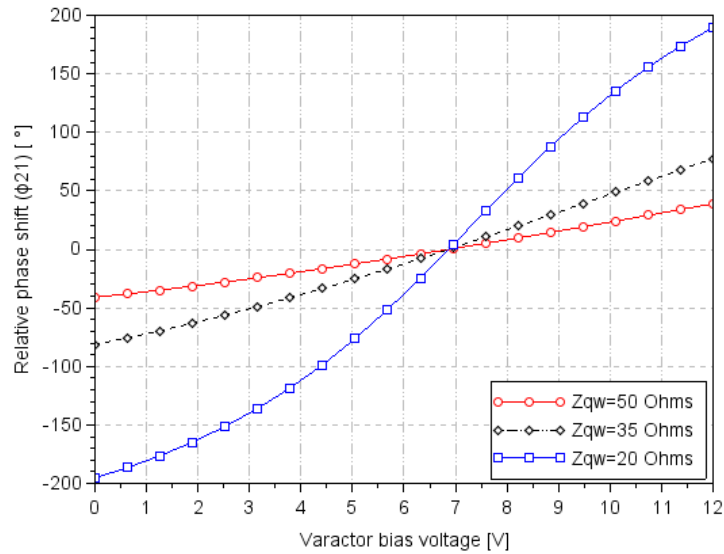


Fig. 4.10 Theoretical calculation of the relative phase shift versus varactor bias voltage ( $Z_{qw}$  varies).

Table 4.1 Design parameters of the RTPS ( $r_z=2$ ).

	$Z_{il}$	$Z_{ol}$	$Z_{qw}$	$R_s$	$C_{min}$	$C_{max}$
RTPS	50 $\Omega$	25 $\Omega$	20 $\Omega$	2.5 $\Omega$	0.45 pF	3.16 pF

#### 4.1.4 Design Implementation and Fabrication

Unknown parameters  $Z_l$  and  $\theta_l$  of the  $\pi$ -section LPF are obtained from the transmission line model and parametric analysis. For ease of comparison,  $45^\circ$ ,  $67.7 \Omega$  open-end stubs are predefined in transmission line model and parametric analysis. Table 4.2 demonstrates that the results ( $Z_l$ ,  $\theta_l$ ) obtained from the transmission line model are close to that of the parametric analysis. The accuracy of the analyses is further verified through the evaluation of fabricated RTPS terminated with commercial packaged silicon tuning varactor diode (Skyworks, SMV2202-040LF). The varactor has junction capacitor ranges from 0.3 pF to 3.14 pF with the series resistance of  $2.5 \Omega$  and parasitic inductance of 0.45 nH. The prototypes were implemented on the FR-4 with the dielectric permittivity of 3.8, loss tangent of 0.02, and substrate thickness of 0.25 mm. Fig. 4.11 shows the final layout for the proposed phase shifter and all important dimensions are listed in table 4.3. The photograph of the distributed elements  $\pi$ -section LPF and proposed phase shifter is illustrated in Fig. 4.12.

Table 4.2 Parameters of  $\pi$ -section LPF obtained from numeric and parametric analysis.

	$Z_s$	$\theta_s$	$Z_l$	$\theta_l$
Transmission line mode	$67.7 \Omega$	$45^\circ$	$26.9 \Omega$	$68.33^\circ$
Parametric analysis ( $r_z=2$ )	$67.7 \Omega$	$45^\circ$	$26.28 \Omega$	$72^\circ$

Table 4.3 Parameters of  $\pi$ -section LPF (unit in mm)

	$W_s$	$W_l$	$W_2$	$W_3$	$W_4$	$W_5$	$W_g$	$W_b$	$l_s$	$l_l$	$l_2$	$l_3$	$l_4$	$l_{g1}$	$l_{g2}$	$l_b$
Proposed RTPS	0.3	0.5	1.4	0.5	2.1	1.5	1	0.8	2.2	6.5	4.3	5.5	7.5	1.5	2	7.4

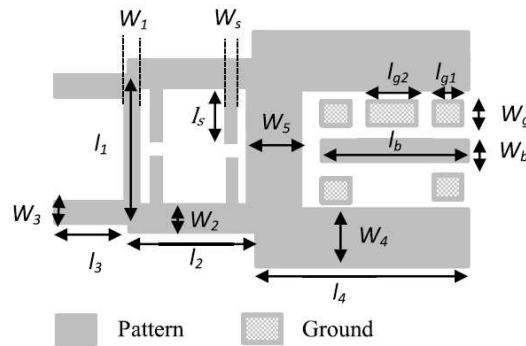


Fig. 4.11 Layout of the full-360°, harmonic-suppressed hybrid coupler phase shifter.



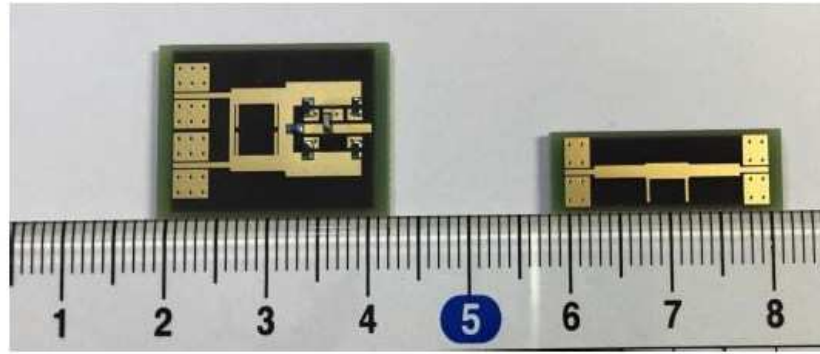


Fig. 4.12 A full 360°, harmonic-suppressed hybrid coupler phase shifter (left) and  $\pi$ -section LPF (right).

#### 4.1.5 Simulation and Measurement Results

Scattering parameters of the  $\pi$ -section LPF and phase shifter were simulated using Ansoft High Frequency Structure Simulator (HFSS) and measurements were performed using Agilent PNA E8361C network analyzer. Fig. 4.13 shows the simulation and measurement results of the  $\pi$ -section LPF at the second harmonic of fundamental frequency. Fig. 4.14 shows the comparison of  $S_{21}$  response of the conventional and harmonic-suppressed phase shifters at the second harmonic at 17.2 GHz. The proposed phase shifter suppresses second harmonic but the frequency where transmission zeros occurs is slightly different from the 50  $\Omega$   $\pi$ -section LPF shown in Fig. 4.13. Frequency is shifted because  $Z_A=25 \Omega$  is assigned to the  $\pi$ -section LPF of the harmonic-suppressed phase shifter in order to obtain  $r_z=2$ . Fig. 4.15 demonstrates that a full 360° phase shift evaluated at 8.6 GHz is achieved in simulations and measurements of the proposed phase shifter. Measured relative phase shift agrees with the simulated one and it is relatively close to the theoretical value (See Fig. 4.6). Nonlinear phase increment occurs because  $Z_{qv}=20 \Omega$  is used in the proposed phase shifter due to the restriction of the commercial varactor. Fig. 4.16 shows the scattering parameters of the harmonic-suppressed phase shifter with respect to the variation of bias voltage applied across varactor. Reflection coefficient at the input and output ports are less than  $-10$  dB, and insertion loss of 5 dB with less than 2 dB variations within the operation bandwidth of

200 MHz are achieved. From our EM simulation, part of insertion loss is due to dielectric loss in the FR-4 substrate. If the substrate with low  $\tan \delta$  such as Rogers RO4350 ( $\tan \delta=0.004$ ) is chosen,  $S_{21}=-3.6\pm0.75$  dB is obtained at 8.6 GHz.

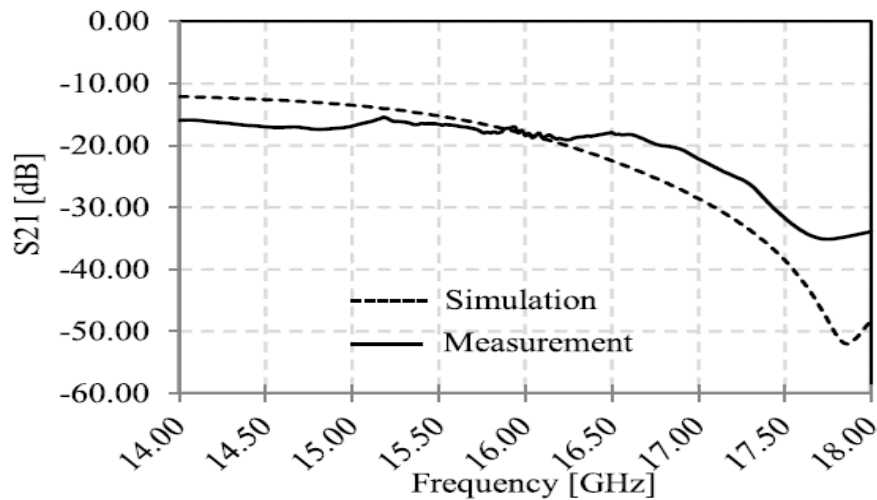


Fig. 4.13 Second harmonic suppression of the  $\pi$ -section LPF at 17.2 GHz. (a) Simulation (dashed) using HFSS (b) Measurement (solid).

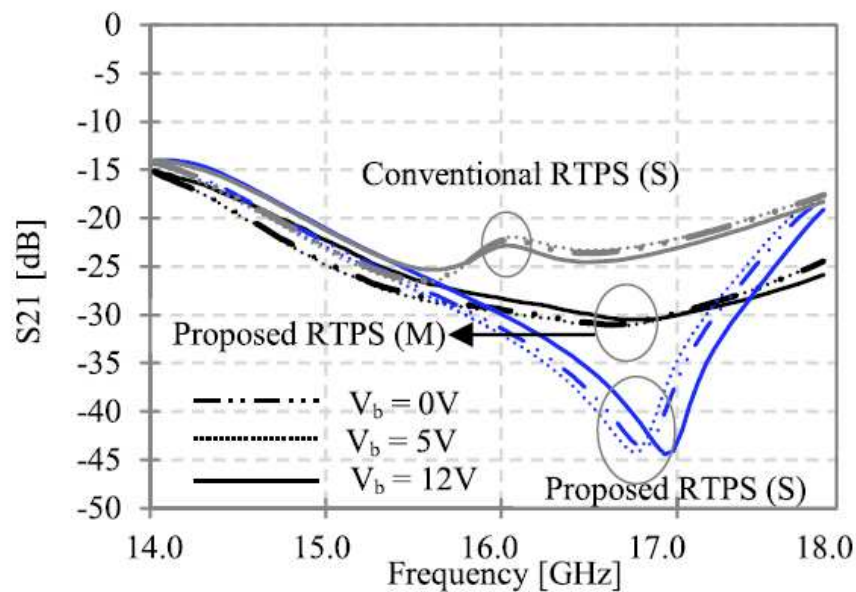


Fig. 4.14 Second harmonic suppression of the proposed phase shifter, in comparison with conventional phase shifter. S represents simulation results from HFSS, and M represents measurements.

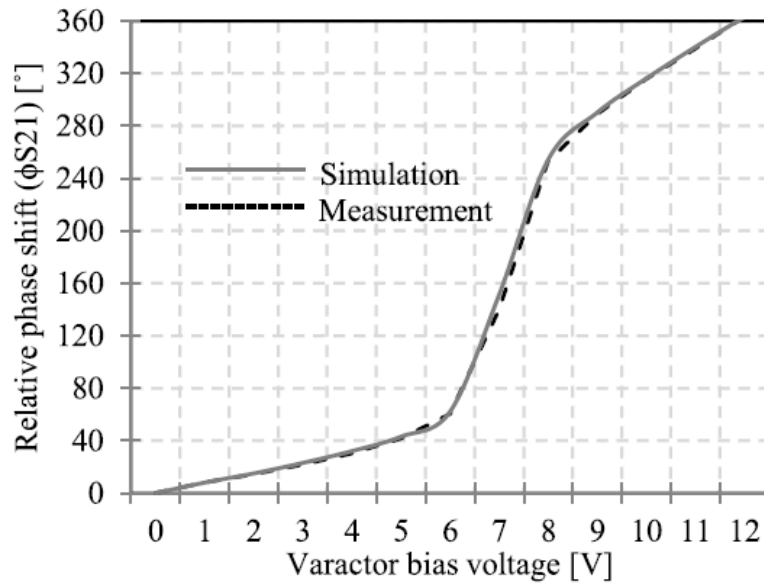


Fig. 4.15 Relative phase shift versus varactor bias voltage evaluated at fundamental frequency of 8.6GHz. Simulation (solid) result from HFSS, and measurement (dashed).

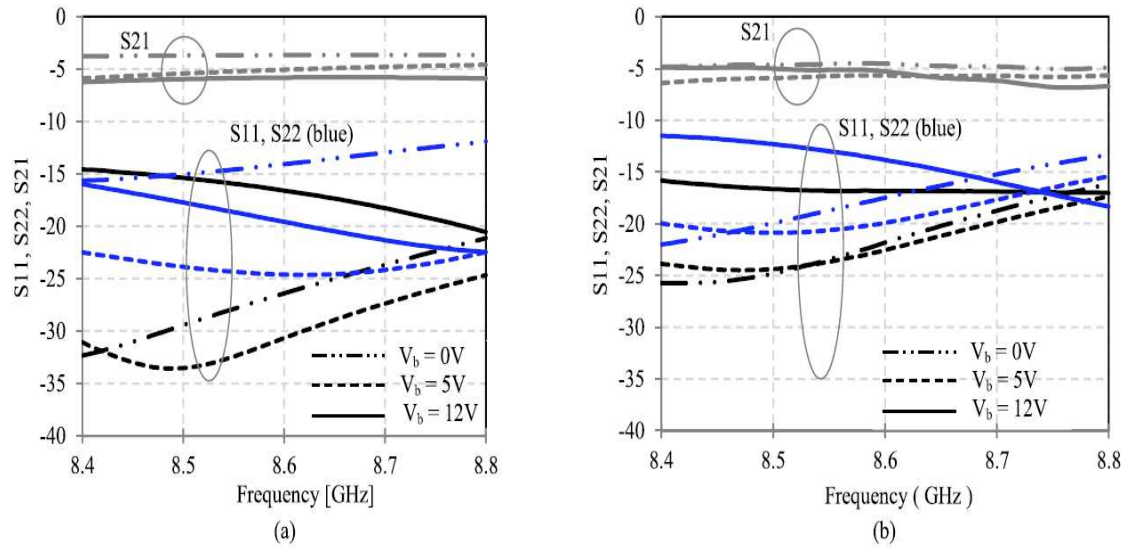


Fig. 4.16  $|S_{11}|$  (black),  $|S_{22}|$  (blue), and  $|S_{21}|$  (grey) of the phase shifter at various varactor bias voltage  $V_b$ . (a) Simulations. (b) Measurements.

## 4.2 Phase Shifter with Discrete Reflective Loads

### 4.2.1 Circuit Analysis

In the design of reflective-type phase shifter (RTPS), hybrid coupler connected to reflection loads with separated by a quarter-wavelength transmission line is essential for full  $360^\circ$  phase shift. Radiation problem arises when it is cascaded to the antenna elements of phased array antenna. In this section, new topology of reflective loads is proposed to overcome null in radiation pattern of phased array antenna. Fig. 4.17 shows proposed phase shifter, which is composed of a hybrid coupler connected to reflection loads. Each reflective load has a varactor terminated to ground and another varactor connected in series with an external inductor. For hybrid coupler, it has input impedance  $Z_{i3}$ , and output port impedance  $Z_{o3}$  at port R1 and R2. Input-to-output impedance ratio  $r_z$  is fixed at 2, same as the ratio of hybrid coupled in phase shifter presented in section 4.1.

As discussed earlier, phase of a travelling wave can be tuned in the conventional RTPS and proposed RTPS by adjusting dynamic range of varactor, as follows:

1. Series resonant at a low bias voltage associated with  $C_{max}$
2. Series resonant at a high bias voltage associated with  $C_{min}$

as demonstrated in eq. (4.19) to (4.21)

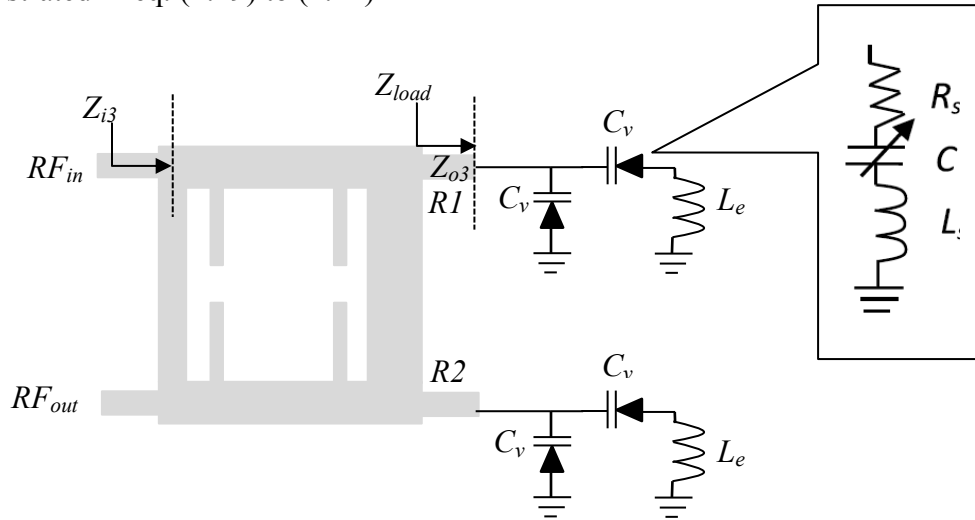


Fig. 4.17 Schematic diagram of phase shifter with discrete reflective loads.

Apart from  $C_{max}$  and  $C_{min}$ , phase doubler circuit such as quarter wavelength transmission line is required to achieve  $360^\circ$  phase shift. In the following section, new topology of reflective loads in the phase shifter (Fig. 4.17) is analyzed to achieve wide phase shift range and near-constant insertion loss. Load impedance can be derived as

$$\begin{aligned} Z_{load} &= (R_s + jX_{vac}) || (R_s + j(X_{vac} + X_l)) \\ &= \frac{(R_s^2 - X_{vac}^2 - X_l - 2Z_{03}R_s) + jR_s(2X_{vac} + X_l)}{2R_s + jR_s(2X_{vac} + X_l)} \end{aligned} \quad (4.24)$$

where  $X_{vac}$  and  $X_l$  are impedances of varactor and external inductor, respectively. The phase shifter is designed at 8.6 GHz. Series inductor  $L_s$  required for the maximum phase shift is calculated using eq. (4.22) and it is accounted into reactance component  $X_{vac}$  of the varactor.  $X_l$  represents impedance of another external inductor cascaded to the anode of the varactor.

The reflection of the reflective loads connected in shunt can be found as

$$\begin{aligned} |\Gamma| &= \frac{Z_{load} - Z_{03}}{Z_{load} + Z_{03}} \\ &= \frac{(R_s^2 - X_{vac}^2 - X_{vac}X_l - 2Z_{03}R_s) + j(2X_{vac} + X_l)(R_s - Z_{03})}{(R_s^2 - X_{vac}^2 - X_{vac}X_l + 2Z_{03}R_s) + j(2X_{vac} + X_l)(R_s + Z_{03})} \end{aligned} \quad (4.25)$$

The maximum phase shift range is realized by terminating ports R1 and R2 of the phase shifter with parallel circuit of reflection loads resonate at difference frequencies. Since the relative phase shift ( $\phi_{S21}$ ) is the phase angle of the reflection coefficient in eq. (4.25), one can compute  $\phi_{S21}$  as,

$$\begin{aligned} \phi_{S21} &= 4\tan^{-1} \left[ \frac{(2X_{vac} + X_l)(R_s - Z_{03})}{(R_s^2 - X_{vac}^2 - X_{vac}X_l - 2Z_{03}R_s)} \right] \\ &\quad - 4\tan^{-1} \left[ \frac{(2X_{vac} + X_l)(R_s + Z_{03})}{(R_s^2 - X_{vac}^2 - X_{vac}X_l + 2Z_{03}R_s)} \right] \end{aligned} \quad (4.26)$$

Maximum phase shift range between the input and output signals over frequencies of interest is obtained by substituting maximum and minimum capacitances of varactor into eq. (4.16), which gives eq. (4.27), shown below

$$\phi_{S_{21}} = \phi_{S_{21}}(C_{min}) - \phi_{S_{21}}(C_{max}) \quad (4.27)$$

Insertion loss between input and output ports is given as,

$$IL = \alpha_l^2 \Gamma^2$$

$$= \alpha_l^2 \frac{[R_s^2 - X_{vac}^2 - X_{vac}X_l - 2Z_{03}R_s]^2 + [R_s(2X_{vac} + X_l)(R_s - Z_{03})]^2}{[R_s^2 - X_{vac}^2 - X_{vac}X_l + 2Z_{03}R_s]^2 + [R_s(2X_{vac} + X_l)(R_s + Z_{03})]^2} \quad (4.28)$$

where  $\alpha_l$  represent transmission loss of the  $-3$ -dB hybrid coupler, which caused by the conductor and dielectric loss of the substrate. Ideal case ( $\alpha_l=1$ ) is considered in our calculation. Calculated insertion loss variation when  $C_{min}=0.2$  pF and  $C_{max}=1$  pF at optimum inductance  $L_e$  is plotted and shown in Fig. 4.19. Fig. 4.20 shows relative phase shift range across frequencies of interest when varactors are varied from 0.2 to 1 pF.

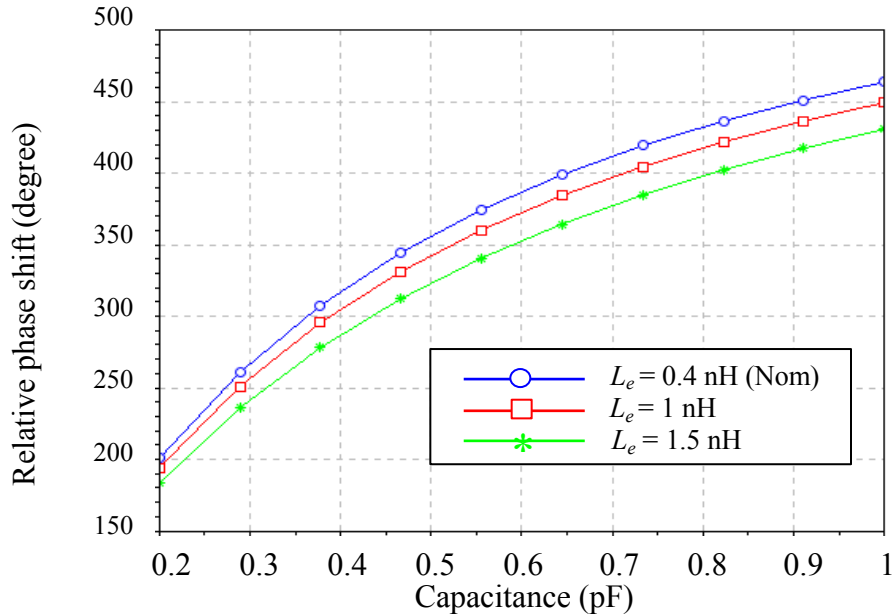


Fig. 4.18 Calculated relative phase shift versus tuning range of varactor at 8.6 GHz ( $L_s = 0.2$  nH,  $Z_{03} = 25 \Omega$ , and  $R_s = 2 \Omega$ ).

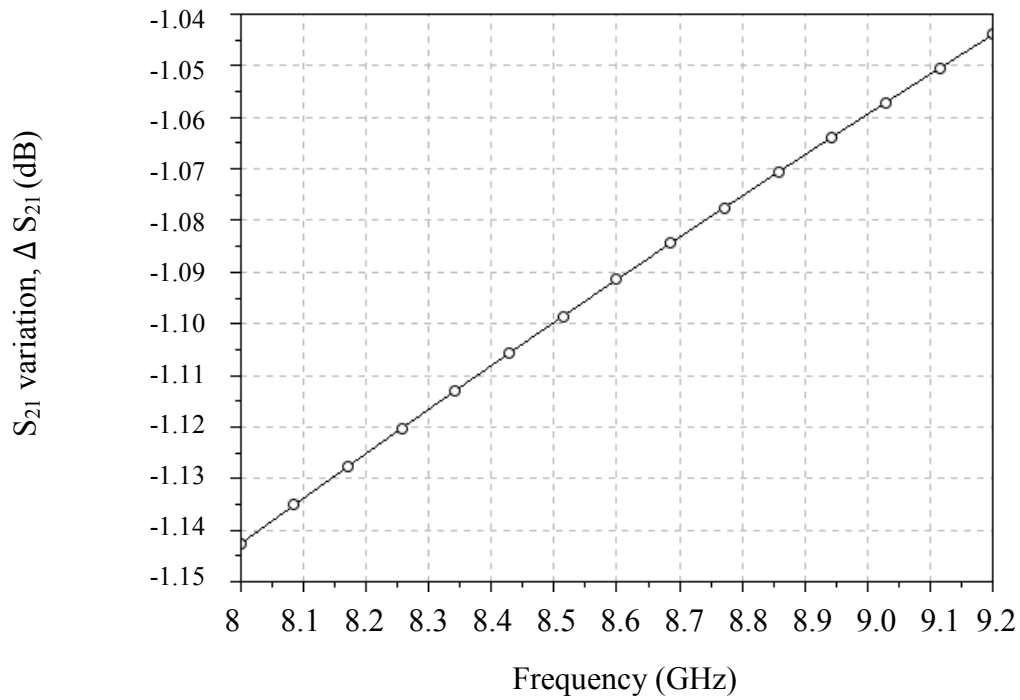


Fig. 4.19 Calculated insertion loss of phase shifter versus tuning range of varactor.

( $L_e = 0.4$  nH,  $L_s = 0.2$  nH,  $C_{min} = 0.2$  pF,  $C_{max} = 1$  pF,  $Z_{03} = 25 \Omega$ , and  $R_s = 2 \Omega$ ).

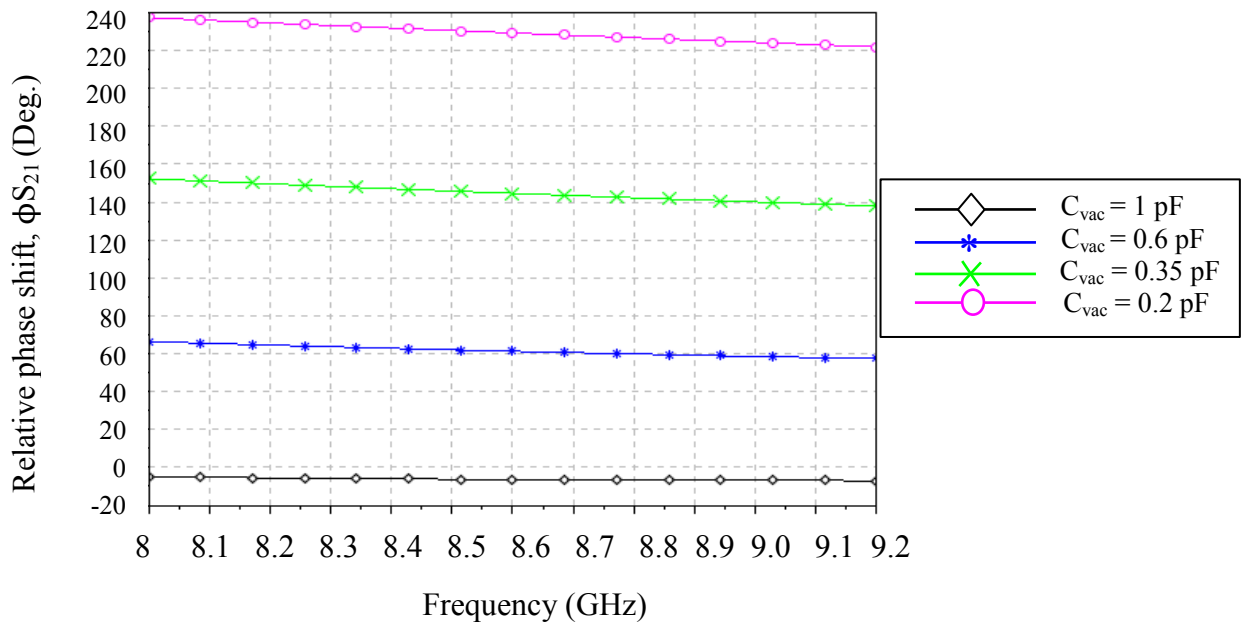


Fig. 4.20 Calculated phase shift across frequencies of interest. ( $L_e = 0.4$  nH,  $L_s = 0.2$  nH,  $Z_{03} = 25 \Omega$ , and  $R_s = 2 \Omega$ ).

### 4.2.2 Design Implementation and Fabrication

Phase shifter was designed at 8.6 GHz with optimal  $L_e$  and implemented on an FR-4 substrate with dielectric constant  $\epsilon_r$  of 0.02, substrate thickness of 0.2 mm and loss tangent  $\tan \delta$  of 0.02. Proposed topology of reflection loads reduces device size and eliminates unwanted radiation at the termination ports of hybrid coupler. Commercial GaAs varactor diodes (Macom, MAVR-000120-1411) in surface-mounted package with  $R_s=0.88 \Omega$ ,  $C_{jo}=1.09$  pF,  $V_j=4.445$  V and  $\gamma_g=1.375$ , were chosen as reflective loads. Input-output port impedance ratio  $r_z$  is chosen as 2, corresponding to the input impedance of  $50 \Omega$ . Open stubs are integrated into the hybrid coupler to filter second harmonics noise. Optimum inductance of external inductor,  $L_e$ , was obtained as 0.4 nH from eq. 4.26 (See fig. 4.18). Final dimensions of the phase shifter are tabulated in table 4.4.

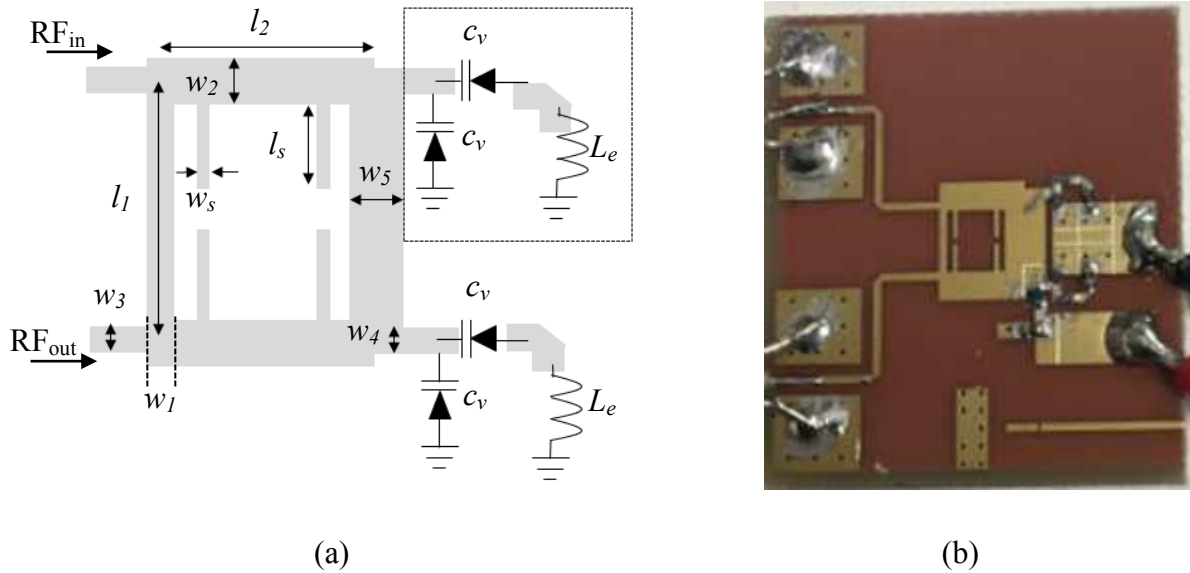


Fig. 4.21 Proposed phase shifter, (a) Optimized design parameters, and (b) photograph of the proposed phase shifter.

Table 4.4 Dimension of phase shifter with discrete loads. (unit in mm)

	$w_s$	$w_1$	$w_2$	$w_3$	$w_4$	$w_5$	$l_s$	$l_1$	$l_2$
Proposed RTPS	0.3	0.5	1.6	0.5	0.6	2.4	1.4	5	4.1



### 4.2.3 Simulation and Measurement Results

Figs. 4.22 and 4.23 show the simulation results of input and output return losses of proposed phased shifter when reverse bias voltage is varied from 0 to 10 V. Input and output return losses ( $S_{11}$  and  $S_{22}$ ) are better than  $-10$  dB from 8.2 GHz to 9.2 GHz. Fig. 4.24 shows the simulated insertion loss obtained,  $S_{21} = -3.3 \pm 0.5$  dB with  $-10$  dB impedance bandwidth of 1 GHz. Low insertion variation  $\pm 0.5$  dB was obtained at the expense of reduced maximum relative phase shift, as depicted in Fig. 4.25. Maximum relative phase shift of  $250^\circ$  is obtained when reverse bias voltage is tuned from 0 to 10 V. Simulations results from full-wave electromagnetic software validates theoretical prediction of relative phase shift range plotted in Fig. 4.20. At the center frequency,  $f_c$  of 8.6 GHz, insertion loss variation is less than  $\pm 0.5$  dB for  $250^\circ$  tuning range. The limitation of the relative phase shift range is partially constraint by commercially available varactor (MACOM, MAVR-000120-1411), 0.2 to 1 pF capacitance range.

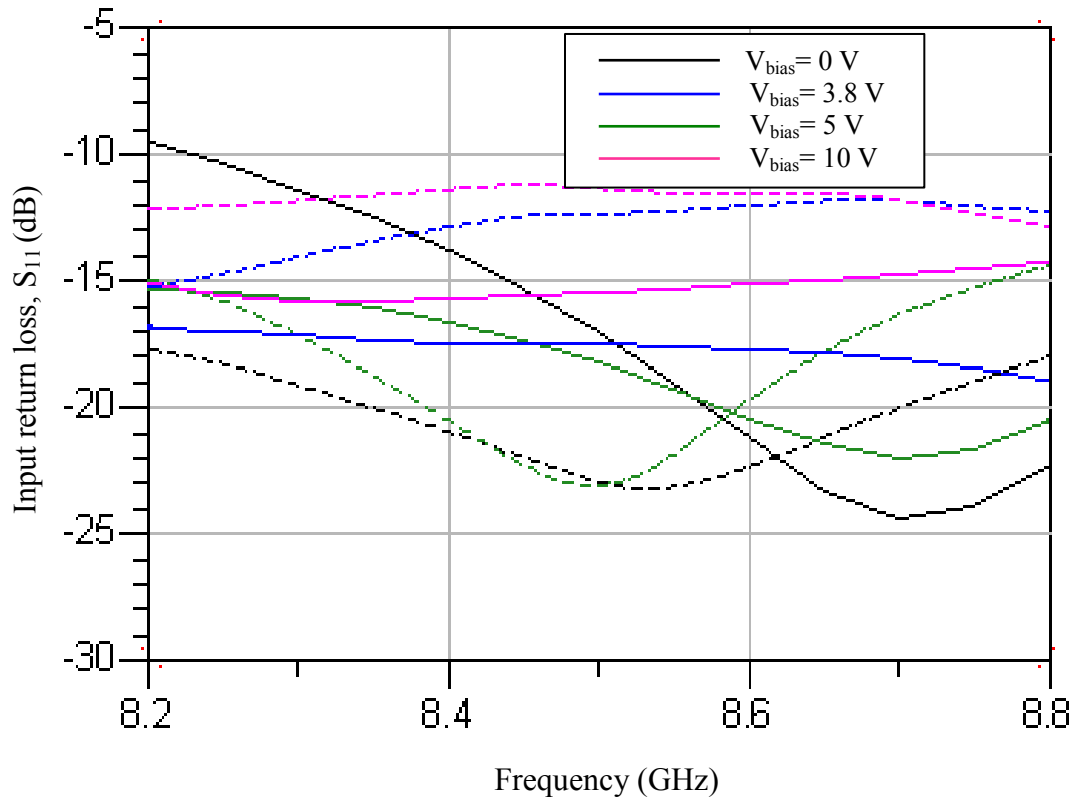


Fig. 4.22 Input return loss  $S_{11}$  of phase shifter, simulation (solid) and measurement (dashed).

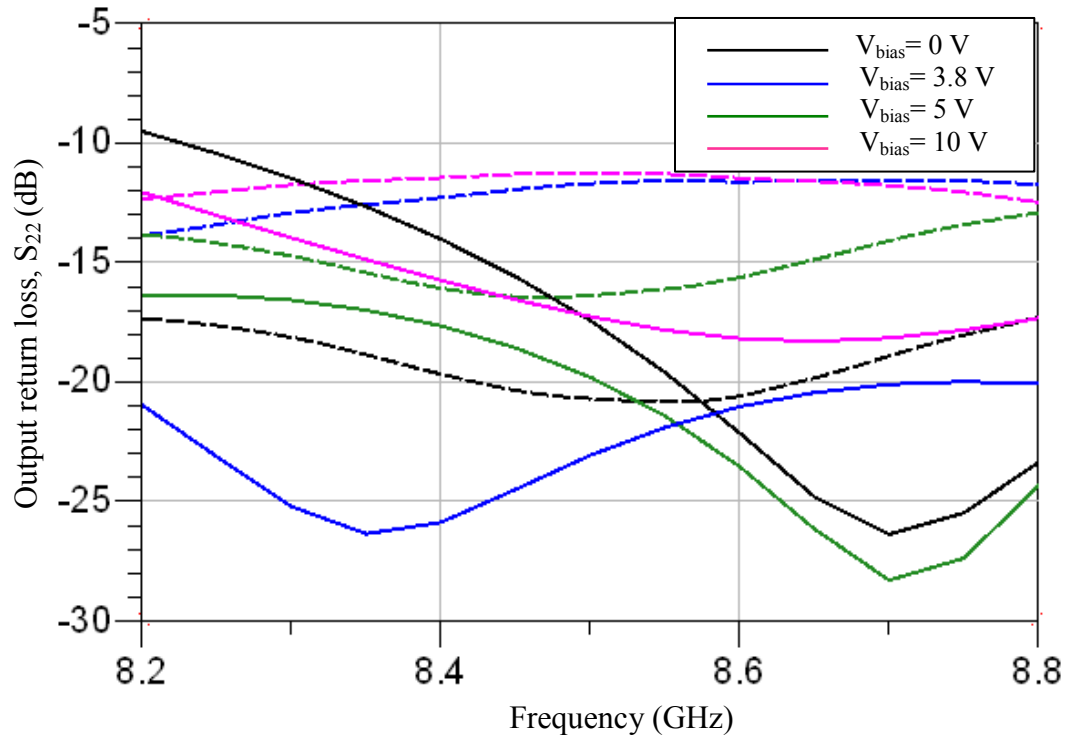


Fig. 4.23 Output return loss  $S_{22}$  of phase shifter, simulation (solid) and measurement (dashed).

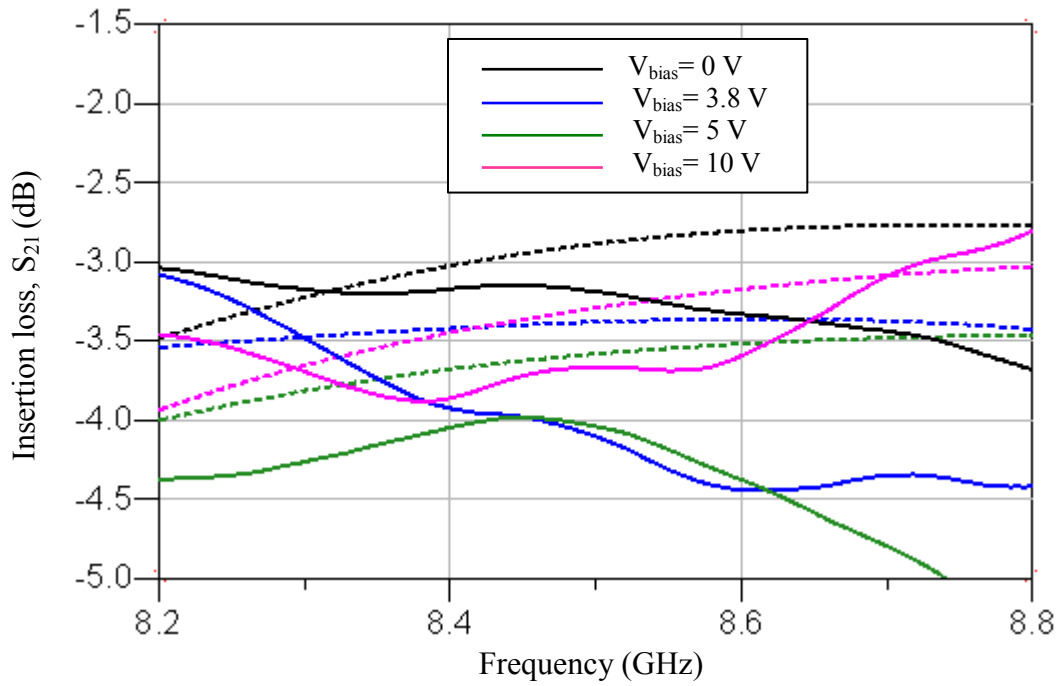


Fig. 4.24 Insertion loss  $S_{21}$  of phase shifter, simulation (solid) and measurement (dashed).

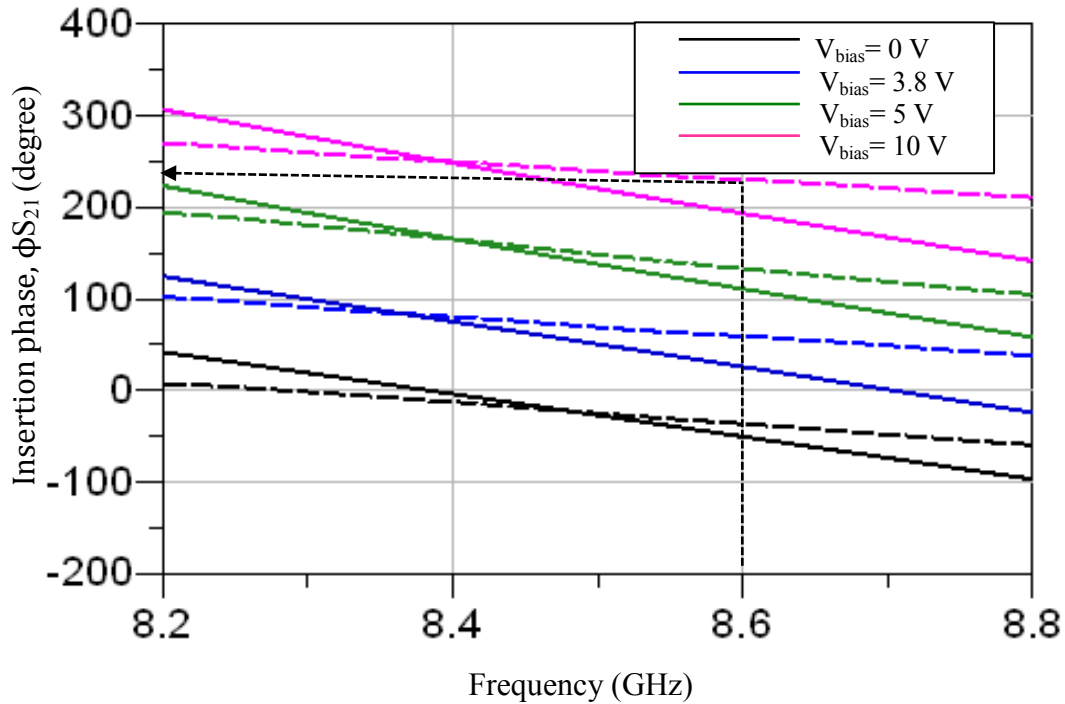


Fig. 4.25 Insertion phase,  $\phi_{S_{21}}$  of phase shifter output, simulation (solid) and measurement (dashed).

#### Electric field distribution

Fig. 4.26 shows the electrical field of conventional phase shifter with  $360^\circ$  relative phase shift range. High electric field density is observed at quarter wavelength transmission line at the output and coupling ports of hybrid coupler. Quarter-wave length transmission line was used to double the phase of reactance loads in order to realize  $360^\circ$  relative phase shift range. Same phase shift technique was implemented in proposed phase shifter in Section 4.1. However, quarter-wavelength lines of the phase shifters become radiators and causes unwanted null in the main beam when they were cascaded to antenna elements in phased array system. Fig. 4.27 shows an improved version of phase shifter with discrete components as reflection loads proposed in Section 4.2. A weak electric field is observed at the pads where discrete components are mounted to. Difference in electric field distribution between two topologies concludes that proposed phase shifter in Section 4.2 can be used for phased array system.

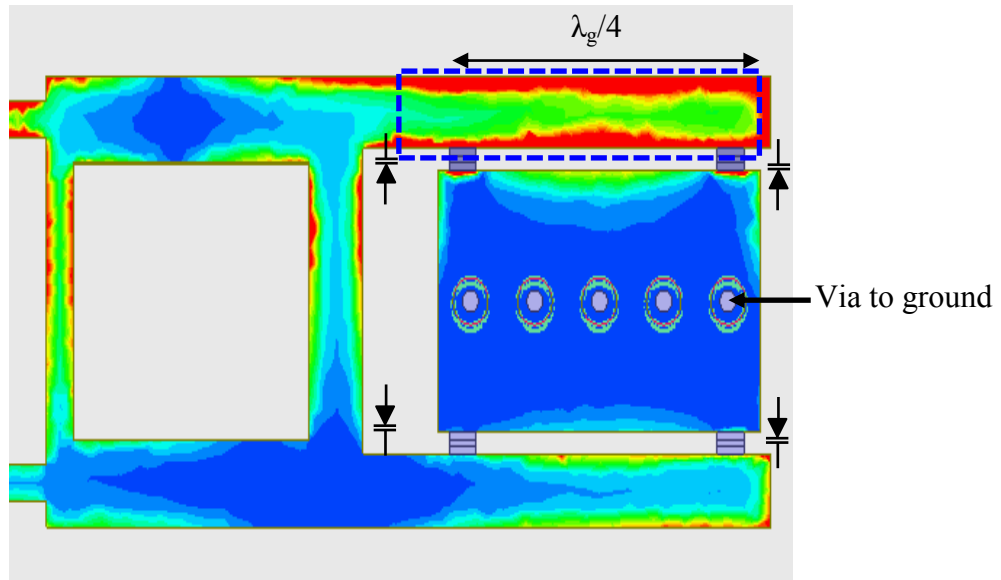


Fig. 4.26 Electric field distribution of conventional phase shifter with reflection loads separated by quarter wave-length transmission line.

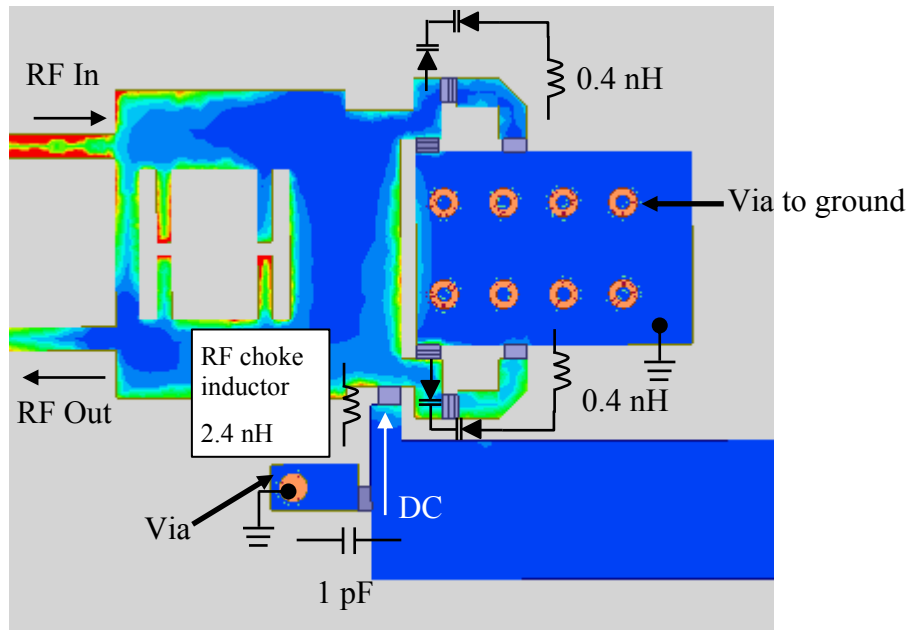


Fig. 4.27 Electric field distribution of proposed phase shifter with discrete reflection loads.

Table 4.4 shows the comparison of the proposed works against other phase shifters found in the literature. In general, lower insertion loss variation is expected in digital phase shifter. However, comparison between [3] and [17] shows that insertion loss variation with respect to the changes in reverse bias voltage, is more related to tangent loss of material used, rather than type of circuit (analog or digital) used. The implementation of phase shifter at high frequency (8 GHz) using PCB manufacturing process is impractical based on the comparison made between [5] and [13]. Insertion loss variation increases from 0.5 dB to 2 dB when operating frequency of PCB-based phase shifter is increased. Discrete reflection loads were proposed in work 2 to reduce insertion loss variation due to microstrip dispersion characteristic at reflective network. Insertion loss lower than  $-4$  dB across operating bandwidth of 600 MHz is achieved in work 2, which is better than other designs. Best to the author's knowledge, the proposed phase shifter is the first reflective-type phase shifter fabricated on PCB at X-band spectrum. Nevertheless, the phase shifter has a relative phase shift range more than  $180^\circ$  and insertion loss better than MMIC-based phase shifters.

Table 4.5 Comparison of proposed works against other phase shifters found in the literature

	[3]	[17]	[5]	Work 1[13]	Work 2
Process	GaAs	SiGe	PCB	PCB	PCB
Type	Analog	Digital	Analog	Analog	Analog
Method	Reflective	Vector sum	Reflective	Reflective	Reflective
Frequency [GHz]	9.5-10.5	8-12	1.95-2.05	8.4-8.8	8.3-8.6
Capacitance ratio, $r$	6	N/A	5.7	7.4	5
Bias voltage	0-32 V	N/A	0-5 V	0-12 V	0-10 V
S <sub>21</sub> [dB]	$-5.3 \pm 0.5$	$-4.5 \pm 1.5$	$-4.7 \pm 0.5$	$-5 \pm 2$	$-3.5 \pm 0.5$
$\Delta\theta_{S21}$	$360^\circ$	$360^\circ$	$360^\circ$	$360^\circ$	$250^\circ$

### 4.3 Chapter Summary

In Section 4.1, full-360° hybrid coupler phase shifter with second harmonic suppression has been presented. Relative phase shift range is determined to be restricted by the port impedance ratio of the phase shifter and series inductance in the reflective load. Transmission line model and parametric analysis were proposed to incorporate  $\pi$ -section LPF in the phase shifter for harmonic suppression, without compromising on the phase range of the phase shifter. The proposed phase shifter was validated through simulations and experiments. However, quarter-wavelength of phase shifters becomes radiators and causes null in the radiation pattern when phased shifters were deployed in the phased-array system. In Section 4.2, an improved version of phase shifter was proposed by introducing discrete components as reflection loads for phased array system. Low insertion loss variation ( $< 1$  dB) and 250° relative phase shift range have been achieved in simulations and experiments.

## References

- [1] R. N. Hardin, E. J. Downey, and J. Munushian, "Electronically variable phase shifter utilizing variable capacitance diodes," *Proc. IRE*, vol. 48, no. 5, pp. 944–945, May 1960.
- [2] C. L. Chen, W. E. Courtney, L. J. Mahoney, M. J. Manfra, A. Chu, and H.A. Atwater, "A Low-Loss Ku-Band Monolithic Analog Phase Shifter," *IEEE Trans. Microw. Theory Techn.*, vol. 35, no. 3, pp. 315–320, March 1987.
- [3] J. I. Upshur and B. D. Geller, "Low-loss 360 degrees X-band analog phase shifter," *IEEE MTT-S Int. Microw. Symp. Dig.*, pp. 487–490, May 1990.
- [4] T. W. Yoo, J. H. Song, and M. S. Park, "360° reflection-type analogue phase shifter implemented with a single 90° branch-line coupler," *IEEE Electronics Lett.*, vol. 33, no. 3, pp. 224–226, Jan. 1997.
- [5] C. S. Lin, S. F. Chang, and W. C. Hsiao, "A Full-360° Reflection Type Phase Shifter With Constant Insertion Loss," *IEEE Microw. Wireless Compon. Lett.*, vol. 18, no. 2, pp. 106–108, Feb. 2008.
- [6] H. Hayashi, T. Nakagawa, and K. Araki, "A miniaturized MMIC analog phase shifter using two quarter-wave-length transmission lines," *IEEE Trans. Microw. Theory Techn.*, vol. 50, no. 1, pp. 150–154, Jan. 2002.
- [7] C. Toker, M. Saglam, M. Ozme, and N. Gunalp, "Branch-line couplers using unequal line lengths," *IEEE Trans. Microw. Theory Techn.*, vol. 49, no. 4, pp. 718–721, April 2001.
- [8] S. S. Liao, P. T. Sun, N.-C. Chin, and J.-T. Peng, "A novel compact size branch-line coupler," *IEEE Microw. Wireless Compon. Lett.*, vol. 15, no. 9, pp. 588–590, Sept. 2005.
- [9] Y. H. Chun and J. S. Hong, "Compact Wide-Band Branch-Line Hybrids," *IEEE Trans. Microw. Theory Techn.*, vol. 54, no. 2, pp. 704–709, Feb. 2006.

- [10] S. Cheng, E. Ojefors, P. Hallbjorner, and A. Rydberg, "Compact reflective microstrip phase shifter for traveling wave antenna applications," *IEEE Microw. Wireless Compon. Lett.*, vol. 16, no. 7, pp. 431–433, July 2006.
- [11] K. Y. Tsai, H.-S. Yang, J. H. Chen, and Y.-J.E. Chen, "A Miniaturized 3 dB Branch-Line Hybrid Coupler With Harmonics Suppression," *IEEE Microw. Wireless Compon. Lett.*, vol. 21, no. 10, pp. 537–539, Oct. 2011.
- [12] J. Kim and J. G. Yook, "A Miniaturized 3 dB 90° Hybrid Coupler Using Coupled-Line Section With Spurious Rejection," *IEEE Microw. Wireless Compon. Lett.*, vol. 24, no. 11, pp. 766–768, Nov. 2014.
- [13] C. E. Guan, A. I. A. Galal, N. Mizoguchi, A. Ishikawa, S. Fukugawa, R. Kitaya and H. Kanaya, "Analysis and Design of a Full 360 degrees, Harmonic-Suppressed Hybrid Coupler Phase Shifter," *IEICE Trans. Electron.*, vol. E100–C, no. 10, pp. 875-883, Oct. 2017.
- [14] H. Kanaya, T. Shinto, K. Yoshida, T. Uchiyama, and Z. Wang, "Miniaturized HTS coplanar waveguide bandpass filters with highly packed meanderlines," *IEEE Trans. Appl. Supercond.*, vol. 11, no. 1, pp. 481–484, March 2001.
- [15] I. J. Bahl and D. K. Trivedi, "A Designer's Guide to Microstrip Line," *Microwaves*, pp. 174–182, May 1977.
- [16] P. A. Garcia, N. E. Lopez, L. F. H. Ontanon, and F. L. H. Andres, "Complex Impedance Transformers Based on Branch-Line Hybrid Couplers," *Progress In Electromagnetics Research C*; vol. 69, pp. 147–157, 2016.
- [17] B. Cetindogan, E. Ozeren, B. Ustundag, M. Kaynak, and Y. Gurbuz, "A 6 bit vector-sum phase shifter with a decoder based control circuit for X-band phased-arrays," *IEEE Microw. Wireless Compon. Lett.*, vol. 26, no. 1, pp.64-66, Jan. 2016.



## Chapter 5

### Phased Array Antenna

The application of phased array antenna has been extended from airborne radar systems such as satellite communication to ground-based radar system, for example Lidar in self-driving car and RFID wireless locating system [1]. In order to meet the requirements of consumer applications, compact and reasonably low-priced electronically steerable antenna array is required. Cost of the final product depends on the phase-shift technology and devices integration in phased array system.

As mentioned earlier, phase shifters are the core and most expensive components in the phased array antenna. It can be realized using digital circuit or analog circuit. At high frequency, analog phase shifters could be realized at lower cost compared to its digital counterpart. Varactor diodes and PIN diodes are the most common semiconductor device used in analog phase shifter to realize low cost design [1]-[6]. Conventional phase shifter is unfitted for phased array system because quarter-wavelength transmission line at the phase shifter reflective network causes null in radiation pattern. By reducing reflective load to single varactor diode, unwanted radiation from the phase shifter is eliminated but relative phase shift range is drastically reduced to  $180^\circ$  phase shift. This is one of the main reason series feeding network was widely used to realize large scan angle in phased array antenna [5]-[8]. As we know, the cumulative nature of the phase shift in series-fed network enables large scan angle with a small relative phase shift range. However, insertion loss and phase delay of the phased array antenna increase when the number of stages of phase shifters increases.

Accumulated group delay from multiple stages phase shifters causes beam squint [4]-[5]. Beam squint is referred to the pointing angle of main beam deviates from desired scan angle across frequencies of interest. Only small phase shift range is required by phase shifters in series-fed phased array antenna. We could observe that phase shifters deployed in series-fed antenna arrays always have a small relative phase shift range. Beam squint in corporate-fed network is lower than series-fed network because of low group delay. But relatively large phase shift are required for large scan angle in corporate-fed network hinders many researchers from developing corporate-fed phased array antenna. In this work, passive elements are proposed to enhance the scan angle range of corporate-fed phased array antenna, which is limited by phase shifters with a  $250^\circ$  relative phase shift range.

In recent years, electronically steerable passive array radiator (ESPAR) has been studied for analog beam steering [13], [14]. ESPAR consists of a single active antenna and few passive antenna elements mutually coupled to neighbor active antenna element. Currents are induced at the passive antenna, in which phase of currents at passive antenna elements can be tuned by varying the reactance of termination capacitor at the passive antenna elements. By altering input impedance at the passive antenna, beam is steered without the need of phase shifter. Simple ESPAR architecture makes it a good alternative to the conventional phased antenna array, especially in lightweight and battery-power devices with size constraints.

In the following section, floating parasitic antenna elements are chosen to increase the scan angle of corporate-fed phased array antenna. As opposed to ESPAR architecture, floating metals are chosen as parasitic antennas in this work. System ground and floating parasitic antennas are not connected to each other, electrically or electromagnetically. Therefore, radiation pattern and input impedance of phased array antenna at the broadside direction is not affected by the parasitic antennas, since floating parasitic antennas are an open circuit. Current is induced at parasitic elements only when beam is scanned towards end-fire direction. Mutual coupling between parasitic antennas and active antenna array increases scan angle of the phased array antenna.

### 5.1 Phased Array Antenna Architecture

Assume that phased antenna array is used as transmitter, and similarly, same operation concept is held for receiver. Fig. 5.1 shows phased array antenna consists of four antenna elements which are individually connected to the RTPS in corporate-fed network. Incident RF signals propagate from antenna to RTPS are combined at the corporate-fed network constructed from Wilkinson power combiner/divider discussed in section 3.2. Antenna elements, phase shifters, and input and output ports of Wilkinson power dividers are matched to the transmission line characteristic impedance ( $50 \Omega$ ). Noted that it is crucial to avoid the presence of grating lobes in the radiation pattern, thus antenna elements are spaced apart by  $\lambda_0/2$ , where  $\lambda_0$  is the free space wavelength of RF signals. RF signals at phase shifters' output port are in-phase when main beam radiates at broadside direction during no steering condition. In order to steer beam to scan angle of  $\theta$ , phase weight coefficients with progressive phase shift of  $n\phi$  should be applied to  $n$ -stage antenna elements in phased array system. Progressive phase shifts can be calculated from eq. (2.17) in Chapter 2. Required phase shifts required for  $\pm 25^\circ$  scan angle are listed in Table 5.1. Total relative phase shift range of  $228^\circ$  is required to steer 1x4 elements phased array antenna to  $\pm 25^\circ$  (see Fig. 5.1). Theoretically, relative phase shift range of  $270^\circ$  is needed to steer beam to  $\pm 30^\circ$  for 1x4 elements phased array antenna.

Table 5.1 Progressive phase shift required for beam steering from  $-25^\circ$  to  $+25^\circ$ .

Scan Angle	$\phi_{PS1} [V_{bias1}]$		$\phi_{PS2} [V_{bias2}]$		$\phi_{PS3} [V_{bias3}]$		$\phi_{PS4} [V_{bias4}]$	
$-25^\circ$	$0^\circ$	0 V	$76.1^\circ$	3.8 V	$152^\circ$	5 V	$228^\circ$	10 V
$-15^\circ$	$0^\circ$	0 V	$46.6^\circ$	2.8 V	$93.2^\circ$	4 V	$140^\circ$	4.8 V
$-5^\circ$	$0^\circ$	0 V	$15.7^\circ$	1.5 V	$31.4^\circ$	2.6 V	$47.1^\circ$	2.9 V
0	$0^\circ$	0 V	$0^\circ$	0 V	$0^\circ$	0 V	$0^\circ$	0 V
$+5^\circ$	$47.1^\circ$	2.9 V	$31.4^\circ$	2.6 V	$15.7^\circ$	1.5 V	$0^\circ$	0 V
$+15^\circ$	$140^\circ$	4.8 V	$93.2^\circ$	4 V	$46.6^\circ$	2.8 V	$0^\circ$	0 V
$+25^\circ$	$228^\circ$	10 V	$152^\circ$	5 V	$76.1^\circ$	3.8 V	$0^\circ$	0 V

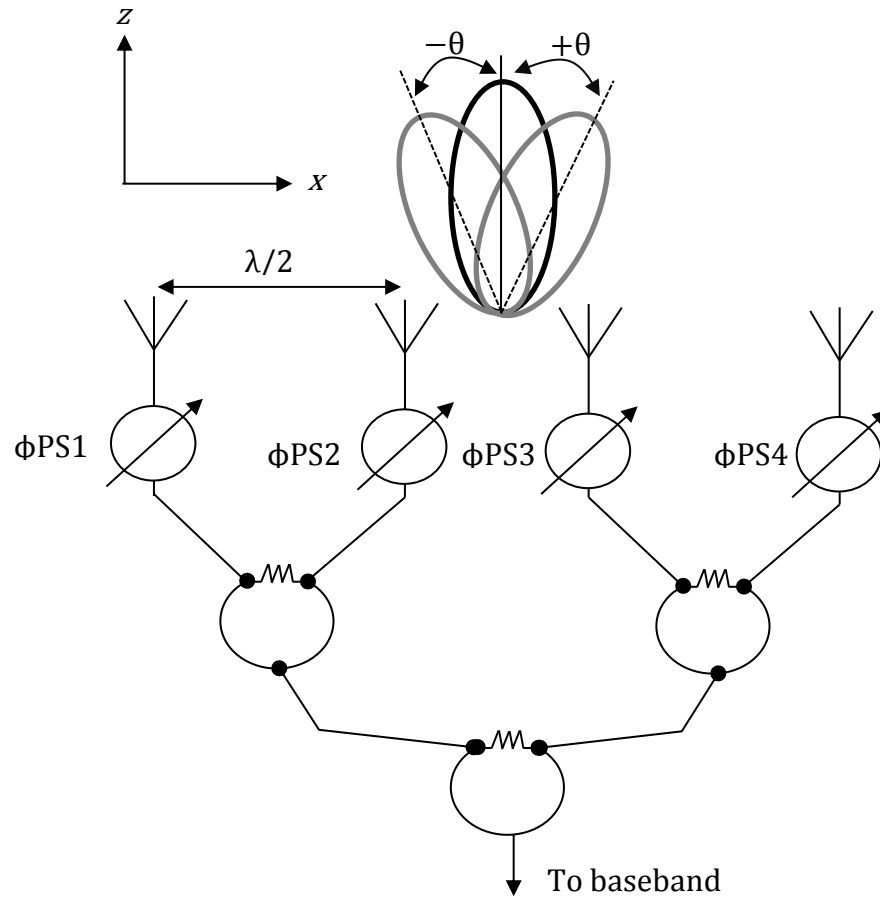


Fig. 5.1 Corporate-fed phased array antenna with the proposed phase shifter.

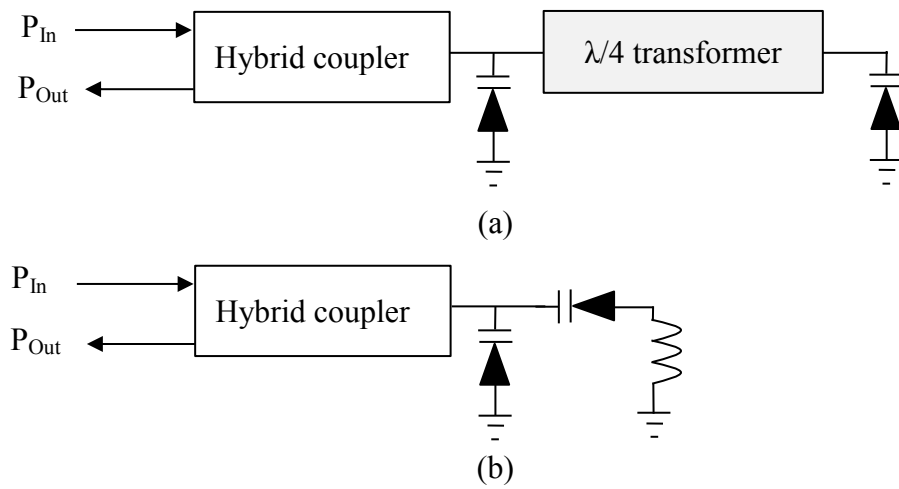


Fig. 5.2 Phase shifter with different reflection loads topology. (a) Conventional phase shifter. (b) Proposed phase shifter with discrete reflective loads.

Conventional phase shifter in Fig. 5.2(a) has a  $360^\circ$  phase shift range but it is not suitable to be deployed in phased array antenna due to the radiative nature of quarter-wavelength transmission line. Author proposes phase shifter with reflective network composed of discrete loads for phased array antenna application, as depicted in Fig. 5.2(b). The phase shifter consists of reflection loads connected in parallel, in which one of the varactor diode is terminated by discrete inductor to eliminate unwanted radiation. Low insertion loss variation ( $<1$  dB) for all bias voltages is achieved and it allows uniform power distribution to all antenna elements. The only demerit of the phase shifter is the maximum phase shift range is limited to  $250^\circ$ , due to the capacitance tuning range of the commercially varactor (with  $C_{min}=0.2$  pF and  $C_{max}=1$  pF). The device restricts phase difference between adjacent antenna elements to  $83.3^\circ$  for  $1 \times 4$  linear phased array antenna. Table 5.2 shows the influence of parasitic antenna on the scan angle of phased array, composed of phase shifters with limited phase shift range. In this work, parasitic antennas are introduced to extend scan angle range from  $55^\circ$  to  $60^\circ$ .

## 5.2 Parasitic Element For Scan Angle Enhancement

Two parasitic antennas are placed on the left and right side of phased array antenna for mutual coupling. They are spaced apart from neighbor active antennas by one-half of free space wavelength. When the beam is steered over threshold scan angle,  $\theta_t$ , mutual coupling occurs between floating parasitic antennas and active antenna elements driven by phase shifters. Currents are induced at the adjacent floating parasitic antennas on the metal surface. Induced current creates electric dipoles at the edges of the antennas. Let's consider an active dipole antenna and a parasitic antenna shown in Fig. 5.3. Active antenna is driven by a voltage generator,  $V_g$ , and current,  $I$ , flows along the antenna.

Table 5.2 Comparison of phased array antenna with and without parasitic element.

Number of antenna elements	Number of parasitic antenna	Required phase difference between adjacent elements	Calculated scan angle
4	0	$83.3^\circ$	$27.5^\circ$
4	2	$83.3^\circ$	$30^\circ$

When parasitic antenna is brought closer to the neighborhood of active dipole antenna, current  $I_2$  is induced on parasitic antenna and current flows along active dipole antenna is reduced to  $I_1$ . This phenomenon is known as mutual coupling where,

$$I = I_1 + I_2 . \quad (5.1)$$

The resultant voltage at active dipole antenna is expressed as,

$$V_1 = Z_{11}I_1 + Z_{12}I_2 \quad (5.2)$$

$$\text{and voltage at parasitic antenna, } V_2 = Z_{21}I_1 + Z_{22}I_2. \quad (5.3)$$

Voltages and currents at the two-port network are related by the  $Z$ -matrix:

$$\begin{bmatrix} V_1 \\ V_2 \end{bmatrix} = \begin{bmatrix} Z_{11} & Z_{12} \\ Z_{21} & Z_{22} \end{bmatrix} \begin{bmatrix} I_1 \\ I_2 \end{bmatrix} \quad (5.4)$$

with

$$Z_{11} = \left. \frac{V_1}{I_1} \right|_{I_2=0}, Z_{12} = \left. \frac{V_1}{I_2} \right|_{I_1=0}, Z_{21} = \left. \frac{V_2}{I_1} \right|_{I_2=0}, Z_{22} = \left. \frac{V_2}{I_2} \right|_{I_1=0} \quad (5.5)$$

$Z_{12}$  and  $Z_{21}$  are known as the active impedance.  $Z_{11}$  and  $Z_{22}$  are input impedance of active dipole antenna and parasitic antenna.

When current is induced at parasitic antenna, the mutual coupling does not only affect the input impedances of the active element in the array, but it also alters radiation pattern of scanned beam. When beam is steered to scan angle,  $\theta_s$ , maximum current  $I_2$  is induced on the parasitic antenna for  $Z_{12}=Z_{21}$  due to antenna reciprocity. Array factor of active and parasitic antennas is written in [13] as,

$$AF = 1 + \frac{I_2}{I_1} e^{-jkd \cos \theta_s}. \quad (5.6)$$

$k$  is the propagation wavenumber and  $d$  is the separation distance between parasitic antenna and its neighbor active driven antenna. In general, it will be difficult to calculate array factor in phased array antenna with mutual effects. For phased array antenna in this work, distance between active driven antenna and parasitic antenna  $d$  is assumed to be a constant.

For the sake of simplicity in our analysis,  $d$  is fixed to one-half of free space wavelength, so that AF becomes a function of scan angle  $\theta_s$ :

$$AF = 1 + \frac{I_2}{I_1} e^{-j\pi \cos \theta_s}. \quad (5.7)$$

Parametric study is performed in full-wave electromagnetic software to find optimum dimension of parasitic antenna. Fig. 5.4 shows electric field distributed on the floating parasitic antenna when mutual coupling occurs at scan angle close to the end-fire direction ( $+30^\circ$ ). Induced current at the floating parasitic antenna increases the maximum scan angle range from  $55^\circ$  to  $60^\circ$  by merely applying relative phase shift range of  $250^\circ$  to  $1 \times 4$  elements phased array antenna.

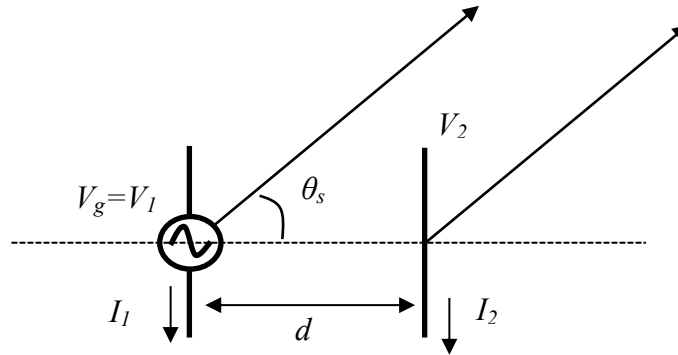


Fig. 5.3 Mutual coupling between active dipole antenna and parasitic antenna.

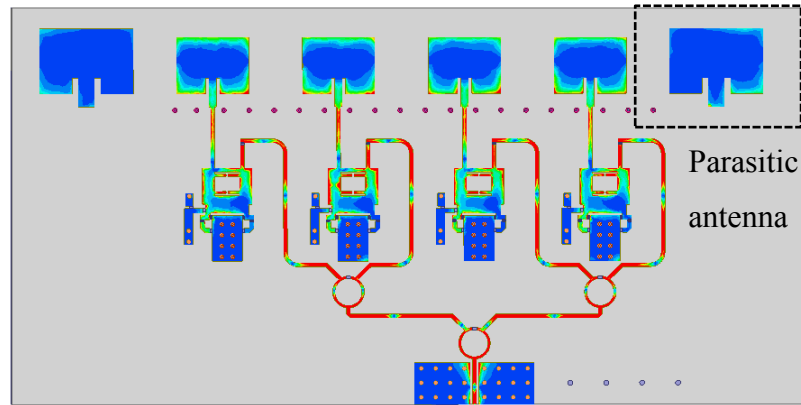


Fig. 5.4 Electric field distribution at scan angle of  $+30^\circ$

### 5.3 Design Implementation and Fabrication

Phased array antenna was fabricated on multi-layer PCB process to achieve low profile, compact and robust design. It is designed to operate at the 8.6 GHz of X band spectrum for wide band response and to be fabricated on FR-4 with dielectric constant,  $\epsilon_r=4.2$  and tangent loss  $\tan \delta=0.02$ . Four identical patches are used as antenna elements. Microstrip patch antenna was fabricated on 1.6 mm FR-4 while Wilkinson power dividers and phase shifters were fabricated on 0.2 mm FR-4. In order to combine antenna elements, phase shifters, and Wilkinson power divider into a single module multiple layers PCB manufacturing process was chosen. Fig. 5.5 shows the top and bottom views of phased array antenna fabricated on four layers PCB.

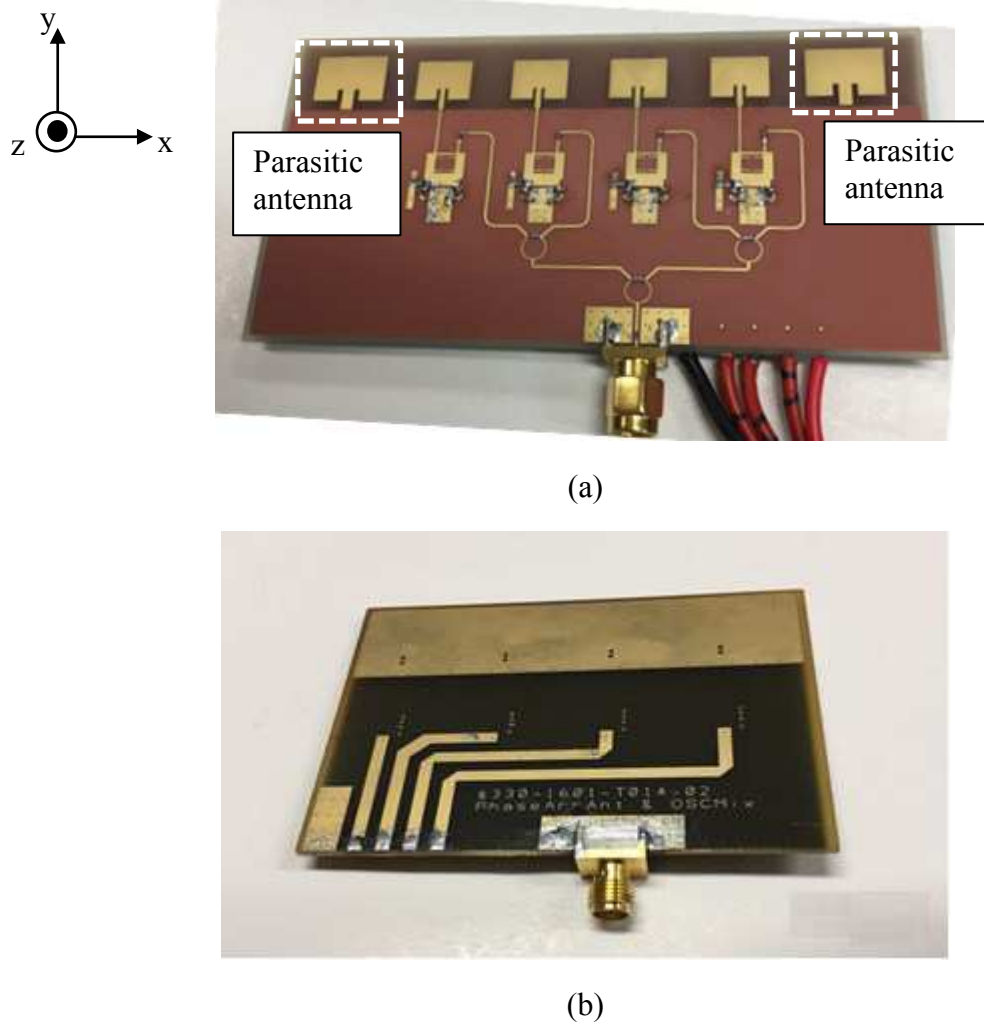


Fig. 5.5 Prototype of phased array antenna (74.5 mm x 46.8 mm). (a) Top view. (b) Bottom view.



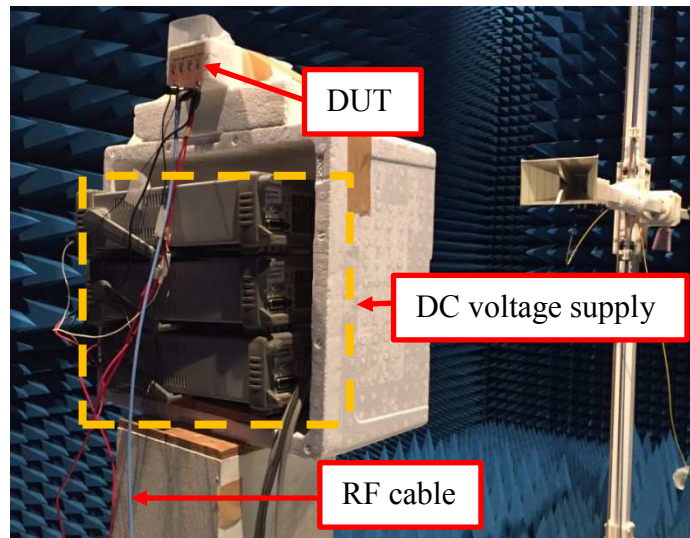


Fig. 5.6 Phased array antenna measurement setup in anechoic chamber.

Fig. 5.6 shows radiation pattern measurement setup in anechoic chamber. Double ridge horn antenna was used as transmitter and signals received at the phased array antenna were normalized to obtain antenna radiation pattern. DC bias voltages are applied to copper traces at the bottom layer for beam scanning. Those traces are electrically connected to the phase shifter at the top layer. Realized gain of the array antenna was calculated using Friss transmission equation.

## 5.4 Simulation and Measurement results

### 5.4.1 S-parameter

Fig. 5.7 shows return loss ( $S_{11}$ ) versus frequencies of interest. Good return loss of phase array antenna (lower than  $-10$  dB) is observed from 8.4 GHz to 9 GHz, for scan angle from  $-30^\circ$  to  $+30^\circ$ . Curve of return loss changes when phased array antenna is steered to the maximum scan angle. At the maximum scan angle, mutual coupling occurs between parasitic and active antenna elements. As a result, input impedance of phased array system changes due to induced current at the parasitic antenna.

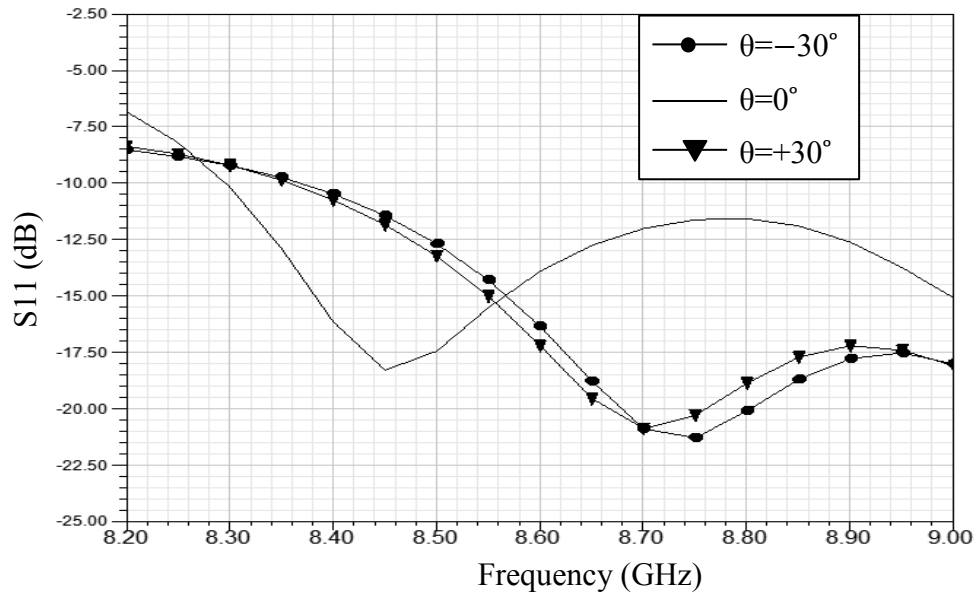


Fig. 5.7 Return losses of phased array antenna at various scan angle.

#### 5.4.2 Maximize Scan Angle Using Parasitic Antenna

Fig. 5.8 shows the vector of induced surface current on parasitic antenna when scan angle of phased array antenna is set to  $+30^\circ$ . It is observed that induced current on the parasitic antenna lags the ones in the active driven antenna by more than  $180^\circ$ . Dimensions of the parasitic antenna,  $w_p$  and  $l_p$ , not only determine net current withdrawn from the active driven antenna, but it also affects phase of the induced current at parasitic antennas.  $w_p$  and  $l_p$  are optimized in full wave electromagnetic simulation tool in order to obtain desired phase shift for maximum scan angle.

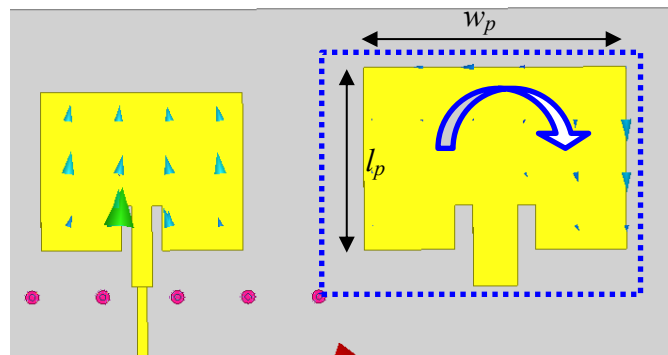


Fig. 5.8 Induced current at the floating parasitic antenna.

### 5.4.3 Far-field Radiation and Realized Gain

Fig. 5.9 shows simulation and measurements of broadside far-field radiation pattern at 8.6 GHz. Fig. 5.9(a) and (b) show simulated and measured radiation patterns at  $xz$ -plane of Fig. 5.5 while Fig. 5.9 (c) shows simulated 3D radiation pattern. By varying the bias voltages to the phase shifters, radiation beams were steered to  $-10^\circ$  and  $+10^\circ$ , as depicted in Figs. 5.10 and 5.11, respectively. It is observed that measurement results match to simulated radiation patterns from full-wave electromagnetic simulation tool. When the reverse biased voltages are increased, the scan angle is steered towards the end-fire direction. As we know,  $-30^\circ$  to  $+30^\circ$  beam steering range for corporate-fed phased array antenna requires large phase shift range, thus large reverse bias voltage is required to tune varactor to achieve large reactance variation. In this work, author proposes parasitic antennas to realize maximum scan angle of  $\pm 30^\circ$  using reverse bias voltage of 10 V, as demonstrated in Figs. 5.12 and 5.13. By using reverse bias voltage of 10 V, the proposed phased array antenna supports grating-lobe-free scanning with maximum scan angle range of  $60^\circ$ .

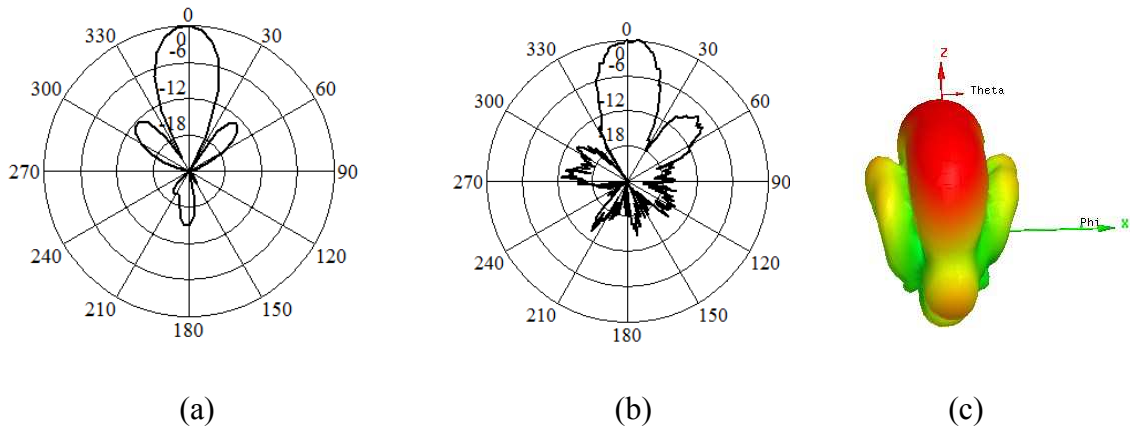


Fig. 5.9 Radiation pattern at scan angle,  $\theta=0^\circ$  and center frequency,  $f_c=8.6$  GHz ( $xz$ -plane). (a) Simulation. (b) Measurement. (c) Simulated 3D radiation pattern.

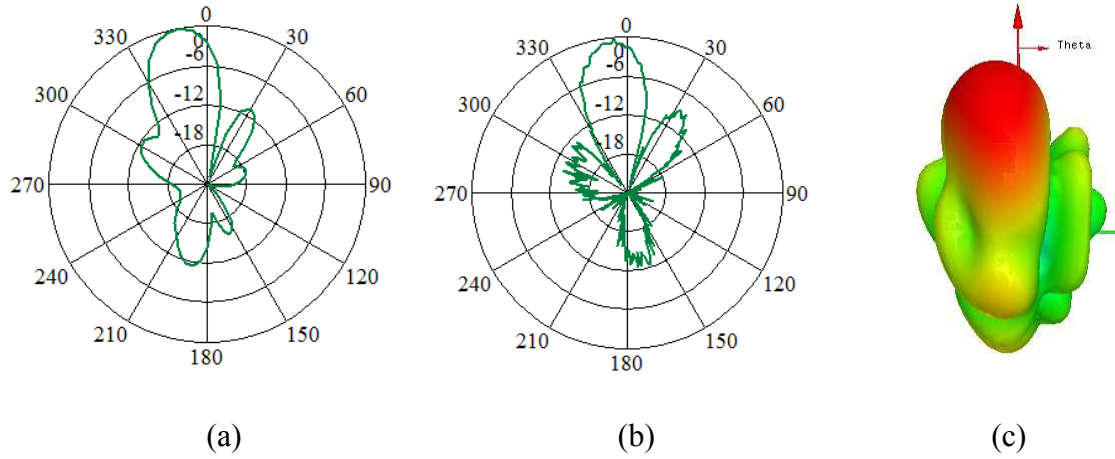


Fig 5.10 Radiation pattern at scan angle,  $\theta = -10^\circ$  and center frequency,  $f_c = 8.6$  GHz (xz-plane). (a) Simulation. (b) Measurement. (c) Simulated 3D radiation pattern.

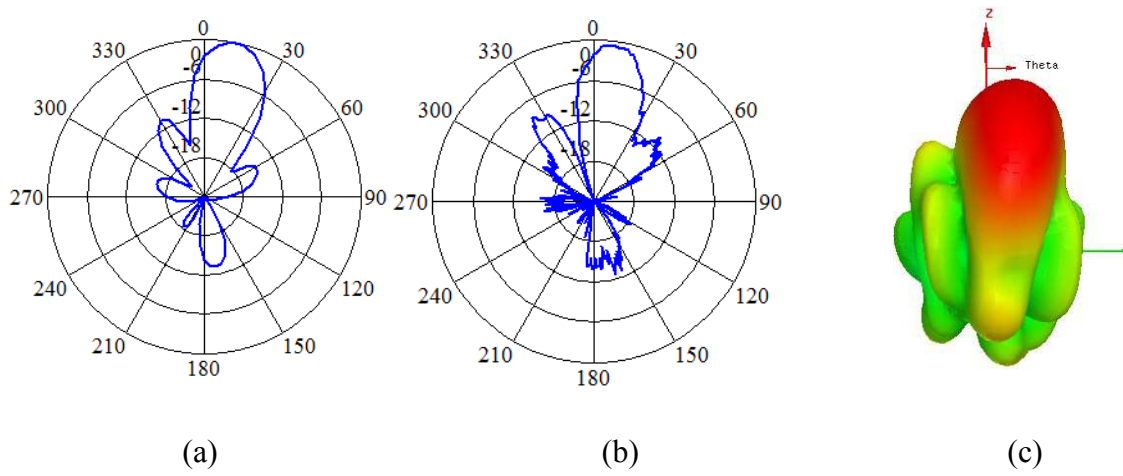


Fig. 5.11 Radiation pattern at scan angle,  $\theta = +10^\circ$  and center frequency,  $f_c = 8.6$  GHz (xz-plane). (a) Simulation. (b) Measurement. (c) Simulated 3D radiation pattern.

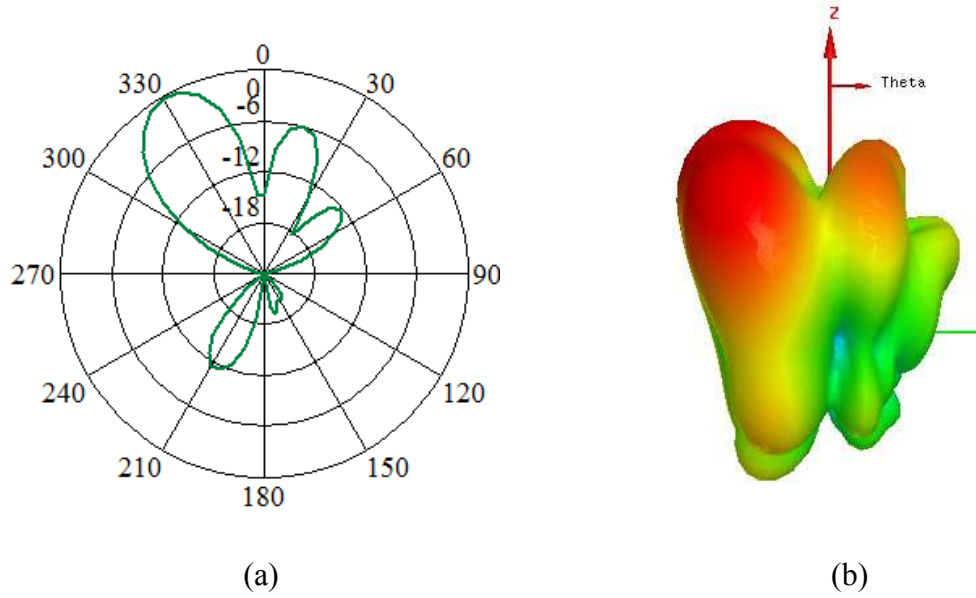


Fig. 5.12 Radiation pattern at scan angle,  $\theta = -30^\circ$  and center frequency,  $f_c = 8.6\text{GHz}$  (xz-plane). (a) Simulation. (b) Measurement. (c) Simulated 3D radiation pattern.

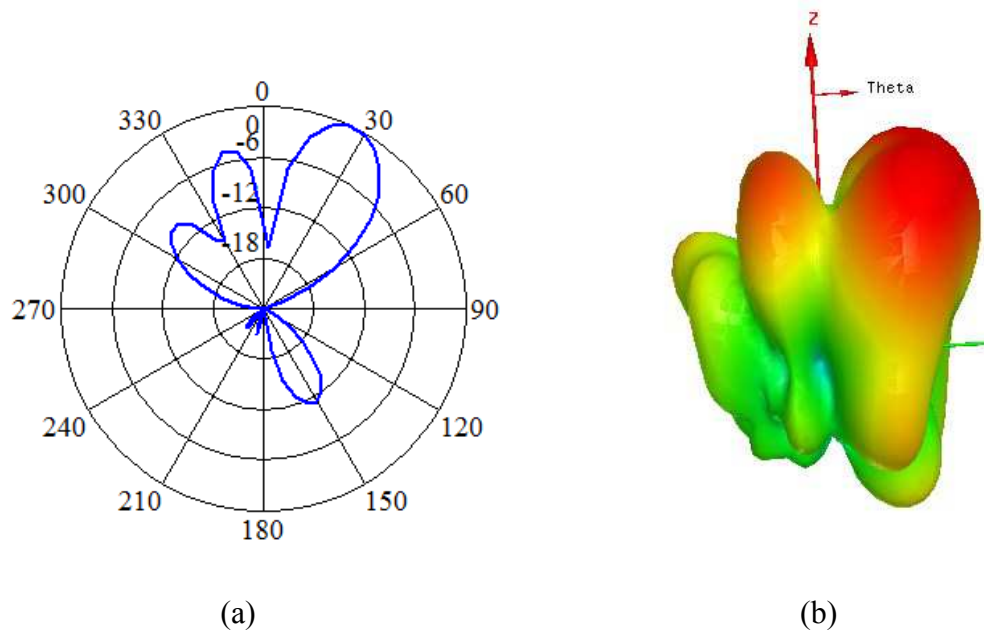


Fig. 5.13 Radiation pattern at scan angle,  $\theta = +30^\circ$  and center frequency,  $f_c = 8.6\text{GHz}$  (xz-plane). (a) Simulation. (b) Simulated 3D pattern.

Fig. 5.14 shows realized gains at  $xz$ -plane for  $-30^\circ$  to  $+30^\circ$  scan angle. Gain difference between broadside and maximum scan angle is 2.2 dB at center frequency,  $f_c=8.6$  GHz. Reduced realized gain at the maximum scan angle is due to the angular filtering characteristic of antenna elements. In theory, antenna elements have peak gain at broadside direction and gain reduces at the end-fire direction due to element factor of the antenna.

Figs. 5.15 to 5.19 shows the realized gain at  $xz$ -plane for the scan angle of  $0^\circ$ ,  $-15^\circ$ ,  $+15^\circ$ ,  $-30^\circ$  and  $+30^\circ$  at center frequency,  $f_c=8.6$  GHz, lower operating frequency  $f_{lo}=8.4$  GHz, and upper operating frequency  $f_{up}=8.8$  GHz. At 8.6 GHz, main beam-to-side lobe ratios are 11.6 dB for  $0^\circ$ , 6.4 dB for  $-15^\circ$ , 6.4 dB for  $+15^\circ$ , 5.3 dB for  $-30^\circ$ , and 5.3 dB for  $+30^\circ$ . Realized gains at  $xz$ -plane for scan angle from  $-30^\circ$  to  $+30^\circ$  are tabulated in table 5.3. In addition, figs. 5.18 to 5.19 show the occurrence of minor beam squinting at maximum scan angle ( $\pm 30^\circ$ ) when operating frequencies are varied from 8.4 GHz to 8.8 GHz. Low beam squint of  $0.2^\circ$  per 1% frequency variation is achieved in this work.

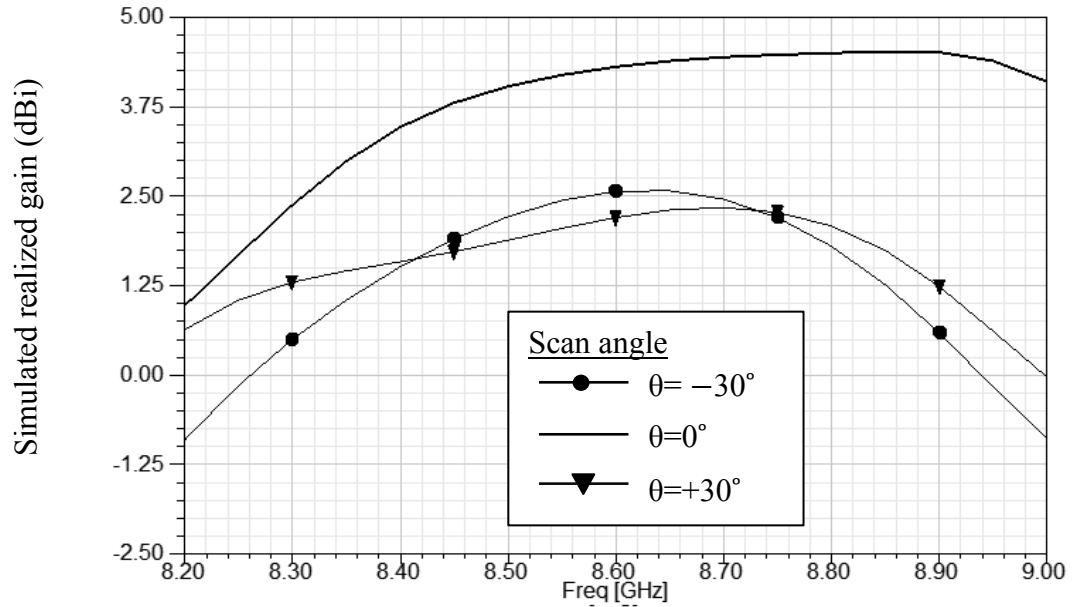


Fig. 5.14 Simulated realized gain of phased array antenna at  $xz$ -plane (max. scan angle  $\theta=\pm 30^\circ$ ).

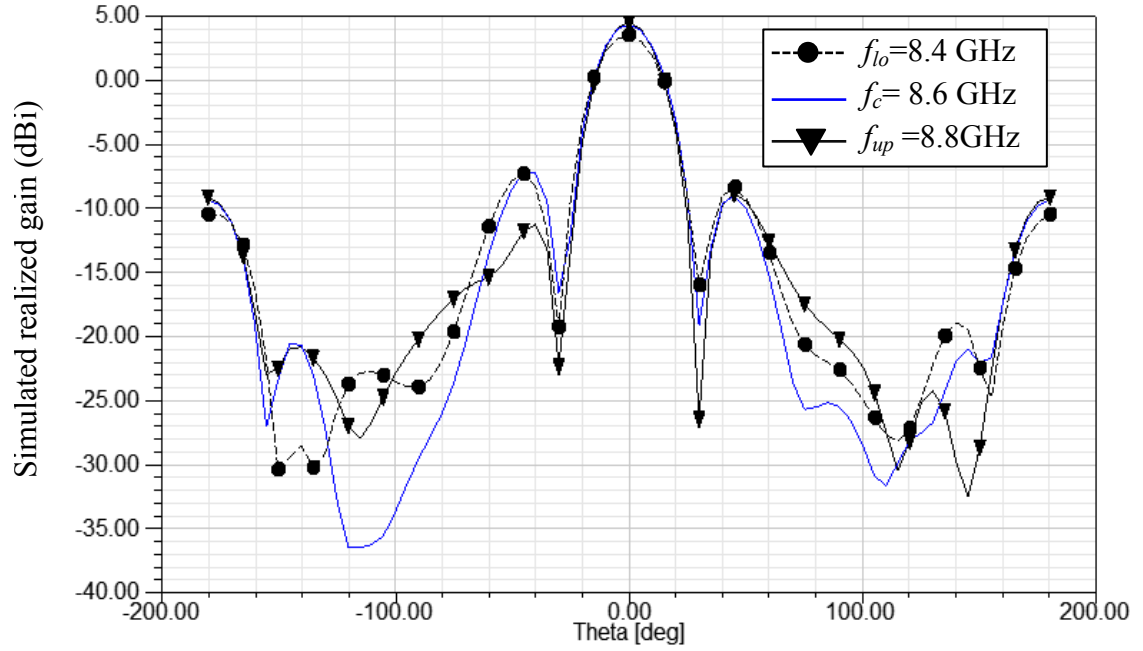


Fig. 5.15 Broadside radiation beam at multiple frequencies (no beam steering).

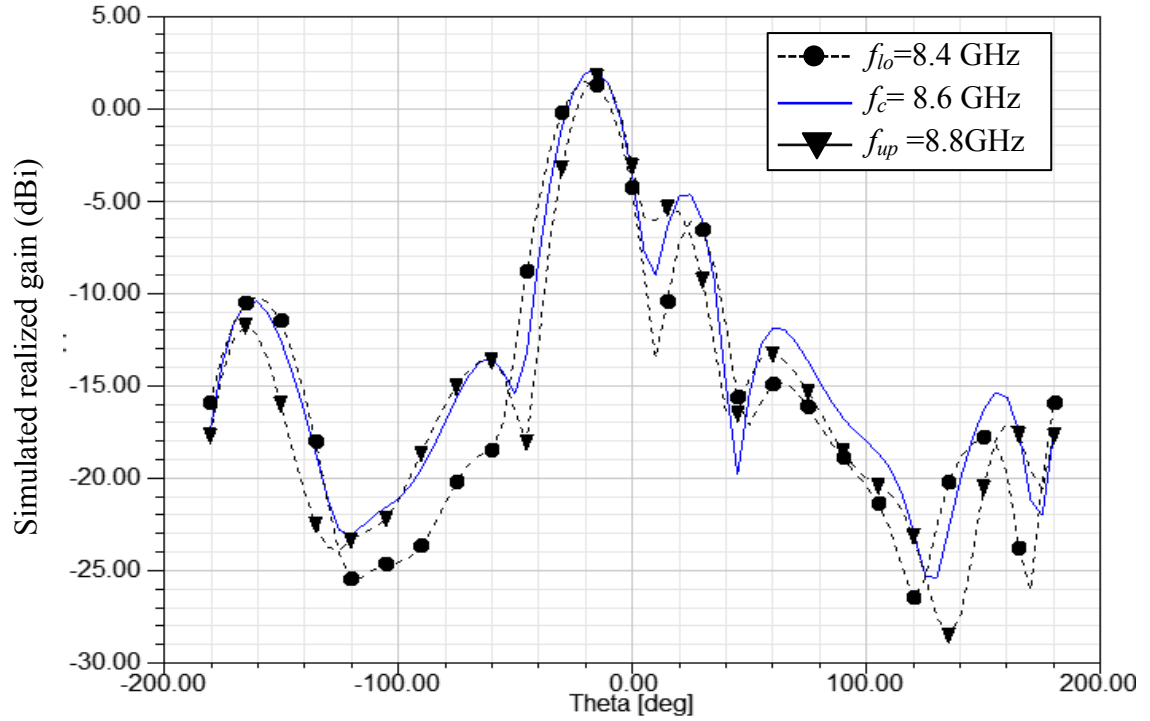


Fig. 5.16 Scan angle of  $-15^\circ$  at multiple frequencies (xz-plane)

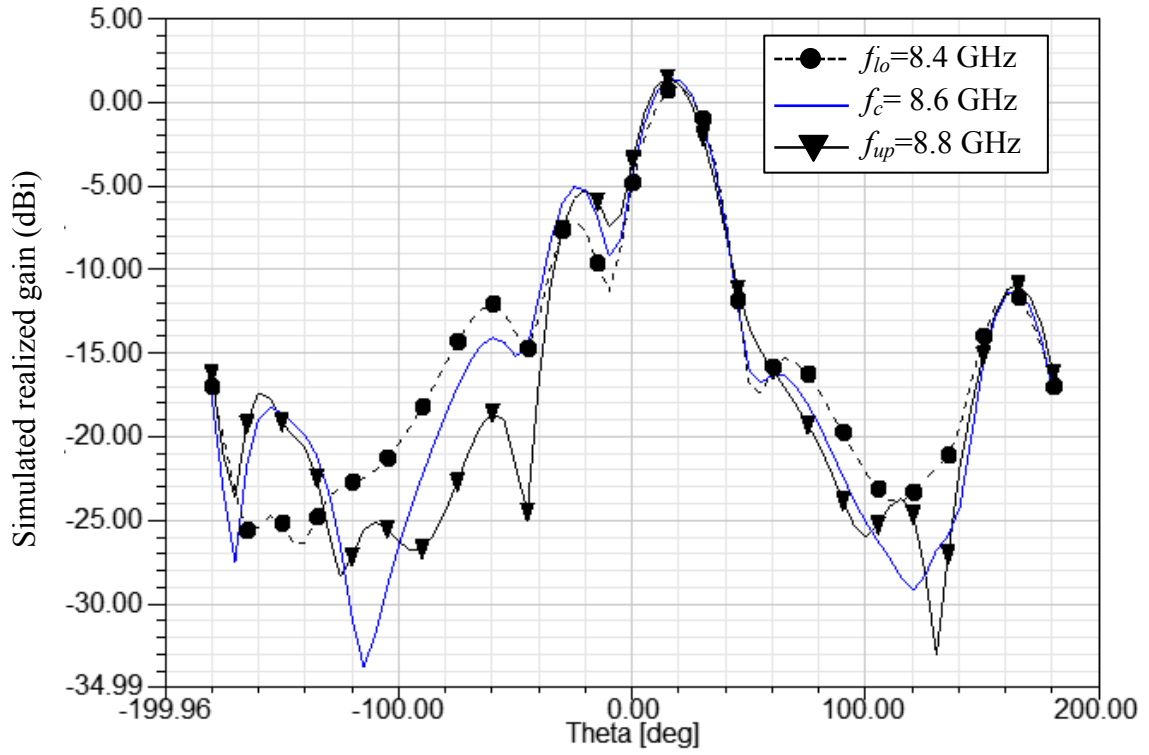


Fig. 5.17 Scan angle of +15° at multiple frequencies (xz-plane).

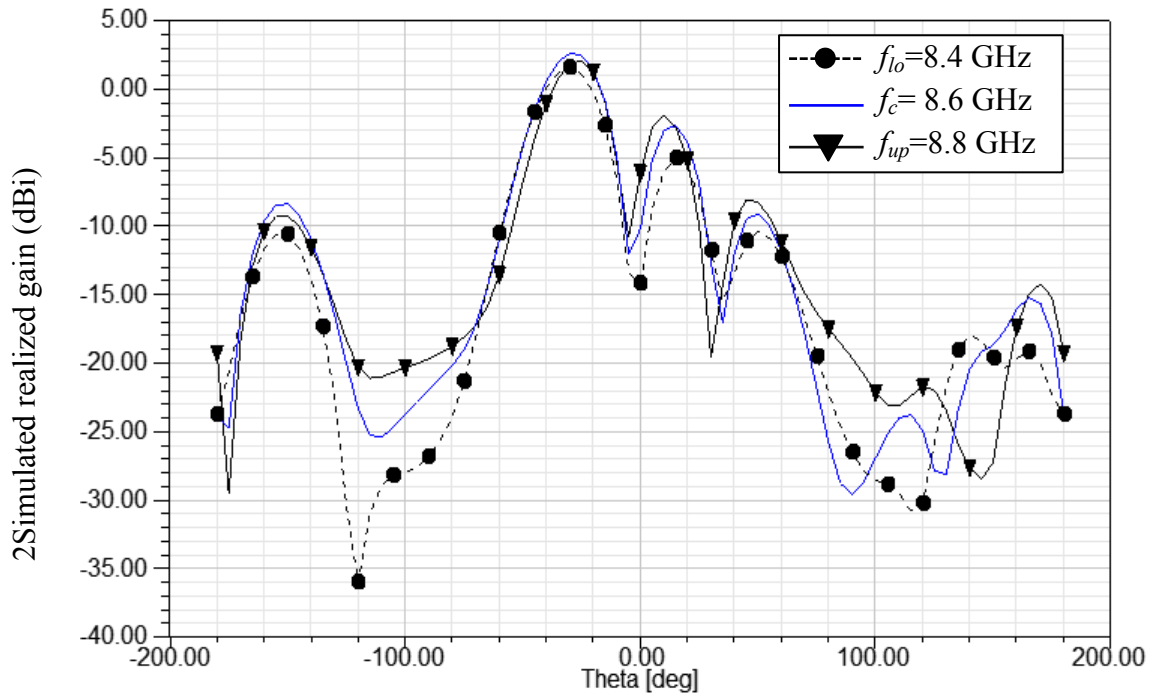


Fig. 5.18 Scan angle of -30° at multiple frequencies (xz-plane).



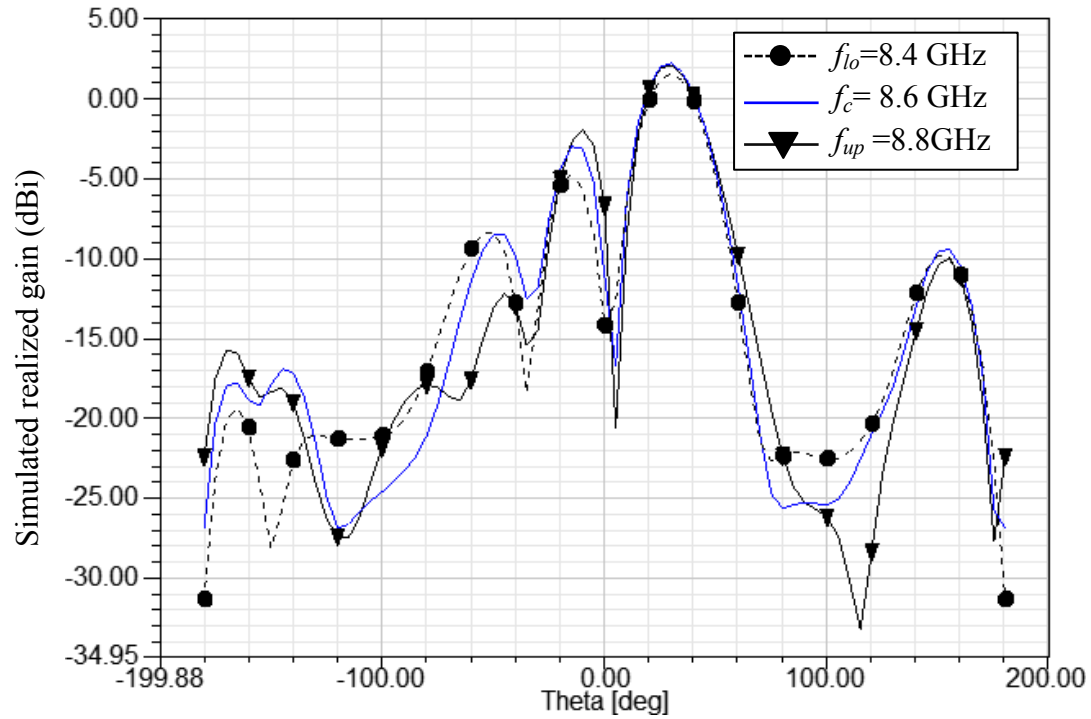


Fig. 5.19 Scan angle of  $+30^\circ$  at multiple frequencies ( $xz$ -plane).

Table 5.3 Realized gain for difference scan angle at the center frequency,  $f_c=8.6$  GHz.

Scan angle	Theta (deg)		$-60^\circ$	$-30^\circ$	$0^\circ$	$+30^\circ$	$+60^\circ$	SLL	$\theta_{-3dB}$
$-30^\circ$	8.4 GHz	Gain (dBi)	-13.6	1.8	-6.1	-19.7	-11.2	-2	$20^\circ$
	8.6 GHz	Gain (dBi)	-11	2.6	-10.2	-12.7	-11.9	-2.7	$20^\circ$
	8.8 GHz	Gain (dBi)	-10.6	1.5	-14.3	-14.8	-12.2	-5.1	$20^\circ$
$0^\circ$	8.4 GHz	Gain (dBi)	-11.4	-19.3	3.4	-16	-13.5	-8.4	$20^\circ$
	8.6 GHz	Gain (dBi)	-13.6	-16.5	4.3	-15.3	-19	-7.3	$20^\circ$
	8.8 GHz	Gain (dBi)	-15.4	-22.3	4.4	-26.4	-12.5	-11.2	$20^\circ$
$+30^\circ$	8.4 GHz	Gain (dBi)	-9.4	-13.1	-14.2	1.58	-12.8	-4.7	$20^\circ$
	8.6 GHz	Gain (dBi)	-11.4	-11.8	-11	2.19	-11.8	-3.12	$20^\circ$
	8.8 GHz	Gain (dBi)	-9.8	-14.5	-6.7	2.08	-9.79	-1.9	$20^\circ$

Table 5.4 Comparison of the proposed phased array antenna against other steerable antennas found in the literature.

	[7]	[11]	[5]	[12]	This work
Feeding Network	Series	Series	Series	Corporate	Corporate
Number of active antenna elements	4	4	5	11 (DRA*)	4
Center Frequency	2.4 GHz	2.45 GHz	5.8 GHz	7.7 GHz	8.6 GHz
Scan Range (Deg.)	49°	30°	22 °	60°	60°
Number of voltages	3	6	1	4	4
Max. bias voltage (V)	15 V	30 V	30 V	50 V	10 V
Beam squint	0.4 ° per 1% freq. variation	-	5.6° per 1% freq. variation	-	0.2 ° per 1% freq. variation
Gain variation with scan range	1.5 dB	-	0.4 dB	<1 dB	2.2 dB
Return loss bandwidth	3%	1.02%	4.6%	16.7%	12.5%

\*Dielectric resonator antenna (DRA)

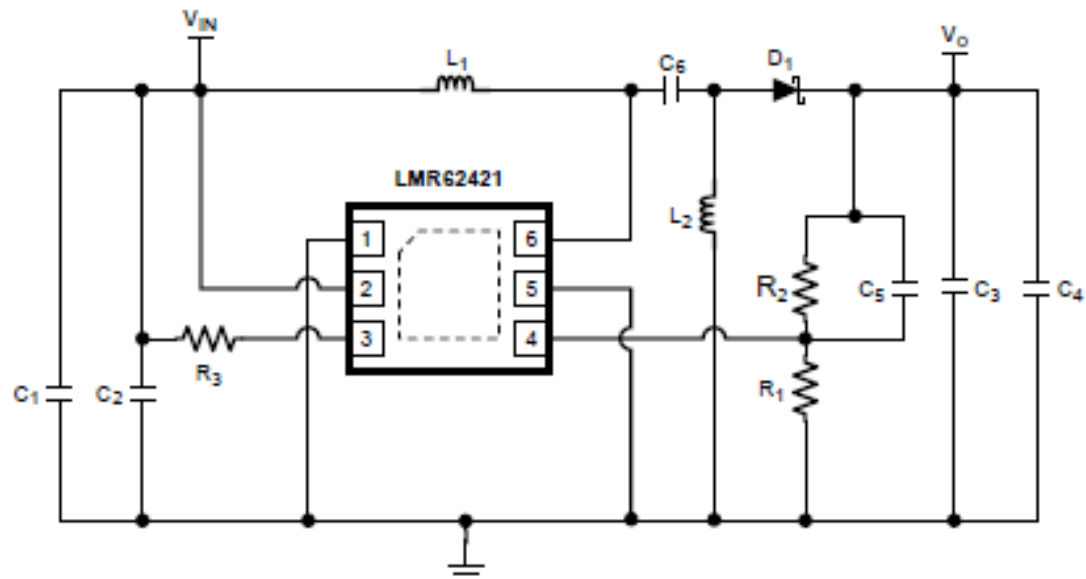
Table 5.4 summarizes the performance of the proposed phased array antenna against other steerable antennas found in the literature. Corporate-fed phased array antennas, such as work found in [12] and phased array antenna in this work, achieve a wider electronic scan-angle range compared to the other designs shown in the table 5.3. Work in [12] offers wide return loss bandwidth and gain variation is less than 1 dB for entire scan range. However, non-planar structure and high reverse bias voltage (50 V) are required for beam scanning makes it unfitted for compact wireless system. On the other hands, realization of large scan range of 60° with low reverse bias voltage (<10 V) in this work makes it a favorable candidate for area-constraint wireless application. Beam squint of this work is 0.2° per 1% percent of frequency variation, which is the lowest compared to the works found in the literature, as demonstrated in figs. 5.18 and 5.19. The only disadvantage of this work is that gain degradation is slight higher than other designs when beam is steered from broadside direction to  $\pm 30^\circ$ .

### 5.5 Chapter Summary

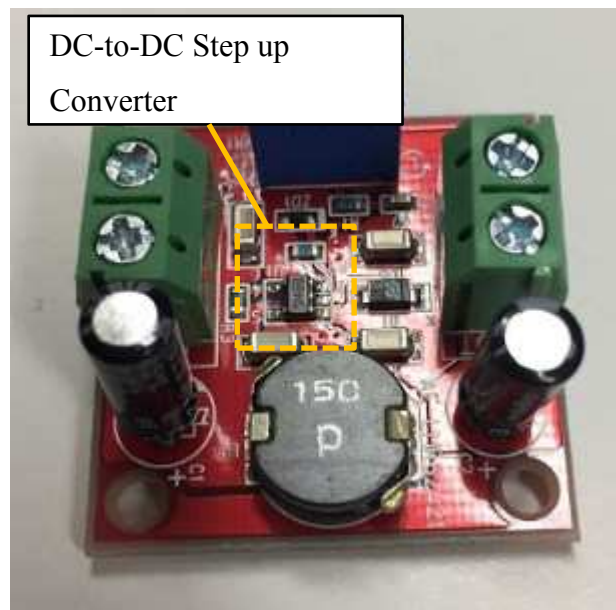
Corporate-fed phased array antenna with parasitic antennas for scan angle extension has been proposed. Corporate-fed phased array antenna has lower beam squint than series-fed phased array antenna. Corporate-fed network provides low group delay as signal propagates from source to antenna elements. On the other hand, phased array antennas found in the literatures were mostly based on series-fed network. Corporate-fed phased array antenna has not been widely studied because large phase shift range is required to realize wide scan angle. In this work, parasitic antennas have been deployed to increase scan angle of corporate-fed phased array antenna, which is limited by  $250^\circ$  phase shift range of phase shifters. Without parasitic antennas, the maximum scan angle range of the proposed phased array antenna is restricted to  $55^\circ$ . The presence of parasitic antennas in corporate-fed phase array antenna has increased the scan angle from  $55^\circ$  to  $60^\circ$ . Total scan range of  $60^\circ$  can be realized by using varactors with low bias voltage of 10 V.

In commercial applications, 1.8 V or 3.3 V is the common DC voltage level for TTL logic circuits. DC-to-DC step up converter can be used to step up DC voltage from 3.3 V to 10 V for the proposed phased array antenna to be implemented in compact wireless system. Fig. 5.20(a) and (b) shows the circuit diagram and hardware of commercially available DC-to-DC step up converter (LMR62421).

Proposed phased array antenna was fabricated on 4 layers FR-4 PCB and measured to validate the proposed design concept. Measurement results of radiation patterns are in agreement with the simulation results. In summary, phased array antenna operates on low bias voltage ( $<10$  V) to achieve wide scan angle ( $\pm 30^\circ$ ) has been realized. Beam squint of the proposed phased array antenna is lower than other series-fed phased array antenna found in the literature.



(a)



(b)

Fig. 5.20 Schematic of DC-to-DC step up converter (LMR62421) and its subsidiary components. (a) Block diagram, and (b) prototype of DC-to-DC step up converter.

## References

- [1] X. H. T. Chou, M. Y. Lee and C.T. Yu, “Subsystem of Phased Array Antennas With Adaptive Beam Steering in the Near-Field RFID Applications,” *IEEE Antennas and Wireless Propagation Lett.*, vol. 14, pp. 1746–1749, April 2015.
- [2] F. Ellinger, R. Vogt, and W. Bächtold, “Compact reflective type phase shifter MMIC for C-band using a lumped element coupler,” *IEEE Trans. Microw. Theory Tech.*, vol. 49, no. 5, pp. 913–917, May 2001.
- [3] C. S. Lin, S. F. Chang, and W.C. Hsiao, “A Full-360 Reflection-Type Phase Shifter With Constant Insertion Loss,” *IEEE Microw. Wireless Compon. Lett.*, vol. 18, no. 2, pp. 106-108, Feb. 2008.
- [4] P. Padilla, J. F. Valenzuela-Valdés, J. L. Padilla, J. M. Fernández-González, and M. Sierra-Castañer, “Electronically Reconfigurable Reflective Phase Shifter for Circularly Polarized Reflectarray Systems,” *IEEE Microw. Wireless Compon. Lett.*, vol. 26, no. 9, pp. 705-707, Sept. 2016.
- [5] E. Öjefors, S. Cheng, K. From, I. Skarin, P. Hallbjörner, and A. Rydberg, “Electrically Steerable Single-Layer Microstrip Traveling Wave Antenna With Varactor Diode Based Phase Shifters,” *IEEE Trans. on Ant. Prop.*, vol. 55, no. 9, pp. 2451-2459, Sept. 2007.
- [6] M. Tsuji, T. Nishikawa, K. Wakino, and T. Kitazawa, “Bi-Directionally Fed Phased-Array Antenna Downsized With Variable Impedance Phase Shifter for ISM Band,” *IEEE Trans. on Microw. Theory Techn.*, vol. 54, no. 7, pp. 2962-2969, Jun. 2006.
- [7] M. A. Y. Abdalla, K. Phang, and G. V. Eleftheriades, “A Planar Electronically Steerable Patch Array Using Tunable PRI/NRI Phase Shifters,” *IEEE Trans. on Microw. Theory Techn.*, vol. 57, no. 3, pp. 531-541, Feb. 2009.
- [8] D. Y. Ren, J. H. Choi, and T. Itoh, “Series Feed Networks for Dual Polarized Frequency Scanning Phased Array Antenna Based on Composite Right/Left-Handed Transmission Line,” *IEEE Trans. on Microw. Theory Techn.*, vol. 65, pp no. 12, pp. 5133-5143, Dec. 2017.

- [9] G. V. Eleftheriades, M. A. Antoniadis, and F. Qureshi, "Antenna applications of negative-refractive-index transmission-line (NRI-TL) structures," *IET Microw., Antennas, Propag.* (Special Issue on Metamater.), vol. 1, no. 1, pp. 12–22, Feb. 2007.
- [10] S.-S. Oh and L. Shafai, "Compensated circuit with characteristics of lossless double negative materials and its application to array antennas," *IET Microw., Antennas, Propag.*, vol. 1, no. 1, pp. 29–38, Feb. 2007.
- [11] A. Tombak and A. Mortazawi, "A novel low-cost beam-steering technique based on the extended-resonance power-dividing method," *IEEE Trans. Microw. Theory Tech.*, vol. 52, no. 2, pp. 664–670, Feb. 2004.
- [12] M. Nikfalazar, A. Mehmood, M. Sohrabi, and M. Mikolajek, A. Wiens, H. Maune, C. Kohler, J. R. Binder, and R. Jakoby, "Steerable Dielectric Resonator Phased-Array Antenna Based on Inkjet-Printed Tunable Phase Shifter With BST Metal-Insulator-Metal Varactors," *IEEE Antennas and Wireless Propagation Lett.*, vol. 15, pp. 877-880, Sept. 2015.
- [13] R.N. Nikkhah, M. J. Rashed-Mohassel, and A. A. Kishk, "Compact Low-Cost Phased Array of Dielectric Resonator Antenna Using Parasitic Elements and Capacitor Loading," *IEEE Trans. on Antennas Prop.*, vol. 61, no. 4, pp. 2318-2321, Jan. 2013.
- [14] Y. Yusuir and X. Gong, "Beam-Steerable Patch Antenna Array Using Parasitic Coupling and Reactive Loading," in *IEEE Antennas and Propagation Society International Symposium*, pp. 4693-4696, Jun. 2017.

## Chapter 6

### Conclusions and Future Work

#### 6.1 Conclusions

Analog phased array antenna has low power consumption and it is a good candidate for battery-powered wireless terminal devices. Although it could not deliver the smart functionalities that digital beamformer (DBF) does, it offers significantly low DC power consumption and reduces fabrication cost since the need for digital signal processor and analog-to-digital (ADC) is eliminated. Several hardware topologies were studied and analog phased array antenna is proposed to meet the demands for continuous beam steering.

The contributions of works in this dissertation can be summarized as follows:

##### A. Antenna for Multiple Layers PCB Manufacturing Process

Input impedance of conventional array antenna is sensitive to the thickness of dielectric substrate. In a complex system such as RF front end receiver in GPS, receiver architecture is split into few sections or blocks: RF front end module, and Controller Area Network (CAN). Typically, RF front end module consists of antenna, filter, low noise amplifier (LNA), mixer, and analog-to-digital converter. CAN consists of digital signal processor (DSP), memory modules, a Field Programmable Gate Arrays (FPGA)-based system controller and high speed clock signals. RF front-end and CAN are often combined into a signal module for space-saving.

To achieve compact design and short propagation distance, high frequency clock signals might pass through RF front end and vice-versa. In this situation, multiple layers fabrication process such as PCB, RF-CMOS or LTCC may emerge as prospective candidates for a high density and compact system. However, low degree of freedom in input impedance tuning of patch antenna constraints antenna implementation in multiple layers PCB. In this work, slotted patch antenna electromagnetically fed by two layers feed line has been proposed for multiple layers PCB manufacturing process. Contrary to conventional patch, input impedance and realized gain of the proposed antenna are less sensitive to the thickness of dielectric substrate.

#### B. Phase Shifter for Corporate Feed Phased Array System

Off-the-shelf integrated circuit (IC) phase shifters are widely available in either 2.4 GHz or 5 GHz. On the contrary, for operation frequency above 5 GHz, MMIC-based phase shifters sold in the market are overpriced due to low demand-to-supply ratio. Conventional Reflective-Type Phase Shifter (RTPS) was taken as reference model in this work. RTPS with integrated low pass filter has been proposed in this work to suppress higher order noise. Relative phase shift range of  $360^\circ$  is achieved with 12 V reverse bias voltage. However, proposed phase shifter is not suitable for phased array system because distributed transmission line of the phase shifter radiates and distorts far-field radiation pattern. Phase shifter with discrete reactive components as reflection loads has been proposed for phased array system. Continuous relative phase shift from  $0^\circ$  to  $250^\circ$  has been obtained with 10 V reverse bias voltage. Measured insertion loss variation ( $<1$  dB) of the proposed phase shifter is better than any off-the-shelf phase shifters, and those found in the literature that operate at similar frequency range. It is worth mentioning that the proposed phased shifter is cost-effective because it can be fabricated using standard PCB manufacturing process. Simulation and measurement results of phased array antenna based on the improved version of harmonic-suppressed phase shifters has good far-field radiation patterns.



### C. Parasitic Antenna to Increase Scan Angle In Phased Array System.

Corporate-fed phased array antenna requires large relative phase shift range to achieve wide scan angle. In corporate-fed network, the maximum scan angle is limited by relative phase shift range of phase shifter. As we know, radiation pattern and the maximum scan angle of phased array antenna are closely related to the multiplication of array factor to antenna element factor. In recent years, pattern reconfigurable antenna elements known as electronic steerable passive array antenna (ESPAR) were widely reported due to its capability to steer beam towards the end-fire direction without any phase shifter. Beam steering in ESPAR is realized using passive array antennas placed in the vicinity of active driven antenna, without the presence of any phase shifter. In ESPAR, portion of the current in the active path is induced to the passive antenna and this phenomenon is known as mutual coupling effect. Distance of passive antenna to the active antenna determines coupling co-efficient. Input impedance of ESPAR varies depends on the loading applied to the input port of passive antenna [1]-[2]. In this work, the author extended the working principle of ESPAR to increase scan angle of phased array antenna. As opposed to the ESPAR, input port of parasitic antennas in this work is not terminated to the ground. Besides, it is placed one-half of free space wavelength away from the active antenna. Input impedance of the parasitic antennas is optimized by changing the dimensions of the parasitic antenna. No current is induced when the main beam radiates at the broadside direction because parasitic antennas remain as high-impedance circuits. At the maximum scan angle, mutual coupling effects occurs between parasitic antenna and the nearest adjacent active antenna. As a result, scan angle range is extended to  $60^\circ$  ( $\pm 30^\circ$ ). Proposed parasitic antennas in this work have successfully increased the scan range from  $55^\circ$  to  $60^\circ$  through the manipulation of radiation characteristic of active antenna element.

## 6.2 Future works

Realized gain is reduced when beam is steered from broadside direction towards end-fire direction. It is inevitable because of angular filtering characteristic of antenna elements. Related gain degradation should be given serious consideration. Degradation associated to beam steering can be minimized if antenna element has radiation pattern with wide half-power beam width. In this work, 2.2 dB gain degradation is observed when the beam is steered from  $0^\circ$  to  $\pm 30^\circ$ . For improvements in future, magneto-electric dipole antennas in [3]-[5] should be considered as a replacement for existing antenna elements. Symmetrical E- and H-plane patterns of the magneto-electric dipole antenna offer wide half-power beam width and stable gain over wide frequency bandwidth. The main obstacle of integrating magneto-electric dipole antenna to the phased array antenna is its non-planar structure. Existing knowledge gap on exciting non-planar antennas as antenna array using planar feeding network, in either series-fed or corporate-fed networks, remains as huge challenge for it to be utilized in planar phased array system for mass production.

## References

- [1] Mohammad Ranjbar Nikkhah, J. Rashed-Mohassel, and Ahmed A. Kishk, "High-Gain Aperture Coupled Rectangular Dielectric Resonator Antenna Array Using Parasitic Elements," *IEEE Trans. on Antennas Prop.*, vol. 61, no. 7, July 2013.
- [2] Mohammad Ranjbar Nikkhah, J. Rashed-Mohassel, and Ahmed A. Kishk, "Compact Low-Cost Phased Array of Dielectric Resonator Antenna Using Parasitic Elements and Capacitor Loading," *IEEE Trans. on Antennas Prop.*, vol. 61, no. 4, April 2013.
- [3] Lei Ge and Kwai Man Luk, "A Low-Profile Magneto-Electric Dipole Antenna," *IEEE Trans. on Antennas Prop.*, Vol. 60, no. 4, pp. 1684-1689, April 2012.
- [4] Lei Ge and Kwai Man Luk, "A Wideband Magneto-Electric Dipole Antenn," *IEEE Trans. on Antennas Prop.*, Vol. 60, no. 11, Nov. 2012.
- [5] Guangwei Yang and Jianying Li, "Study on wide-angle scanning linear phased array," in *2017 IEEE International Symposium on Antennas and Propagation & USNC/URSI National Radio Science Meeting*, pp. 491-492, July 2017.